

**Searches for New Physics in final states
containing leptons, b -jets and E_T^{miss} at the
ATLAS detector**



UNIVERSITY OF

LIVERPOOL

Thesis submitted in accordance with the requirements of the
University of Liverpool for the degree of Doctor in Philosophy by

Matthew James Sullivan

Department of Physics
Oliver Lodge Laboratory
University of Liverpool

September 2020

Abstract

This is my abstract.

Declaration

I hereby confirm this work is my own, except where other works are referenced. This work has not previously been submitted to any institute, including this one. This thesis does not exceed the relevant word count.

Matthew James Sullivan

Acknowledgements

During my eight years at the University of Liverpool, the people helping to make it such a memorable period of my life have become innumerable, and to thank each and every person would require an equally long period of time. For those not acknowledged by name I can only give my thanks for being involved in this part of my life. It has been a true privilege to call this city my home and be a part of the Department of Physics throughout.

The first of many thanks goes to my mum, my dad and my sister, for their endless and unwavering support throughout my PhD. The level of support you all offer continues to astound me and I can only offer my gratitude in return. An honourable mention must go to my niece, Charlotte, who was born halfway through my PhD and has been the best niece one could ask for, although these words are, for now, lost on you.

Secondly, many thanks are owed to the non-physics friends, who have given me respite from the challenges of my PhD. Particularly, Holly, Brad, Pete, Alex, Ellie and Sean, who have supported and encouraged me through challenging professional and personal times. Your continued reminder to write this Thesis, however, is unforgiveable. Additionally, a big thanks to Hannah, who for the last ten years has been putting up with my nonsense, and hopefully will continue to do so. I hope over time I can begin to pay back the levels of support you have all given me.

These acknowledgements would be incomplete without a mention to the circumstances within which a large portion of it was written. The COVID-19 pandemic has had a devastating impact on individuals and families the world-over, causing both physical and mental struggle. On a personal level, numerous thanks are owed for enabling me to submit this work in this turbulent time. Firstly, to UKRI, for their generous financial support, enabling me to continue my work during these challenging times. Secondly, thanks are owed to the NHS, both due to their handling of the national crisis and for their continued healthcare support during, undoubtedly, the most stressful period of my life. However, the period of national lockdown due to the coronavirus has also provided unforeseen opportunities for personal development, and I submit this work having gained far more than anticipated. Countless thanks are owed to Jess, for managing to keep my stress-levels under control, for

the walks, the talks and the laughs. Without you, this work would have been submitted in a much heavier fashion.

Of course, many thanks are owed to the physics community within which I have been immersed. Firstly, to the Liverpool ATLAS group, who welcomed me into the collaboration in 2016 and have supported me throughout my PhD. The group, and the department, provided me with some incredible opportunities, for which I am extremely grateful. Secondly, to all of the physics friends, who have listened to my rants, help spot the bugs I couldn't find, and bluntly point out when I'm being stupid. Special thanks must go to James, Chips and Lauren for dealing with me when at my most difficult, and for the frequent trips to the pub, both in Liverpool and Geneva.

Finally, to my excellent supervisors, Monica D'Onofrio and Yanyan Gao. You have pushed me to levels beyond what I imagined I could achieve and have given me amazing opportunities for professional development. I can only apologise for being slow and stupid, and am extremely grateful for your patience in supervision.

Contents

List of Figures	x
List of Tables	xiii
Introduction	1
I Theoretical overview and experimental apparatus	3
1 The Standard Model and Beyond	4
1.1 The Standard Model	4
1.2 Physics Beyond the Standard Model	16
2 The LHC and the ATLAS Experiment	23
2.1 The LHC accelerator	23
2.2 Luminosity and pileup	24
2.3 ATLAS overview	26
2.4 Magnet system	28
2.5 Inner Detector	29
2.6 Calorimetry	31
2.7 Muon System	33
2.8 ATLAS Trigger System	34
3 Data and Monte Carlo samples	36
3.1 Datasets	36
3.2 Monte Carlo simulation	39
3.3 Simulating Wt -channel single top at NLO	43
4 Object reconstruction	50
4.1 Reconstruction overview	50
4.2 Leptons	51
4.3 Jets	55
4.4 Flavour-tagging	58

4.5	$E_{\text{T}}^{\text{miss}}$	60
4.6	Overlap removal	61
4.7	Event cleaning	62
4.8	Object definitions summary	62
5	Analysis methods	64
5.1	General search analysis strategy	64
5.2	Discriminant variables	65
5.3	Selection optimisation methods	67
5.4	Estimating systematic uncertainties	73
5.5	Statistical analysis	76
II	Searches for New Physics in Run-2 ATLAS data	80
6	Searches for $\tilde{\chi}_1^\pm \tilde{\chi}_2^0$ pair-production	81
6.1	SUSY signal model	82
6.2	Event selection	84
6.3	Background estimation	84
6.4	Systematic uncertainties	86
6.5	Results	86
6.6	Studies with 139fb^{-1}	92
7	Search for Dark Matter production in association with a top quark	93
7.1	2HDM+ a signal model	93
7.2	Event selection	96
7.3	Background estimation	97
7.4	Systematic uncertainties	98
7.5	Results	100
III	High-Luminosity LHC studies	112
8	Sensitivity to $\tilde{\chi}_1^\pm \tilde{\chi}_2^0$ pair-production at the HL-LHC	113
8.1	MC simulation	114
8.2	Detector simulation	115
8.3	Event selection	118
8.4	Systematic uncertainties	122
8.5	Results	124
	Appendices	128

A	Sensitivity to $\tilde{\chi}_1^\pm \tilde{\chi}_2^0$ pair-production at the HL-LHC	128
A.1	Detector simulation parameterisations	128
A.2	Cut & count studies	132
A.3	Deep learning studies	132
A.4	Extending W +jets sample statistics	135
B	Testbeam studies of FE-I4 and RD53A performance at HL-LHC	137
B.1	ATLAS ITk upgrade	138
B.2	Experimental setup	138
B.3	138
	Bibliography	139

List of Figures

1.1	QED interaction vertex.	8
1.2	QCD interaction vertices.	9
1.3	Electroweak gauge boson interaction vertices.	11
1.4	Schematic of the Higgs potential.	13
1.5	Higgs interaction vertices	14
1.6	SM Higgs branching ratios	15
1.7	SUSY particle production cross-sections	19
1.9	Running of SM coupling constants	21
2.1	Diagram of the LHC accelerator complex	24
2.2	Integrated luminosity as a function of time in Run-2	25
2.3	Pileup profile for Run-2	26
2.4	Diagram of the ATLAS detector	27
2.5	Diagram of the ATLAS magnet system	28
2.6	Diagram of the ATLAS Inner Detector	29
2.7	Diagram of the ATLAS Calorimetry System	32
2.8	Diagram of the ATLAS Muon Spectrometer	34
2.9	Functional diagram of ATLAS trigger and DAQ system	35
3.1	E_T^{miss} trigger efficiency for 2015-2018	38
3.2	Overview of the MC simulation chain	40
3.3	Feynman diagrams for $t\bar{t}$ at leading order	40
3.4	Feynman diagrams for Wt -channel single top at leading order	43
3.5	Feynman diagrams for Wt -channel single top at next-to-leading order	44
3.6	Comparison of E_T^{miss} distribution in CRST for DR and DS samples	46
3.7	Comparison of p_T^{b2} and $\Delta\phi(\ell, E_T^{\text{miss}})$ distributions in the proposed single top CR	48
3.8	Comparison of m_T and m_{CT} distributions using $WWbb$ samples	49
4.1	Representative diagram of particle signatures within ATLAS	51
4.2	Electron identification efficiencies in Run-2	53

4.3	Muon reconstruction efficiencies in Run-2	54
4.4	Distributions of muon track- and calorimeter-based isolation	55
4.5	Output of MV2c10 BDT applied on simulated $t\bar{t}$ events	59
4.6	b -tagging efficiency and MC scale-factors as a function of jet p_T	60
5.1	Schematic diagram showing typical search regions configuration	65
6.1	Diagram of $\tilde{\chi}_1^\pm \tilde{\chi}_2^0$ pair-production with a final state of 1 lepton, 2 b -tagged jets and E_T^{miss}	82
6.2	Run-1 summary plot of searches for $\tilde{\chi}_1^\pm \tilde{\chi}_2^0$ pair-production	82
6.3	Production cross-sections for various electroweak SUSY particles	84
6.4	Post-fit distributions	89
6.6	Exclusion limits for $\tilde{\chi}_1^\pm \tilde{\chi}_2^0$ production with Wh signature	91
7.1	Feynman diagram for the tW +MET analysis	94
7.2	Diagram of DM produced in association with a $t\bar{t}$ pair.	95
7.3	Production cross-section for DM plus top quark processes	96
7.4	Key kinematic variables at preliminary selection level	99
7.5	Post-fit E_T^{miss} distributions in CRs	104
7.6	Post-fit E_T^{miss} distributions in VRs	105
7.7	Post-fit N-1 distributions in SR	106
7.8	Summary of data/MC agreement in all CR/VRs	107
7.9	Exclusion limits for the DMt signature	108
7.10	Exclusion limits for the $DMt + t\bar{t}$ signature	109
8.1	Simulated $t\bar{t}$ event in the ATLAS ITk with $\langle\mu\rangle = 200$	114
8.2	Comparison of the key kinematic distributions for truth, truth-smearred and fully reconstructed $t\bar{t}$ samples	118
8.3	Signal grid separation for HL-LHC projection	120
8.4	Preselection-level distributions for HL-LHC projection	122
8.5	BDT outputs for HL-LHC projection	123
8.6	Limit plot for HL-LHC projection	125
A.1	Electron performance parameterisations for HL-LHC detector simulation	129
A.2	Muon performance parameterisations for HL-LHC detector simulation	130
A.3	Jet performance parameterisations for HL-LHC detector simulation	131
A.4	E_T^{miss} performance parameterisations for HL-LHC detector simulation	131
A.5	Expected sensitivity in each reoptimised signal region, and the best expected combination.	133
A.6	Diagram of DNN used in deep learning HL-LHC sensitivity estimate	133
A.7	DNN outputs on benchmark SUSY signals.	134

A.8 E_T^{miss} comparison of W +jets nominal and extended sample. 136

List of Tables

1.1	Summary table of the SM particles	6
1.2	Chiral supermultiplets in the MSSM	18
1.3	Gauge supermultiplets in the MSSM	18
1.4	SUSY gauge and mass eigenstates	18
2.1	Summary of the Pixel Detector and SCT components	30
3.1	Summary of E_T^{miss} triggers used in Run-2 relevant for this Thesis	37
3.2	Table showing the MC estimates for the SM backgrounds in CRST	45
3.3	Table of proposed single top CR selections	46
3.4	Yields and purity in proposed single top CR	47
3.5	Comparison of Wt DR and DS predictions with dedicated $WWbb$ predictions	48
4.1	Summary of object definitions used in subsequent Chapters	63
6.1	Summary of SUSY simplified model assumptions	83
6.2	Preliminary event selection for $\tilde{\chi}_1^\pm \tilde{\chi}_2^0$ pair-production search	85
6.3	Signal region definitions for $\tilde{\chi}_1^\pm \tilde{\chi}_2^0$ pair-production search	85
6.4	Control region definitions	85
6.5	Validation region definitions	86
6.6	Summary of dominant experimental and modelling systematics	86
6.7	Background-only fit results in the CRs	87
6.8	Background-only fit results in the SRs	88
6.9	Background normalisation factors	88
6.10	From left to right, the observed 95% CL upper limits on the visible cross-sections σ_{vis} , the observed (S_{obs}^{95}) and expected (S_{exp}^{95}) 95% CL upper limits on the number of signal events with $\pm 1\sigma$ excursions of the expectation, and the discovery p -value (p_0), truncated at 0.5.	92
7.1	Summary of 2HDM+ a model parameters and choices	96
7.2	Preliminary selections	97
7.3	Signal region definitions	98

7.4	Control region definitions	98
7.5	Validation region definitions	100
7.6	Summary of dominant experimental and modelling systematics	100
7.7	Background-only fit results in the control regions	101
7.8	Background-only fit results in the validation regions	102
7.9	Background-only fit results in the signal region	103
7.10	Background normalisation factors	103
7.11	Expected and observed yields in inclusive discovery regions	110
7.12	Model-independent limits from inclusive SRs	111
8.1	Summary of ME and PS configurations used to generate SM MC samples.	115
8.2	Summary of object definitions for leptons for HL-LHC projection	118
8.3	Summary of object definitions for jets for HL-LHC projection	119
8.4	Summary of preselection for HL-LHC projection	119
8.5	Optimised BDT output cuts for the three SRs.	122
8.6	Extrapolated systematic uncertainties for HL-LHC projection.	124
8.7	Expected yields in all SRs after BDT cuts.	125
A.1	Reoptimised signal region selections for HL-LHC sensitivity study.	132

1 Introduction

2 Since its inception the Standard Model (SM) of particle physics has withstood huge
3 amounts of experimental scrutiny. The SM provides a mathematical framework in which
4 to describe *all* non-gravitational interactions of the known fundamental particles. With
5 the discovery of the Higgs boson, a cornerstone of the SM, by the ATLAS and CMS col-
6 laborations in 2012 [1, 2], the SM is considered complete.

7

8 While one cannot detract from the success of the SM's description of physics at the smallest
9 scales, there are numerous open questions which have not yet been answered. The reconcil-
10 iation of gravity with physics at the subatomic scale, the hierarchy problem, astrophysical
11 evidence of dark matter, and the matter-antimatter asymmetry require explanations from
12 physics Beyond the Standard Model (BSM). The experiments at the Large Hadron Col-
13 lider (LHC) have a broad programme of direct and indirect searches for BSM physics.
14 Aiding in this is the LHC itself, providing pp collisions at $\sqrt{s} = 13$ TeV at luminosities
15 around $10^{34} \text{cm}^2 \text{s}^{-1}$. The huge datasets collected by both ATLAS and CMS, afforded
16 by the LHC and its excellent performance, provide an ideal environment for BSM searches.

17

18 The physics analyses presented in this Thesis target two BSM scenarios; searches for Su-
19 persymmetry (SUSY) and searches for Dark Matter (DM) production. In both scenarios,
20 the SM Higgs sector is extended to include an additional Higgs doublet, hence these mod-
21 els being known as Two Higgs Doublet models (2HDM). SUSY extends the SM with an
22 additional symmetry in which particles gain 'superpartners', particles which differ in spin
23 by 1/2 from their SM counterpart. The superpartners to the SM gauge bosons and Higgs
24 mix and form a rich particle spectrum containing charged and neutral states, known as
25 charginos and neutralinos. The lightest supersymmetric particle (LSP), in this case the
26 lightest neutralino, is a leading candidate for DM. A search for the weak production of
27 SUSY particles, specifically a chargino-neutralino pair, decaying to the supersymmetric
28 DM candidate is performed, through decays involving the SM Higgs and W boson. Aside
29 from SUSY, by adding a pseudoscalar mediator, a , to a 2HDM model, DM can couple
30 to the SM extended Higgs sector leading to a rich array of final states. The associated
31 production of DM with a single top quark, a previously experimentally-uncovered final
32 state, is studied in the context of the 2HDM+ a model. In addition to DM coupling to the

33 SM through 2HDM+ a scenarios,

34

35 Both BSM scenarios studied in this Thesis are experimentally-challenging, due to the low
36 rate of new particle production when compared to irreducible SM processes. Advanced
37 signal selection techniques using machine learning (ML) methods are studied, enabling the
38 efficient selection of signal while substantially rejecting the SM background. The upcoming
39 High-Luminosity upgrade of the LHC and ATLAS will provide the opportunity to probe
40 many BSM scenarios to levels never before possible, with an expected dataset of 3000 fb^{-1}
41 being collected by ATLAS by the end of operations. To prepare for the HL-LHC phase of
42 operation, ATLAS will undergo a major upgrade of many detector components. The AT-
43 LAS inner tracker (ITk) will provide high-precision tracking in conditions where as many
44 as 200 inelastic proton-proton collisions are expected in each bunch-crossing. The efficiency
45 of the pixel modules of the ITk are studied after being irradiated to the expected HL-LHC
46 dose. Combining ML methods with the huge High Luminosity (HL) ATLAS dataset, the
47 sensitivity to SUSY at the High-Luminosity LHC (HL-LHC) is also studied.

48

49 **Part I** provides an overall introduction in the context of physics models and the ex-
50 perimental setup. First, a theoretical overview of the SM is given, motivates the need for
51 BSM physics, and then gives an overview of SUSY and the 2HDM+ a model of DM pro-
52 duction. It also gives a brief description of the LHC along with an overview of the ATLAS
53 detector. Finally, the datasets used in this thesis are discussed, along with discussion of
54 the simulation methods and object definitions used in the subsequent Chapters.

55

56 **Part II** describes the core work of this Thesis, encompassing three analyses using pp
57 data at $\sqrt{s} = 13 \text{ TeV}$, presented in separate Chapters. Chapter 6 presents a search for
58 electroweak SUSY using 36.1 fb^{-1} data and subsequently 139 fb^{-1} . Chapter 7 presents a
59 search for DM production in association with a single top quark using 139 fb^{-1} data.

60

61 **Part III** presents studies and work relevant for the HL-LHC phase. Chapter 8 illus-
62 trates the prospect for a search for the electroweak production of SUSY particles using
63 3000 fb^{-1} data at $\sqrt{s} = 14 \text{ TeV}$. Chapter B presents work done on the Inner Tracker (ITk)
64 studying the performance of hybrid pixel modules for upcoming upgrade for the HL-LHC.

65

Part I

66

Theoretical overview and experimental apparatus

67

Chapter 1

The Standard Model and Beyond

This chapter presents an overview of the Standard Model (SM), along with the extensions to it which form the basis of the analyses in Chapters 6 and 7. The SM is currently our best description of nature but does not give a complete description of some fundamental physical phenomena, outlined in Section 1.2, which motivates searches for physics beyond the SM (BSM).

1.1 The Standard Model

The SM is the name given to the theory describing the fundamentals of particle interactions. Since its inception over half a century ago, it has withstood experimental scrutiny, each time providing a theoretical description of experimental data. The particle content of the SM was deemed complete in 2012, with the discovery of a particle consistent with the Higgs boson by the ATLAS [1] and CMS [2] collaborations.

The SM describes matter in terms of quarks and leptons and their interactions via three of the four fundamental forces through the exchange of force-carriers known as bosons. As alluded to at the beginning of this Chapter, the SM provides an incomplete description of physics at the smallest scales, which will be discussed later in this Chapter.

Overview

The SM particles are easily separable into two categories; fermions, which obey Fermi-Dirac statistics and have half-integer spin, and bosons, which obey Bose-Einstein statistics and have integer spin.

The fermions are further separable into two families, quarks and leptons, both of which have three generations. The quarks can be separated into ‘up-type’ and ‘down-type’, having electric charge $+\frac{2}{3}$ and $-\frac{1}{3}$, respectively. The ‘up-type’ quarks are the up (u), charm (c)

94 and top (t) quarks, while the ‘down-type’ quarks are the down (d), strange (s) and bottom
95 (b). The leptons can be separated into charged leptons and neutral leptons (known as
96 neutrinos), with the charged leptons having an electric charge of -1 . The charged leptons
97 are the electron (e), the muon (μ) and the tau (τ), with a corresponding electron neutrino
98 (ν_e), muon neutrino (ν_μ) and tau neutrino (ν_τ). The three generations of fermions are
99 ordered in increasing mass, with the first generation containing the up and down quarks,
100 the electron and its corresponding neutrino, the former three of which combine to make
101 up everyday matter. In the SM neutrinos do not have mass, but experimental evidence of
102 neutrino flavour oscillations [3] implies that neutrinos are in fact massive, although their
103 mass hierarchy is not yet clear [4].

104

105 Composite particles can be formed from combinations of quarks when they undergo hadro-
106 nisation. ‘Hadrons’ are defined as bound states of quarks, with mesons being formed from
107 pairs of quarks and baryons being formed by three quarks. In recent years, more exotic
108 bound states of quarks, such as tetra-quarks [5, 6] and penta-quarks [?, 7] have been ob-
109 served by the LHCb collaboration. All quarks except the top quark undergo hadronisation
110 after a period of time. The top quark, which has a much larger mass than the other
111 quarks, has a lifetime around $\tau_t = 10^{-25}$ s and as such decays via the weak force before it
112 can hadronise. The first generation quarks, i.e. the up quark and down quark, can be
113 combined to produce protons (uud) and neutrons (udd). Combining protons and neutrons
114 with the first generation charged lepton, the electron, we give rise to nuclear physics and
115 all physical matter in our universe.

116

117 The SM bosons are responsible for the interactions of the SM particles. Electromagnetic
118 interactions are mediated by the massless photon (γ), and only occur between electrically-
119 charged particles. Gluons (g), massless and electrically-neutral bosons, mediate the inter-
120 actions between quarks, which carry the colour charge. The W^\pm and Z^0 bosons mediate
121 the weak interaction, which all SM fermions are subject to. Both the W^\pm and Z^0 bosons
122 are massive, and acquire their mass through the spontaneous breaking of the electroweak
123 symmetry, as discussed later in this Chapter.

124

125 The particle content of the SM is summarised in Table 1.1.

126 Mathematical formulation of the SM

127 The SM is a quantum field theory (QFT) based upon the product of symmetry groups:

$$SU(3)_C \times SU(2)_L \times U(1)_Y \tag{1.1.1}$$

128 The $SU(3)_C$ component describes strong interactions (QCD), the $SU(2)_L$ component
129 describes the electroweak sector and $U(1)_Y$ describes electromagnetic interactions.

Name	Symbol	Charge (e)	Spin	Mass
Fermions - Generation-I				
Up-quark	u	+2/3	1/2	2.16 MeV
Down-quark	d	-1/3	1/2	4.67 MeV
Electron	e	-1	1/2	0.511 MeV
Electron-neutrino	ν_e	0	1/2	< 2 eV
Fermions - Generation-II				
Charm-quark	c	+2/3	1/2	1.27 GeV
Strange-quark	s	-1/3	1/2	93 MeV
Muon	μ	-1	1/2	105.66 MeV
Muon-neutrino	ν_μ	0	1/2	< 2 eV
Fermions - Generation-III				
Top-quark	t	+2/3	1/2	172.9 GeV
Bottom-quark	b	-1/3	1/2	4.18 GeV
Tau	τ	-1	1/2	1.78 GeV
Tau-neutrino	ν_τ	0	1/2	< 2 eV
Bosons				
W boson	W^\pm	± 1	1	80.4 GeV
Z boson	Z	0	1	91.2 GeV
Gluon	g	0	1	0
Photon	γ	0	1	0
Higgs boson	H	0	0	125.1 GeV

Table 1.1: A table describing the charge, mass and spin of the SM particles. Particle masses taken from [8].

130

131 In order to understand the mathematical formulation of the SM, the concepts of *groups* will
 132 be briefly discussed. A group is a set of mathematical objects, G , along with an operation,
 133 which obey the following ‘axioms’ [9]:

134

- *Closure*: For all $a, b \in G$, $a \cdot b \in G$

135

- *Associativity*: For all a, b and $c \in G$, $(a \cdot b) \cdot c = a \cdot (b \cdot c)$

136

- *Identity element*: An identity element, I , exists such that $I \cdot a = a \cdot I = a$

137

- *Inverse element*: An inverse element of a , a^{-1} , exists such that $a \cdot a^{-1} = a^{-1} \cdot a = I$

138

The commutation relations of the members of a group are important to know. As a

139 reminder, the commutator of two elements of a group, a, b is defined as:

$$[a, b] = (a \cdot b - b \cdot a) \quad (1.1.2)$$

140 Groups where the commutator of any two elements is always 0 are known as ‘abelian’,
 141 while groups where this does not hold are called ‘non-abelian’. Abelian groups have n^2
 142 generators of the underlying Lie algebra, while non-abelian groups have $n^2 - 1$ generators.
 143 While this seems conceptually-abstract, the number of generators of a group physically
 144 corresponds to the number of ‘force-carriers’ present in a theory governed by that group.

145

146 In equation 1.1.1, $U(n)$ and $SU(n)$ refer to unitary groups and special unitary groups,
 147 respectively. $U(n)$ is the set of $n \times n$ unitary matrices ($U \cdot U^{-1} = I$), and $SU(n)$ the subset
 148 of $U(n)$ which have a determinant of 1. The individual symmetry groups will be discussed
 149 in more details in the following sections, starting with electromagnetic interactions and the
 150 $U(1)$ group.

151 Quantum Electrodynamics

152 Electromagnetic interactions are described by Quantum Electrodynamics (QED). These
 153 interactions are unique in the SM, as they have infinite range. We will derive the Lagrangian
 154 describing QED, starting from the Dirac equation for free fermions:

$$\mathcal{L}_{\text{Dirac}} = \bar{\psi}(i\gamma^\mu \partial_\mu - m)\psi \quad (1.1.3)$$

155 Due to the $U(1)$ symmetry, QED is symmetric under *global* phase transformations of the
 156 form:

$$\psi(x) \rightarrow \psi'(x) = e^{i\alpha}\psi(x), \quad \bar{\psi}(x) \rightarrow \bar{\psi}'(x) = e^{-i\alpha}\bar{\psi}(x) \quad (1.1.4)$$

157 Under *local* transformations, where $\alpha \rightarrow \alpha(x)$, the Lagrangian in Equation 1.1.3 is not
 158 gauge invariant:

$$i\bar{\psi}'\gamma^\mu \partial_\mu \psi' = i\bar{\psi}\gamma^\mu \partial_\mu \psi - \bar{\psi}\gamma^\mu \partial_\mu \alpha \psi \quad (1.1.5)$$

159 To resolve this, we define the covariant derivative:

$$D_\mu \equiv \partial_\mu + ieA_\mu \quad (1.1.6)$$

160 Note, with the introduction of the covariant derivative comes the introduction of the vector
 161 field, A_μ , which transforms as:

$$A_\mu \rightarrow A'_\mu = A_\mu - \frac{1}{e}\partial_\mu \alpha(x) \quad (1.1.7)$$

162 The result of a local transformation on the Dirac equation is now:

$$i\bar{\psi}'\gamma^\mu D'_\mu\psi' - m\bar{\psi}\psi = i\bar{\psi}\gamma^\mu\partial_\mu\psi - \bar{\psi}\gamma^\mu eA_\mu\psi - m\bar{\psi}\psi \quad (1.1.8)$$

163 Rearranging Equation 1.1.6 for ∂_μ and substituting in, we see local gauge invariance holds
 164 thanks to the introduction of the covariant derivative. Of particular interest is the term
 165 $\bar{\psi}\gamma^\mu eA_\mu\psi$, which couples the fermion fields to the vector field, which we associate to the
 166 photon, γ , with the coupling constant e corresponding to the electrical charge of the
 167 fermion. To complete the QED Lagrangian, one must add the electromagnetic Lagrangian
 168 to the Dirac Lagrangian. (For concision, we now adopt the Feynman ‘slash’ notation:
 169 $\not{D} = \gamma^\mu\partial_\mu$).

$$\mathcal{L}_{QED} = \mathcal{L}_{Dirac} + \mathcal{L}_{EM} = \bar{\psi}(i\not{D} - m)\psi - \frac{1}{4}F^{\mu\nu}F_{\mu\nu} \quad (1.1.9)$$

170 As the interaction term, introduced by using the covariant derivative, couples fermions to
 171 the photon with a coupling e , QED interactions are only relevant for electrically-charged
 172 fermions. Figure 1.1 shows the QED interaction vertex.

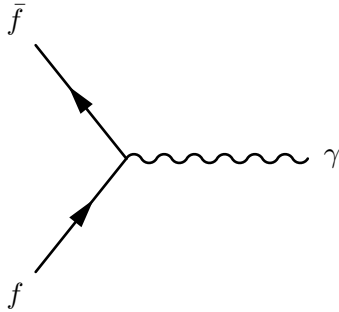


Figure 1.1: Feynman diagram showing the QED interaction vertex between a fermion and the photon.

173 Quantum Chromodynamics

174 Quantum Chromodynamics addresses the interactions between quarks and gluons. It is
 175 governed by the $SU(3)_C$ symmetry hence having $N_C^2 - 1 = 8$ mediators. By virtue of
 176 the symmetry group being a *special* unitary group, the theory is non-abelian, resulting in
 177 gluons being able to self-interact. Similarly to QED, we begin from the Dirac Lagrangian
 178 and introduce a covariant derivative, in this case defined as:

$$\partial^\mu = D^\mu \equiv \partial^\mu\delta_{ij} - ig_s t_{ij}^a G^{a\mu} \quad (1.1.10)$$

179 where δ_{ij} is the Kroenecker delta (0 for $i \neq j$, 1 for $i = j$), g_s the strong coupling
 180 constant, $t^a = \frac{\lambda^a}{2}$ the generators of the $SU(3)_C$ symmetry group with λ^a being the Gell-
 181 Mann matrices and G^a being the gluon gauge fields. Rewriting the Dirac equation from

182 Equation 1.1.3:

$$\mathcal{L}_{\text{QCD}} = \bar{\psi}_j(i\gamma_\mu\partial^\mu - m\delta_{ij})\psi_i \quad (1.1.11)$$

183 In Equation 1.1.11, i and j index the quarks from 1 to 3 and a indexes the gluons
 184 from 1 to 8. Replacing the regular partial derivate in Equation 1.1.10 with the covariant
 185 derivative from Equation 1.1.11, we obtain:

$$\mathcal{L}_{\text{QCD}} = \bar{\psi}_j(i\gamma_\mu\partial^\mu\delta_{ij} - m\delta_{ij})\psi_i - g_s(\bar{\psi}_j\gamma_\mu t_{ij}^a\psi_i)G^{a\mu} \quad (1.1.12)$$

186 Adding in the kinetic term for the gluon fields and again using the Feynman slash
 187 notation, the full QCD Lagrangian is:

$$\mathcal{L}_{\text{QCD}} = \bar{\psi}(i\not{D} - m)\psi - \frac{1}{4}G_a^{\mu\nu}G_{\mu\nu}^a \quad (1.1.13)$$

188 Equation 1.1.13 is helpful to understand the gluon self-interaction, with 3-gluon and
 189 4-gluon interactions present in the expansion of the $G_a^{\mu\nu}G_{\mu\nu}^a$.

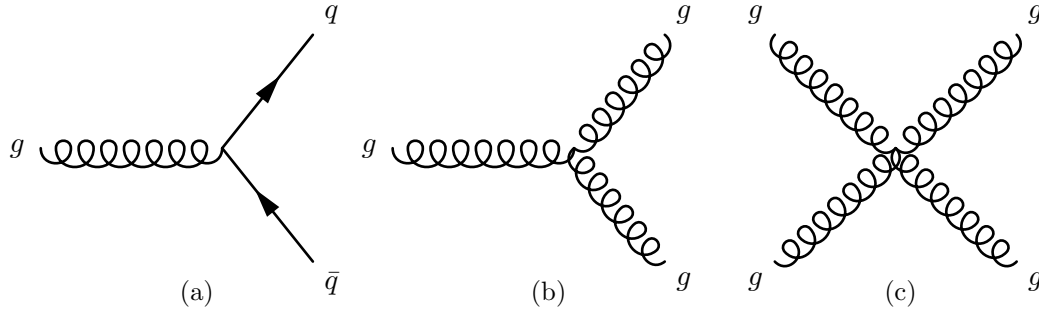


Figure 1.2: Feynman diagram showing the QCD quark-gluon interaction vertex (a), the triple gluon self-interaction (b) and the quartic gluon self-interaction (c).

190 The gauge coupling of QCD depends upon the momentum transfer of a process, Q^2 ,
 191 as follows:

$$g_s(Q^2) = \frac{4\pi}{\beta_0 \ln\left(\frac{Q^2}{\Lambda_{\text{QCD}}^2}\right)} \quad (1.1.14)$$

192 The Q^2 dependence of α_s means the coupling strength "runs" depending on the momen-
 193 tum transfer. At large Q^2 , which corresponds to the high-energy or short-distance regime,
 194 quarks and gluons are treated as free particles. In this regime, perturbative QCD (pQCD)
 195 calculations can be used to make very accurate predictions. In pQCD, calculations pro-
 196 ceed by performing a series expansion in α_s , where higher-order terms correspond to the
 197 contribution from Feynman diagrams with additional QCD vertices. Calculating the cross-
 198 section of a QCD process in this way can lead to ultraviolet (UV) divergences arising from
 199 loops in higher-order Feynman diagrams, which requires the introduction of the *renormal-*
 200 *isation scale*, μ_R , to remove them. This means the evaluation of α_s is dependent upon

201 mu_R , which is typically set to the mass of the Z boson, m_Z , at which the strong coupling
 202 has a value of 0.118.

203

204 However, in the low-energy limit, where $Q^2 \rightarrow \Lambda_{\text{QCD}}^2$, where Λ_{QCD}^2 is the energy at which
 205 quarks and gluons hadronise, known as the *hadronisation scale*, the strong coupling tends
 206 to infinity and hence perturbative calculations can no longer be used. This results in
 207 quarks being bound together into colour-neutral hadrons, a phenomena known as *colour*
 208 *confinement*. Colour confinement forbids the existence of a quark in isolation, instead
 209 forcing quarks to exist in colourless, bound states, known as hadrons. Due to the running
 210 coupling, when the separation of a quark-antiquark pair is increased, so does the energy
 211 of the strong interaction between them. With increasing separation, it eventually becomes
 212 energetically-favourable to produce another quark-antiquark pair. This quark-antiquark
 213 pair forms colourless, bound states with the initial quark-antiquark pair. An additional
 214 result of colour confinement is that the range of the strong force is extremely short, around
 215 1fm.

216 Weak interaction and Electroweak unification

217 The third force described by the SM is the weak interaction, which describes interactions
 218 between the left-handed fermions and is described by The $SU(2)_L$ symmetry group. It is
 219 therefore expected that the weak interaction has 3 mediators (from $N^2 - 1$); W_μ^1 , W_μ^2 and
 220 W_μ^3 . The weak interaction also introduces new quantum numbers known as weak isospin,
 221 T , as well as its third component T_3 . With these quantum numbers, we can define weak
 222 isospin doublets, using the first generation leptons and quarks as examples:

$$\begin{pmatrix} \nu_L \\ e_L \end{pmatrix}; \begin{pmatrix} u_L \\ d_L \end{pmatrix} \quad (1.1.15)$$

223 Both of the weak isospin doublets shown in Equation 1.1.15 have $T = \frac{1}{2}$, with the fermion
 224 in the ‘upper’ position having $T_3 = +\frac{1}{2}$ and the fermion in the ‘lower’ position having
 225 $T_3 = -\frac{1}{2}$.

226

227 An extremely important concept for understanding the weak interaction is chirality. Chi-
 228 rality is an intrinsic property of particles, and determines how they behave in the weak
 229 interaction. The subscript ‘L’ is present as only fermions with ‘left-handed’ chirality (anti-
 230 fermions with ‘right-handed’ chirality) interact via the weak interaction. ‘Left-handed’
 231 fermions, and ‘right-handed’ anti-fermions have $T = \frac{1}{2}$ and hence form isospin doublets,
 232 whereas ‘right-handed’ fermions and ‘left-handed’ anti-fermions have $T = 0$ and hence are
 233 isospin singlets.

234

235 The introduction of weak isospin doublets enables a mechanism for quarks to change flavour
 236 through a charged-current interaction. For example, a ‘down-type’ quark can change into
 237 an ‘up-type’ quark through a transition of T_3 . The Cabibbo-Kobayashi-Maskawa matrix,
 238 known as the CKM matrix, determines the probability of a quark, q , to transition to
 239 another flavour.

$$\begin{pmatrix} d' \\ s' \\ b' \end{pmatrix} = \begin{pmatrix} |V_{ud}| & |V_{us}| & |V_{ub}| \\ |V_{cd}| & |V_{cs}| & |V_{cb}| \\ |V_{td}| & |V_{ts}| & |V_{tb}| \end{pmatrix} \begin{pmatrix} d \\ s \\ b \end{pmatrix} \quad (1.1.16)$$

240 The CKM matrix is *almost* a diagonal matrix, with the on-diagonal elements being
 241 close to one, while the off-diagonal elements are small but non-zero. Therefore, the most
 242 probable quark flavour transitions are intra-generational, but inter-generation transitions
 243 are allowed.

244

245 It was shown by Glashow, Salam and Weinberg that the interaction can be unified with
 246 the electromagnetic interaction, with an overall symmetry group of $SU(2)_L \times U(1)_Y$. We
 247 now introduce the weak hypercharge, $Y = 2(Q - T_3)$, where Q is the electric charge. At
 248 low energies, the electromagnetic and weak interactions independently explain physical
 249 phenomena, such as hyperfine splitting and β decay in nuclei. The unification of these
 250 two interactions into the electroweak interaction must therefore preserve the two separate
 251 interactions at low energy. However, above the ‘unification energy’, the two separate
 252 interactions are merged into a one. This new, unified interactions has four mediators;
 253 two massive, charged W^\pm bosons, a massive, neutral Z and the massless, neutral γ from
 254 the $U(1)$ symmetry in QED. The interaction vertices of the three massive electroweak
 255 gauge bosons are shown in Figure 1.3. Note, Figure 1.3b shows the interaction of only the
 negatively-charged W boson interacting with leptons.

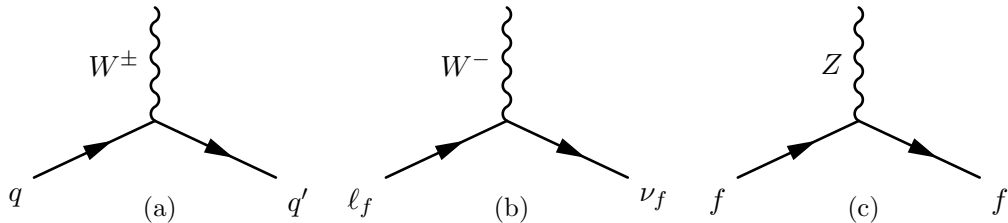


Figure 1.3: Feynman diagrams showing the massive electroweak gauge bosons interaction vertices. Note, as shown in (b), only the W^- couples to the lepton isospin doublet, whereas for the quark isospin doublets (a) both the W^\pm are involved.

256

257 The $SU(2)_L \times U(1)_Y$ symmetry group is non-abelian, and thus the electroweak gauge
 258 bosons can self-interact. Similarly to gluons in QCD, there are triple and quartic self-

259 couplings; $W^\pm W^\mp Z/\gamma$, $W^\pm W^\mp Z/\gamma Z\gamma$ and $WWWW$.

260 As discussed previously, to ensure local gauge invariance of the SM electroweak La-
261 grangian, we define the covariant derivative:

$$\partial_\mu \rightarrow D_\mu \equiv \partial_\mu + \frac{i}{2}g\vec{\tau} \cdot \vec{W}_\mu + ig'\frac{Y}{2}B_\mu \quad (1.1.17)$$

262 where \vec{W}_μ and B_μ are the gauge fields, and g and g' are the couplings, of the $SU(2)_L$
263 and $U(1)_Y$ symmetries, respectively. As the electroweak interaction only couples to ‘left-
264 handed’ fermions, we can define projection operators, which project out the left- and
265 right-handed components of a field:

$$P_L = \frac{1}{2}(1 - \gamma^5); P_R = \frac{1}{2}(1 + \gamma^5); \gamma^5 \equiv \begin{pmatrix} 0 & I_2 \\ I_2 & 0 \end{pmatrix} \quad (1.1.18)$$

266 We are then able to write the fermion field as $\psi = P_L\psi + P_R\psi = \psi_L + \psi_R$. The mass
267 term in the Lagrangian, $m\bar{\psi}\psi$, now expands as:

$$m\bar{\psi}\psi = m\bar{\psi}_R\psi_L + m\bar{\psi}_L\psi_R \quad (1.1.19)$$

268 The left- and right-handed components of the fermion field, ψ , transform differently
269 under the $SU(2)_L \times U(1)_Y$ symmetry and therefore the mass term in Equation 1.1.19 breaks
270 local gauge symmetry. Therefore, we need to introduce a mechanism by which fermions,
271 and also the electroweak gauge bosons, become massive.

272 The Higgs sector

273 The discovery of the W^\pm bosons [10, 11] and Z boson [12, 13] in 1983 with masses around
274 $m_W \sim 80$ GeV and $m_Z \sim 91$ GeV, in good agreement with electroweak predictions,
275 proved the need for a mechanism through which the gauge bosons acquire mass. The
276 Higgs mechanism, first proposed in the 1960’s, provided such a mechanism by introducing
277 an $SU(2)_L$ doublet of complex, scalar fields:

$$\Phi = \begin{pmatrix} \phi^+ \\ \phi^0 \end{pmatrix} = \frac{1}{\sqrt{2}} \begin{pmatrix} \phi_1 + i\phi_2 \\ \phi_3 + i\phi_4 \end{pmatrix} \quad (1.1.20)$$

278 This doublet has isospin $T = \frac{1}{2}$ and hypercharge $Y = 1$. This field has a scalar potential
279 defined as:

$$V(\Phi) = \mu^2\Phi^\dagger\Phi + \lambda(\Phi^\dagger\Phi)^2 \quad (1.1.21)$$

280 The two terms in Equation 1.1.21 can be identified as a mass term for the scalar boson
281 and a self-interaction term, respectively. Dependent upon the choices for μ^2 ($\lambda > 0$), the

282 potential can take on two shapes; parabolic for $\mu^2 > 0$ and a ‘wine bottle’ potential for
 283 $\mu^2 < 0$. For reasons discussed later, the Higgs potential has $\mu^2 < 0$, and the shape of this
 284 potential is shown in Figure 1.4.

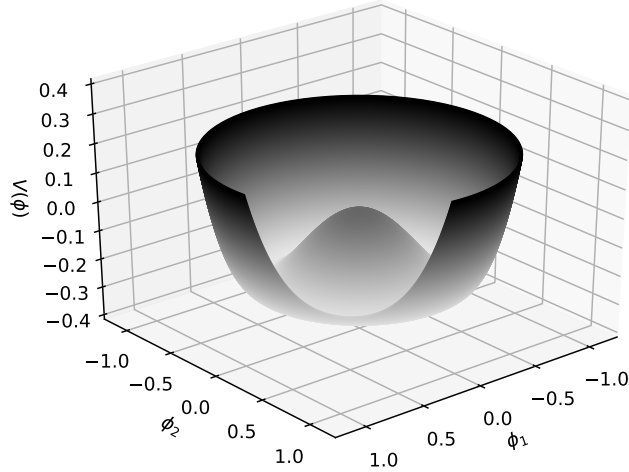


Figure 1.4: Schematic diagram showing the shape of the Higgs potential, known as the ‘Mexican hat’ potential.

285 The potential shown in Figure 1.4 evidently has a local minima at $\phi_1, \phi_2 = 0$. However,
 286 the global minima is at non-zero values of ϕ , and is given by:

$$\phi_{min} = \sqrt{-\frac{\mu^2}{2\lambda}} \quad (1.1.22)$$

287 We define $v^2 = \mu^2/\lambda$, where v is the vacuum expectation value (vev) of the the Higgs field.
 288 The vev of the Higgs field is therefore, non-zero, and is experimentally determined to be
 289 ≈ 246 GeV. It is convenient to choose the vevs of the ϕ_1, ϕ_2 and ϕ_4 to zero, while for ϕ_3
 290 the vev is:

$$\langle 0|\phi_3|0\rangle^2 = v^2 = \frac{\mu^2}{\lambda} \quad (1.1.23)$$

291 The choice for the spontaneous symmetry breaking to be done with the field ϕ_3 is to
 292 allow the photon to remain massless. Expanding the Higgs field around the minima with
 293 $\phi_3 = h + v$, we eventually acquire a term for the Higgs mass of $m_H = \sqrt{-2\mu^2}$. Inserting

294 this field into 1.1.17, we obtain the mass terms for the electroweak gauge bosons:

$$\begin{aligned}
 m_W &= \frac{1}{2}gv \\
 m_Z &= \frac{1}{2}\sqrt{g^2 + g'^2} v \\
 m_\gamma &= 0
 \end{aligned}
 \tag{1.1.24}$$

295 The Higgs Lagrangian contains couplings to not only the electroweak gauge bosons but
 296 also the SM fermions. The strength of the couplings to the fermions are given by y_f ,
 297 known as *Yukawa couplings*. This coupling enables the fermions to acquire masses in a
 298 gauge-invariant way through the Higgs mechanism. The mass of a fermion, f , is given by:

299

$$m_f = y_f \frac{v}{\sqrt{2}}.
 \tag{1.1.25}$$

300 Fermion masses are experimentally-determined, hence determining the Yukawa coupling of
 301 the Higgs to that fermion. The interactions of the Higgs with the electroweak gauge bosons
 and SM fermions are shown in Figure 1.5. The Higgs decay branching ratios (BR) depends

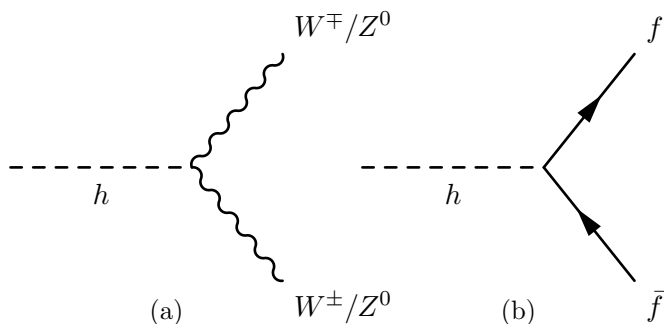


Figure 1.5: Feynman diagrams showing the Higgs interaction vertices with the electroweak gauge bosons (1.5a) and SM fermions (1.5b).

302

303 both upon the Higgs mass and the Yukawa coupling of the Higgs to the SM particles.

304 Figure 1.6 shows the Higgs BRs for a SM Higgs boson with a mass in the range, 120-130

305 GeV. The largest Higgs BR is to a $b\bar{b}$ -pair, which is important for the analyses detailed in

306 Chapters 6 and 8.

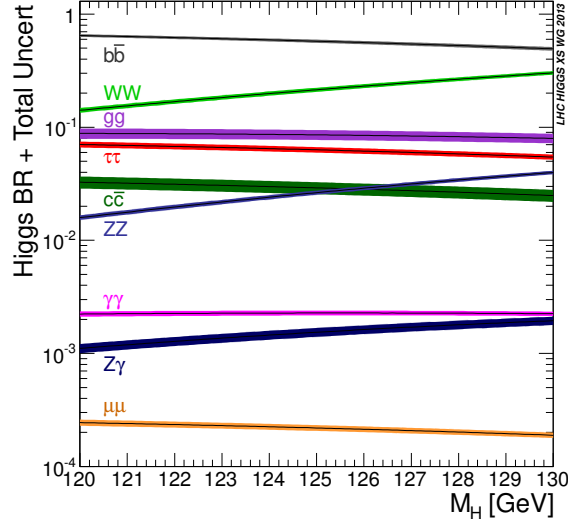


Figure 1.6: This plot shows the branching ratios of the SM Higgs decaying to SM particles in the mass range 120-130 GeV. **REF**

307 Open questions in the SM

308 The first of the open questions to be discussed is the hierarchy problem. While the SM does
 309 not account for gravitational interactions, it is impossible to have a complete description
 310 of nature, a so-called ‘Grand Unified Theory’ (GUT), without its inclusion. The hierarchy
 311 problem arises when considering a unified theoretical description of all four, fundamental
 312 forces. Gravity is expected to become the dominant interaction at the Planck scale, which
 313 has an equivalent mass of $O(10^{19})$ GeV. This is 17 orders of magnitude higher the elec-
 314 troweak scale and the Higgs mass, $O(10^2)$ GeV.

315

316 The Higgs mass consists of two terms; a ‘bare’ mass and the sum of the virtual corrections
 317 from particles coupling to the Higgs. We treat the Planck scale, Λ_P , as a cut-off value for
 318 the virtual contributions. Therefore, the physical Higgs mass can be written as:

$$m_H^2 = m_{H,\text{bare}}^2 + \delta m_H^2 = m_{H,\text{bare}}^2 - \frac{|g_f|^2}{8\pi^2} \Lambda_p^2 + \dots \quad (1.1.26)$$

319 Here, the neglected terms grows logarithmically in Λ_p . Assuming the SM is indeed valid
 320 upto the Planck scale, then the second term is $O(10^{19}\text{GeV})^2$, requiring an equally-large
 321 (to 1 part in over 10^{30} orders of magnitude) bare Higgs mass. The Anthropic Principle
 322 is sometimes invoked to justify this ‘fine-tuning’ [14], while extensions to the SM such as
 323 Supersymmetry (SUSY) provide elegant, mathematical solutions to the hierarchy problem.

324

325 Within the SM, neutrinos do not have mass, but experimental observation of neutrino
 326 oscillations implies that they do have mass, and that each neutrino flavour is a mixture of

327 the mass eigenstates. The SM includes only left-handed neutrinos, as described previously,
 328 while all other fermions are present in both left-handed and right-handed spinors. Neu-
 329 trino mass may be explained by the presence of right-handed neutrinos which the SM does
 330 not include. Through the see-saw mechanism, right-handed neutrinos may also provide
 331 resolution to the unnaturally-small neutrino masses, orders of magnitude smaller than the
 332 other fermions. Alternatively, neutrinos may be Majorana fermions, particles which are
 333 their own antiparticle. The origin of neutrino masses and the question of why their mass
 334 is so small require explanation from BSM physics.

335

336 On larger scales, there are two troubling issues with the SM. Firstly, the SM predicts
 337 that at the Big Bang, the creation of the Universe, matter and antimatter should have
 338 been produced in equal quantity. If this were indeed true, the matter and antimatter
 339 should have all annihilated into photons ($f\bar{f} \rightarrow \gamma$), leaving a radiation dominated uni-
 340 verse devoid of matter. However, at the present day, we can see this is not true. This
 341 matter-antimatter asymmetry is unexplained within the SM. The Sakharov conditions [15]
 342 enable the necessary excess of baryons over antibaryons, to be produced, known as baryo-
 343 genesis. The conditions state that a process can result in a matter-antimatter asymmetry
 344 if it violates baryon-number conservation, charge symmetry (C) and charge-parity (CP)
 345 symmetry. BSM models such as SUSY and GUTs can provide additional particles which
 346 satisfy the Sakharov conditions, hence explaining the matter-antimatter asymmetry.

347

348 Observations of anomalous gravitational behaviour, such as in the rotational curves of
 349 galaxies, enable us to infer the existence of DM. Since we do not *visibly* observe DM, it is
 350 inferred that DM does not interact electromagnetically, therefore being electrically-neutral.
 351 It is also required for DM to be stable, as its effects are observed from the early universe in
 352 the cosmic microwave background (CMB), the residual radiation from the Big Bang, until
 353 now.

354

355 Recent measurements of the DM abundance estimate that $\Omega_{DM}h^2 = 0.1196 \pm 0.0031$,
 356 meaning that DM makes up as much as 26% of the universe. The only DM candidate
 357 within the SM are neutrinos as they are massive (inferred from neutrino mixing), neutral
 358 and stable. Therefore, neutrinos actually form part of the DM density. However, their
 359 contribution can be estimated as $\Omega_\nu h^2 \approx \frac{\sum_i m_i}{91\text{eV}} < 0.003$, a minor contribution to the total
 360 DM abundance.

361 1.2 Physics Beyond the Standard Model

362 There are countless proposed extensions to the SM, each which can provide solutions to
 363 some of the open questions. One such method is to postulate a DM candidate, and couple

364 it to the SM through some mediator. Section ?? describes one such model. Another way
365 of generating New Physics is to extend the symmetries of the SM. One such extension is
366 supersymmetry (SUSY), which is described in Section ??.

367 **Supersymmetry**

368 SUSY introduces an additional symmetry to the SM in which SM fermions can become
369 bosons and SM bosons can become fermions. An operator, Q , is introduced which enables
370 transformations between bosonic and fermionic states, as follows:

$$\begin{aligned} Q|\text{boson}\rangle &= |\text{fermion}\rangle \\ Q|\text{fermion}\rangle &= |\text{boson}\rangle . \end{aligned} \tag{1.2.1}$$

371 The symmetry group of SUSY is of the form $SU(3)_C \times SU(2)_L \times U(1)_Y \times \text{SUSY}$ such that
372 when a SM particle undergoes a SUSY transformation, the SM quantum numbers are un-
373 changed. Under this symmetry group, each of the SM particles gains a superpartner with
374 spin differing by $1/2$. The SM particles and their superpartners can be placed into either
375 chiral multiplets or gauge multiplets.

376

377 The SM fermions and their bosonic, spin-0 superpartners form chiral multiplets. The
378 superpartners to the SM fermions have an ‘s’ prepended to their name, short for scalar.
379 For example, the superpartner to the SM top quark is named the ‘stop’ quark. The SM
380 bosons have ‘ino’ appended to their name, an example of this being the superpartners to
381 the SM gluon being named gluinos. The SM vector bosons and their superpartners form
382 gauge multiplets. In order to give masses to all of the particles, SUSY requires two Higgs
383 doublets with weak isospin $Y = \pm 1/2$. This extended Higgs sector gives rise to four gauge
384 eigenstates to the Higgs scalars: \tilde{H}_u^+ , \tilde{H}_u^0 , \tilde{H}_d^0 and \tilde{H}_d^- . These four eigenstates mix to
385 form five mass eigenstates: h^0 , H^0 , A^0 and H^\pm . The SM Higgs boson discovered in 2012
386 is identified as the lightest CP-even SUSY Higgs, h^0 , while the remaining mass eigenstates
387 are much higher masses and are decoupled. A summary of the chiral supermultiplets and
388 gauge supermultiplets are shown in Tables 1.2 and 1.3, respectively.

Names	Symbol	Spin-0	Spin-1/2	$SU(3)_C \times SU(2)_L \times U(1)_Y$
squarks, quarks (3 generations)	Q	$(\tilde{u}_L \tilde{d}_L)$	$(u_L d_L)$	$(\mathbf{3}, \mathbf{2}, \frac{1}{6})$
	\bar{u}	\tilde{u}_R^*	u_R^\dagger	$(\bar{\mathbf{3}}, \mathbf{1}, -\frac{2}{3})$
	\bar{d}	\tilde{d}_R^*	d_R^\dagger	$(\bar{\mathbf{3}}, \mathbf{1}, \frac{1}{3})$
sleptons, leptons (3 generations)	L	$(\tilde{\nu} \tilde{e}_L)$	(νe_L)	$(\mathbf{1}, \mathbf{2}, -\frac{1}{2})$
	\bar{e}	\tilde{e}_R^*	e_R^\dagger	$(\mathbf{1}, \mathbf{1}, 1)$
Higgs, higgsinos	H_u	$(H_u^+ H_u^0)$	$(\tilde{H}_u^+ \tilde{H}_u^0)$	$(\mathbf{1}, \mathbf{2}, +\frac{1}{2})$
	H_d	$(H_d^0 H_d^-)$	$(\tilde{H}_d^0 \tilde{H}_d^-)$	$(\mathbf{1}, \mathbf{2}, -\frac{1}{2})$

Table 1.2: Chiral supermultiplets in the MSSM.

Names	Spin-1/2	Spin-1	$SU(3)_C \times SU(2)_L \times U(1)_Y$
gluino, gluon	\tilde{g}	g	$(\mathbf{8}, \mathbf{1}, 0)$
winos, W bosons	$\tilde{W}^\pm \tilde{W}^0$	$W^\pm W^0$	$(\mathbf{1}, \mathbf{3}, 0)$
bino, B boson	\tilde{B}^0	B^0	$(\mathbf{1}, \mathbf{1}, 0)$

Table 1.3: Gauge supermultiplets in the MSSM.

389 **Mixing of mass eigenstates**

390 The gauge eigenstates listed in Tables 1.2 and 1.3 are able to mix, resulting in mass eigen-
 391 states which are different from the gauge eigenstates. The gauge and mass eigenstates are
 presented in Table 1.4, showing the mixing between the gauge eigenstates.

Names	Spin	Gauge Eigenstates	Mass Eigenstates
Higgs bosons	0	$H_u^+, H_u^0, H_d^0, H_d^-$	h^0, H^0, A^0, H^\pm
Charginos	1/2	$\tilde{W}^\pm, \tilde{H}_u^+, \tilde{H}_d^-$	$\tilde{\chi}_1^\pm, \tilde{\chi}_2^\pm$
Neutralinos	1/2	$\tilde{H}_u^0, \tilde{H}_d^0, \tilde{W}^0, \tilde{B}^0$	$\tilde{\chi}_1^0, \tilde{\chi}_2^0, \tilde{\chi}_3^0, \tilde{\chi}_4^0$
		$\tilde{e}_L, \tilde{e}_R, \tilde{\nu}_e$	same
Sleptons	0	$\tilde{\mu}_L, \tilde{\mu}_R, \tilde{\nu}_\mu$	same
		$\tilde{\tau}_L, \tilde{\tau}_R, \tilde{\nu}_\tau$	$\tilde{\tau}_1, \tilde{\tau}_2, \tilde{\nu}_\tau$
		$\tilde{u}_L, \tilde{u}_R, \tilde{d}_L, \tilde{d}_R$	same
Squarks	0	$\tilde{c}_L, \tilde{c}_R, \tilde{s}_L, \tilde{s}_R$	same
		$\tilde{t}_L, \tilde{t}_R, \tilde{b}_L, \tilde{b}_R$	$\tilde{t}_1, \tilde{t}_2, \tilde{b}_1, \tilde{b}_2$
Glauino	0	\tilde{g}	same

Table 1.4: Table showing the SUSY gauge and mass eigenstates.

392

393

394 As shown in Table 1.4, mixing occurs between the superpartners of the electroweak gauge
 395 bosons and Higgs bosons, the squarks and sleptons. For the squarks and sleptons, the

396 mixing of the SUSY gauge eigenstates is proportional to the mass of their SM counter-
 397 parts, and as such is only relevant for the superpartners of the top and bottom quarks and
 398 the tau lepton. The L and R subscripts denote that there are superpartners for both the
 399 left-handed and right-handed fermions, and do not denote the handedness of the super-
 400 partners themselves. The winos, bino and Higgsinos can mix to form a rich spectrum of
 401 electroweak mass eigenstates. The bino, \tilde{B}^0 , the neutral wino \tilde{W}^0 and the neutral higgs-
 402 sinos \tilde{H}_u^0 and \tilde{H}_d^0 can mix to form four neutral mass eigenstates known as neutralinos. The
 403 charged winos, \tilde{W}^\pm and the charged higgsinos \tilde{H}_u^\pm and \tilde{H}_d^\pm can mix to form two charged
 404 mass eigenstates known as charginos. The neutralinos, denoted by $\tilde{\chi}_i^0$, where $i = 1, 2, 3, 4$,
 405 while the charginos are denoted by $\tilde{\chi}_i^\pm$, where $i = 1, 2$. By convention, the charginos and
 406 neutralinos are labelled in ascending mass. The lightest neutralino, $\tilde{\chi}_1^0$, is generally the
 407 lightest supersymmetric particle (LSP). The production cross-section for squarks, sleptons,
 charginos and neutralinos is shown in Figure 1.7. In the R-parity conserving case, the LSP

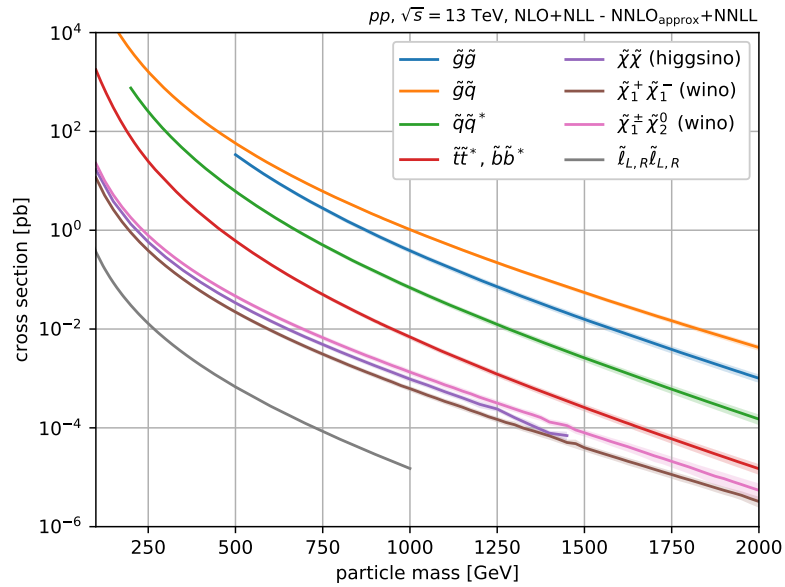


Figure 1.7: Figure showing the production cross-sections for pairs of SUSY particles at $\sqrt{s} = 13$ TeV.

408

409 is stable while the heavier charginos and neutralinos ($\tilde{\chi}_2^\pm, \tilde{\chi}_{3,4}^0$) can decay through a chain
 410 of decays until a final state containing LSPs and SM particles is reached. The two-body
 411 decay chains of charginos and neutralinos are shown in Figure 1.8, assuming that the di-
 412 agrams containing H^0, A^0 and H^\pm are disfavoured compared to diagrams with h^0 due to
 413 its lower mass, and that squarks are heavy and hence also disfavoured. In the case that
 414 the diagrams shown are kinematically-forbidden, decays can proceed via three-body decays
 415 involving SM fermions.

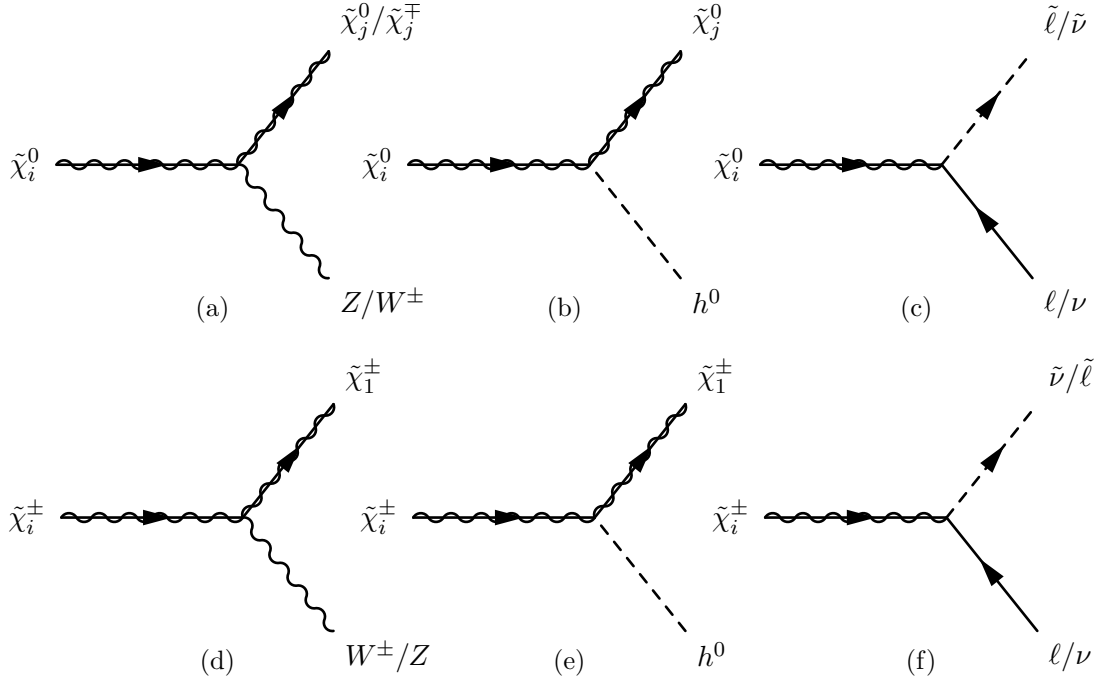


Figure 1.8: Diagrams showing the two-body decays of a given neutralino, $\tilde{\chi}_i^0$ (1.8a, 1.8b and 1.8c) and chargino, $\tilde{\chi}_i^\pm$ (1.8d, 1.8e and 1.8f).

416 Unification of fundamental interactions

417 As previously discussed, it was shown by Glashow, Salam and Weinberg that the electro-
 418 magnetic and weak interactions unify above the electroweak scale, resulting in the combined
 419 electroweak interaction. It is postulated that above some grand unified theory (GUT) scale,
 420 the electromagnetic, weak and strong forces unify. However, in the SM, the evolution of
 421 the couplings of the three forces never converge. However, as described, SUSY introduces
 422 additional particles which alter the running of the coupling constants, allowing them to
 423 unify at the GUT scale. The running of the couplings are shown in Figure 1.9 for both the
 424 SM and SUSY.

425 Resolution to the hierarchy problem

426 As previously discussed, the squared-mass of the Higgs boson, m_H^2 , is comprised of two
 427 components; a bare mass, $m_{H,\text{bare}}^2$, and the quantum corrections to the Higgs mass through
 428 fermion couplings, δm_H^2 . The correction to the Higgs mass for a given fermion, f , is given
 429 by

$$\delta m_{H,f}^2 = \frac{|y_f|^2}{16\pi^2} [-2\Lambda_p^2 + 6m_f^2 \ln(\Lambda_p/m_f)] , \quad (1.2.2)$$

430 where, m_f is the mass of the fermion and y_f is the Yukawa coupling of that fermion to the
 431 Higgs boson. From Equation 1.2.2, it is evident that the top quark which has $y_f \approx 1$, yields

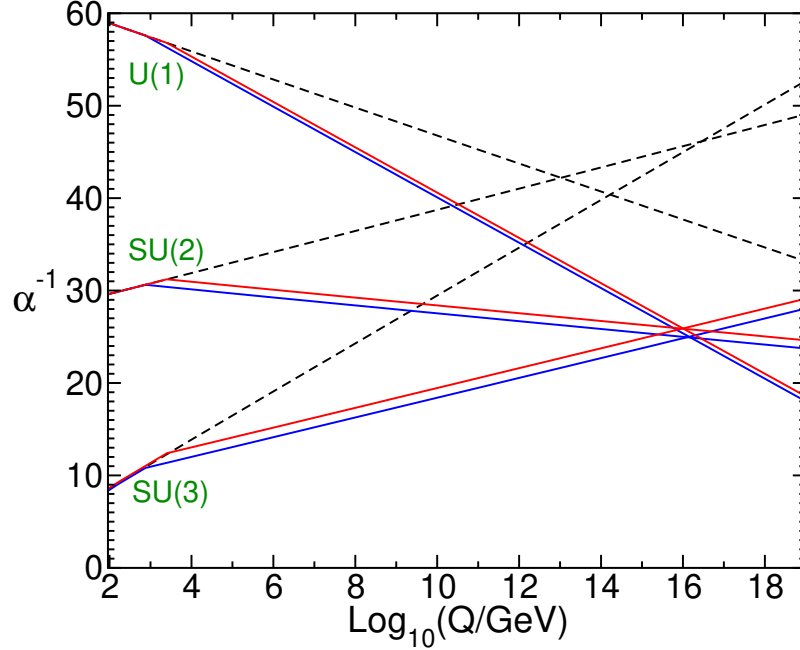


Figure 1.9: Diagram showing how the coupling constants evolve in SM-only (dashed) and SUSY (solid) scenarios. For the SUSY particles, the masses are varied from 750 GeV to 2.5 TeV.

432 the largest correction at around 30 orders of magnitude larger than the measured Higgs
 433 squared-mass, meaning there is either a high degree of ‘fine-tuning’ or there are additional
 434 quantum corrections from New Physics. SUSY introduces two scalars for each SM fermion
 435 (one for each of the left- and right-handed fields). The correction to the Higgs mass for a
 436 scalar, S is given by

$$\delta m_{H,f}^2 = \frac{\lambda_S}{16\pi^2} [\Lambda_p^2 - 2m_S^2 \ln(\Lambda_p/m_S)] , \quad (1.2.3)$$

437 where m_S is the mass of the scalar and $\lambda_S = |y_f^2|$. Assuming that the scalars have the same
 438 masses as their SM counterparts, the quadratic component of the corrections to the Higgs
 439 mass exactly cancel. However, if the superpartners and their SM particles have identical
 440 masses, observations of SUSY particles would have been made long before the LHC. At
 441 the time of writing however, no observation of a SUSY particle has been made. In light of
 442 this, it can be inferred that SUSY must be a spontaneously broken symmetry, in a similar
 443 manner to the electroweak symmetry of the SM. The exact mechanism through which this
 444 occurs is not yet known. However, it is possible to break the SUSY symmetry ‘by hand’
 445 by introducing additional terms in the Lagrangian, as follows:

$$\mathcal{L} = \mathcal{L}_{\text{SUSY}} + \mathcal{L}_{\text{soft}} . \quad (1.2.4)$$

446 In Equation 1.2.4, $\mathcal{L}_{\text{SUSY}}$ contains all of the Yukawa and gauge interactions, while $\mathcal{L}_{\text{soft}}$
 447 contains coupling parameters with positive mass and gauge parameters. The preservation
 448 of the unbroken SUSY is very important for the resolution of the hierarchy problem, as
 449 described in the following section.

450 R-parity

451 SUSY introduces an additional quantum number, known as R-parity, R_p . The R-parity
 452 is constructed using the spin (S), the baryon number (B) and lepton number (L) of the
 453 incoming and outgoing particles from an interaction vertex. The R-parity is defined as:

$$R_P = (-1)^{3(B-L)+2S} . \quad (1.2.5)$$

454 Using Equation 1.2.5, it can be seen that the SM particles all have $R_P = +1$, while
 455 the SUSY particles have $R_P = -1$. In SUSY models which conserve R-parity, processes
 456 which violate lepton and baryon number conservation are disallowed, which prevents the
 457 rapid decay of protons to leptons + mesons, a result which is consistent with experimental
 458 observation. The conservation of R-parity has three important consequences:

- 459 • The LSP is required to be stable. In models where the LSP is neutral and weakly-
 460 interacting with the SM, it becomes an excellent candidate for Dark Matter.
- 461 • Each SUSY particle must decay via a chain containing an odd number of LSPs,
 462 mostly just one.
- 463 • SUSY particles are pair-produced in pp collisions.

464 Extended Higgs sector and Dark Matter

465 In addition to producing DM through the decay of SUSY particles, models with extended
 466 Higgs sectors can provide a way in which DM can couple to the SM, through the addition
 467 of a mediator.

468 Chapter 2

469 The LHC and the ATLAS 470 Experiment

471 The physics analyses detailed in the forthcoming chapters made use of data collected by
472 the ATLAS detector, one of the four main experiments situated around the Large Hadron
473 Collider (LHC) at the European Organisation for Nuclear Research (CERN). CERN is
474 home to the the largest particle physics experiment to date, the LHC. Lying beneath the
475 Franco-Swiss border at a depth of around 100m, it spans a circumference of almost 27km.
476 The LHC is a hadron-hadron collider, accelerating counter-circulating beams of protons
477 (or heavy-ions for a short period every year) to provide collisions at four interactions
478 points around the LHC; ATLAS, CMS, LHCb and ALICE. This thesis focuses entirely on
479 proton-proton collisions recorded by the ATLAS experiment.

480 2.1 The LHC accelerator

481 The protons for the LHC beams are provided by a bottle of hydrogen gas. Protons are
482 isolated by applying a strong electric field to hydrogen atoms, stripping away the electrons.
483 These isolated protons are then transferred to a linear accelerator (LINAC2), where they
484 undergo the initial acceleration to 50 MeV. Proton acceleration is achieved using Radio
485 Frequency (RF) cavities. In the Proton Synchrotron (PS), the proton beam is divided into
486 proton packets known as ‘bunches’, spaced by 25ns intervals, with each bunch containing
487 around $\mathcal{O}(10^{11})$ protons. The 50 MeV proton bunches are further accelerated to an energy
488 of 1.4 GeV by the Proton Synchrotron Booster (PSB) and subsequently to an energy
489 of 25 GeV by the PS. The Super Proton Synchrotron (SPS) is the penultimate stage of
490 acceleration, accelerating the 25 GeV proton bunches to an energy of 450 GeV. These
491 proton bunches are injected into the LHC to produce two counter-circulating beams and
492 are accelerated from 450 GeV to 6.5 TeV by RF cavities.

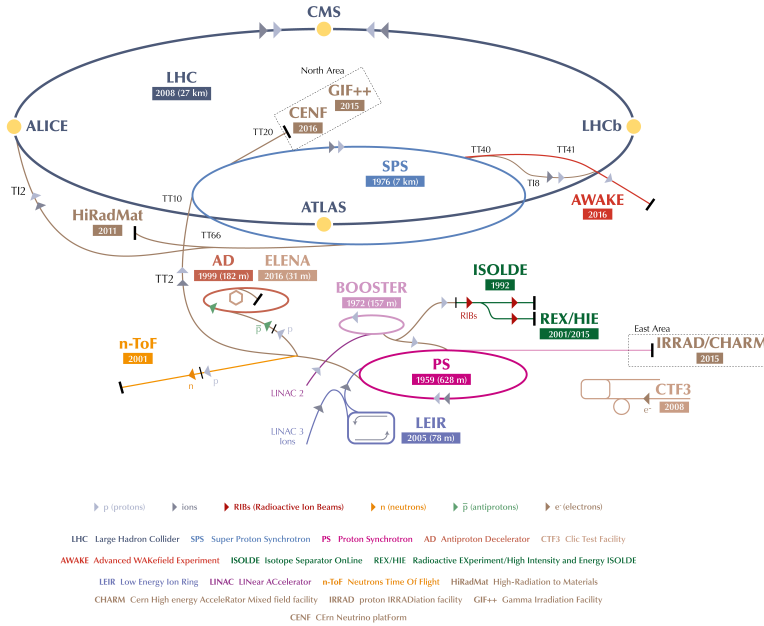


Figure 2.1: A diagram of the CERN accelerator complex. Of importance to the LHC accelerator are LINAC2, PSB, PS, SPS and LHC. [16]

2.2 Luminosity and pileup

The amount of data being delivered by LHC and recorded by its experiments is measured by the *luminosity*. The instantaneous luminosity, \mathcal{L} , of a beam is defined as the number of incident particles per square centimetre per second [$\text{cm}^{-2}\text{s}^{-1}$]. For a circular collider, the expression for the instantaneous luminosity of two colliding beams is given by [17]:

$$\mathcal{L} = f \frac{N_p^2 n_b}{4\pi\sigma_x\sigma_y} F . \tag{2.2.1}$$

In Equation 2.2.1, N_p is the number of protons per bunch, n_b the number of bunches in each beam, f the frequency of bunch crossings ($1/25\text{ns} = 40\text{MHz}$), σ the size of the bunch at the interaction point (IP) and F a geometrical correction factor accounting for a non-zero crossing angle at the IP. The integrated luminosity (often shortened to ‘luminosity’), is defined as the time-integral of the instantaneous luminosity: $L = \int \mathcal{L} dt$.

The luminosity is a measure of the total number of incident particles in a given area in a given time period and has units of an inverse area in square centimetres [cm^{-2}]. However, due to the huge number of incident particles every second, these units are rarely used; instead, integrated luminosity is often quoted in units of ‘barns’, where 1 barn (b) is defined as 10^{-24}cm^2 . For a cross-section quoted in barns, the total number of expected

509 events, N_{exp} , in a dataset with integrated luminosity L and cross-section $\sigma_{pp \rightarrow X}$ is given
 510 by $N_{\text{exp}} = \sigma_{pp \rightarrow X} L$.

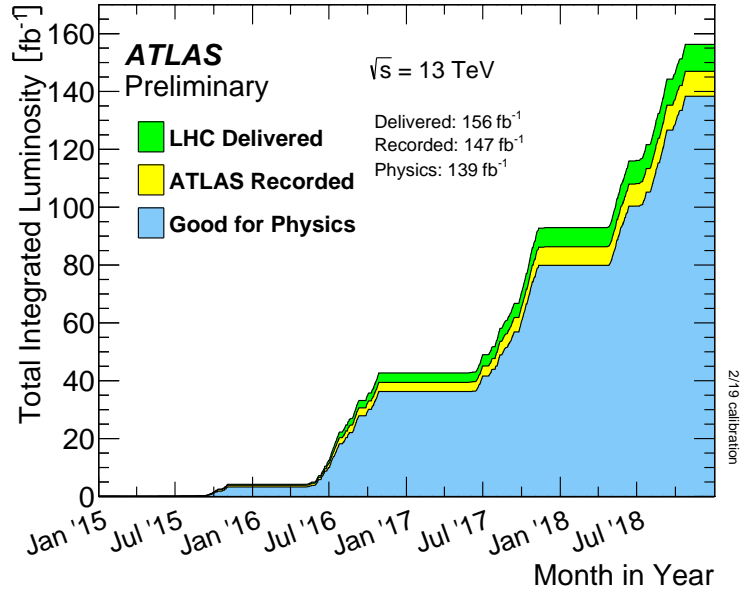


Figure 2.2: Plot showing the total integrated luminosity as a function of time during the Run-2 data-taking period. In total, the LHC delivered 156 fb^{-1} of data, with ATLAS recording 147 fb^{-1} and 139 fb^{-1} being established as suitable for physics analysis.

510

511

512 Due to the bunched beam structure and the intensity of the bunches, multiple inelas-
 513 tic proton-proton collisions are possible per bunch crossing. Pileup is an important effect
 514 in high energy physics experiments such as ATLAS, as large amounts of pileup degrade
 515 the reconstruction performance of an experiment. Pileup events can come from either the
 516 same bunch crossing, known as in-time pileup, or from the bunch crossing just before or
 517 after the bunch-crossing being considered, known as out-of-time pileup. The collision, or
 518 vertex, with at least two tracks and with the highest Σp_T^2 is usually defined as the pri-
 519 mary vertex, or ‘hard scatter’, in an event. All other vertices, and the resultant final state
 520 particles, from the same bunch crossing are considered ‘pileup’ events. Figure 2.3 shows
 521 the pileup profile for each data-taking year for Run-2 of the LHC. The mean number of
 522 interactions per bunch-crossing is taken as the mean of the Poisson distribution of the
 523 number of interactions per bunch-crossing calculated for each bunch. It is calculated using
 524 the per-bunch luminosity, defined as:

$$\mu = L_{\text{bunch}} \times \frac{\sigma_{\text{inel}}}{f_r} . \quad (2.2.2)$$

525 In Eq. 2.2.2, L_{bunch} is the per-bunch instantaneous luminosity, σ_{inel} is the inelastic cross-
 526 section ($\sim 80 \text{ mb}$ for Run-2), and f_r is the bunch-crossing frequency.

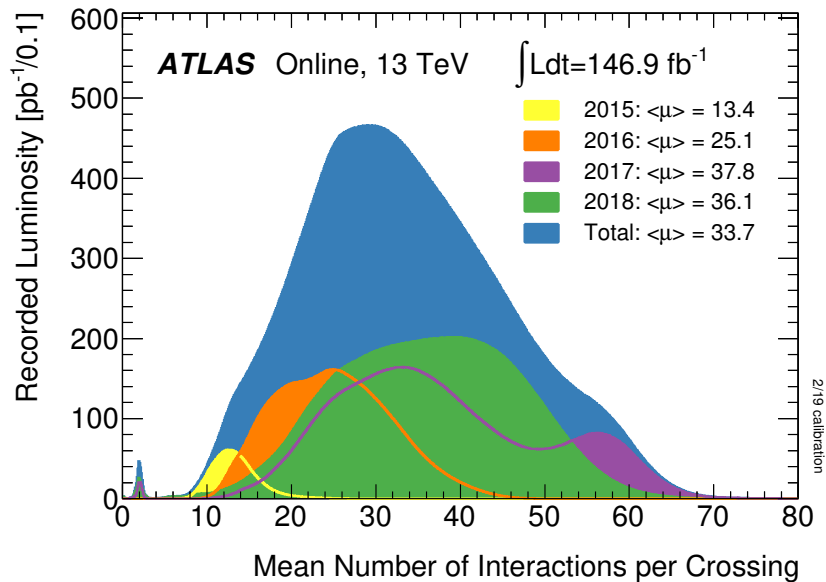


Figure 2.3: Mean number of proton-proton interactions per bunch crossing for Run-2 (2015-2018). The mean number of interactions per bunch-crossing is taken as the mean of the Poisson distribution of the number of interactions per bunch-crossing calculated for each bunch.

2.3 ATLAS overview

ATLAS, *A Toroidal LHC ApparatuS*, is one of the two general purpose detectors (GPDs) and is the largest of all of the LHC experiments, at 44m in length and 25m in width and weighing around 7000 tons. Figure 2.4 shows a schematic diagram of the ATLAS detector and its major subsystems. ATLAS is an almost hermetic detector, providing near-full 4π tracking and calorimetry through multiple detector subsystems. The ATLAS detector design was optimised for [18]:

- High-efficiency for charged particle reconstruction and identification.
- High-precision calorimetry, providing high-precision electron/photon identification and measurement along with accurate hadronic/ E_T^{miss} measurements.
- Precise muon momentum measurements using only the muon system, at even the highest luminosity.
- Ability to trigger on objects with low momentum.

ATLAS has four major subsystems; the Inner Detector (ID), the Electromagnetic Calorimeter (ECAL), the Hadronic Calorimeter (HCAL) and the Muon Spectrometer (MS), arranged in concentric layers about the beam pipe. ATLAS is designed to be symmetric in the forward-backward plane about the interaction point (IP), and when discussed

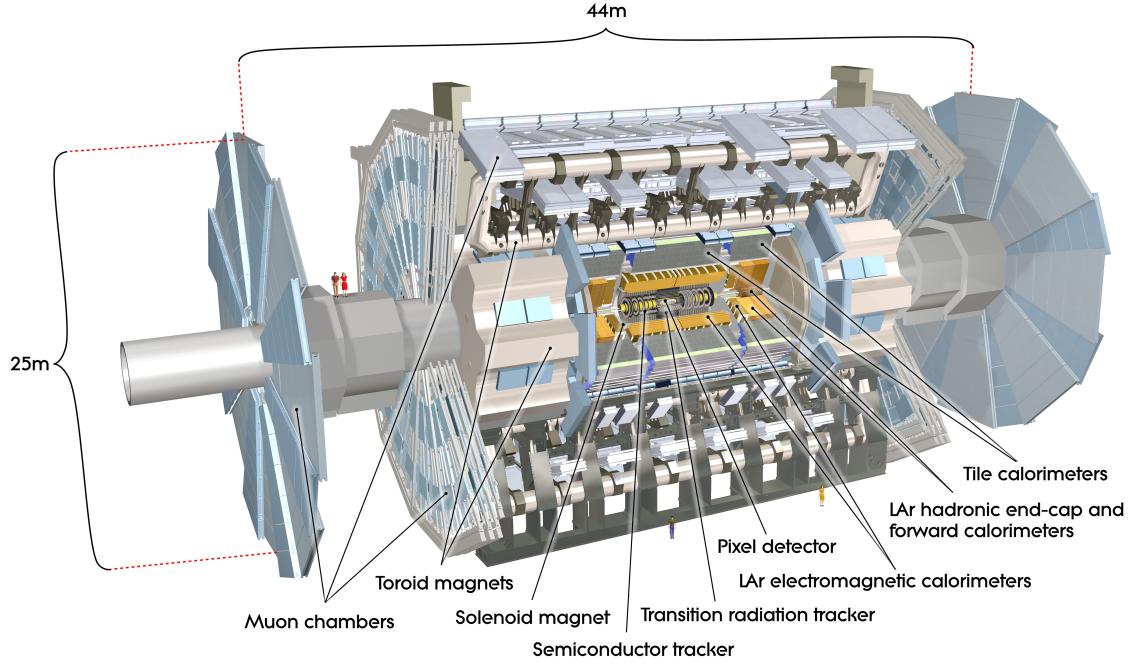


Figure 2.4: Cut-away diagram of the ATLAS detector. [19]

544 is often separated into three segments; the central region, the barrel region and the endcap
 545 region.

546

547 ATLAS uses a ‘right-handed’ coordinate system; the z-axis is defined in the beam di-
 548 rection, with the positive x-axis defined to point from the interaction point to the centre
 549 of the LHC and the positive y-axis being in the upwards direction. Side A of ATLAS, the
 550 side closer to Geneva Airport, is defined with positive z values, and Side C, closer to the
 551 Jura mountains, with negative z values.

552

553 The azimuthal angle, ϕ , and the polar angle, θ , are defined as the angle around the beam
 554 axis and the angle from the beam, respectively. From the polar angle, the pseudorapidity
 555 is defined as $\eta = -\ln \tan(\frac{\theta}{2})$. As the partons are highly boosted in the z-direction, and
 556 the partonic momentum fraction is not exactly known, object measurements are usually
 557 made in the plane perpendicular to the beam, the transverse plane, such as an object’s
 558 transverse momentum, p_T or missing transverse momentum, E_T^{miss} .

559 2.4 Magnet system

560 When a charged particle of charge q moves with velocity v through a magnetic field of
 561 strength $|\vec{B}|$, the force on that particle is given by the Lorentz force,

$$\vec{F} = q\vec{v} \times \vec{B}, \quad (2.4.1)$$

562 where $\vec{v} \times \vec{B}$ denotes the cross-product of the velocity vector of the particle with the vector
 563 describing the magnetic field. Due to the presence of the a cross-product in the Lorentz
 564 force, the force experienced by the charged particle will be perpendicular to both the
 565 velocity vector and the magnetic field. The deflection of particle tracks by the magnet
 566 system enables the measurement of the momentum of an incident particle. The ATLAS
 567 magnet system is constructed from two superconducting magnet systems which enable this;
 568 a central solenoid (CS) which is surrounded by three toroid magnets. A diagram of the
 ATLAS magnet system is shown in Figure 2.5.

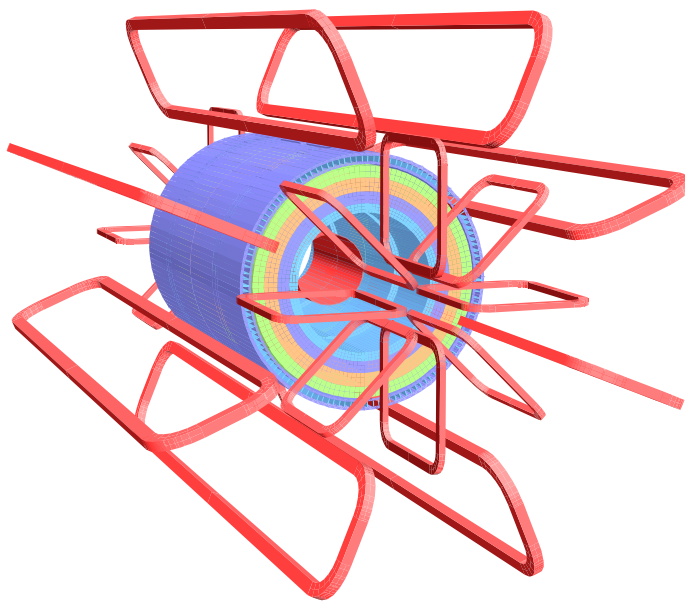


Figure 2.5: Diagram of the ATLAS magnet system, showing the barrel and end-cap toroids in red, while the CS is shown encased by calorimeter layers. [18]

569
 570 The central solenoid (CS) provides a 2T magnetic field to the Inner Detector, peaking
 571 at around 2.6T at the magnet itself. The barrel toroid (BT) and endcap toroid (ECT)
 572 provides a magnetic field between 0.5-1 T for the muon spectrometer, peaking at 3.9T and
 573 4.1T, respectively. Superconductivity of the magnet system is achieved using liquid helium
 574 cooled to around 4.5 K.

575 2.5 Inner Detector

576 The ATLAS Inner Detector (ID), shown in Fig. 2.6, is the innermost layer of the ATLAS
 577 detector. It is designed to provide high-precision tracking, vertex information, and for the
 578 identification of particles. The ID has 3 components; the Pixel detector, the Semiconductor
 579 Tracker (SCT) and the Transition Radiation Tracker (TRT). The Pixel detector and SCT
 580 use silicon pixels and strips, respectively, while the latter uses straw detectors to provide
 581 tracking information. The ID is immersed in a 2T magnetic field provided by the CS,
 582 allowing precise momentum measurement through the measurement of track deflection.
 583 The Pixel and SCT detectors provide coverage in $|\eta| < 2.5$, while the TRT provides further
 584 tracking information up to $|\eta| < 2.0$.

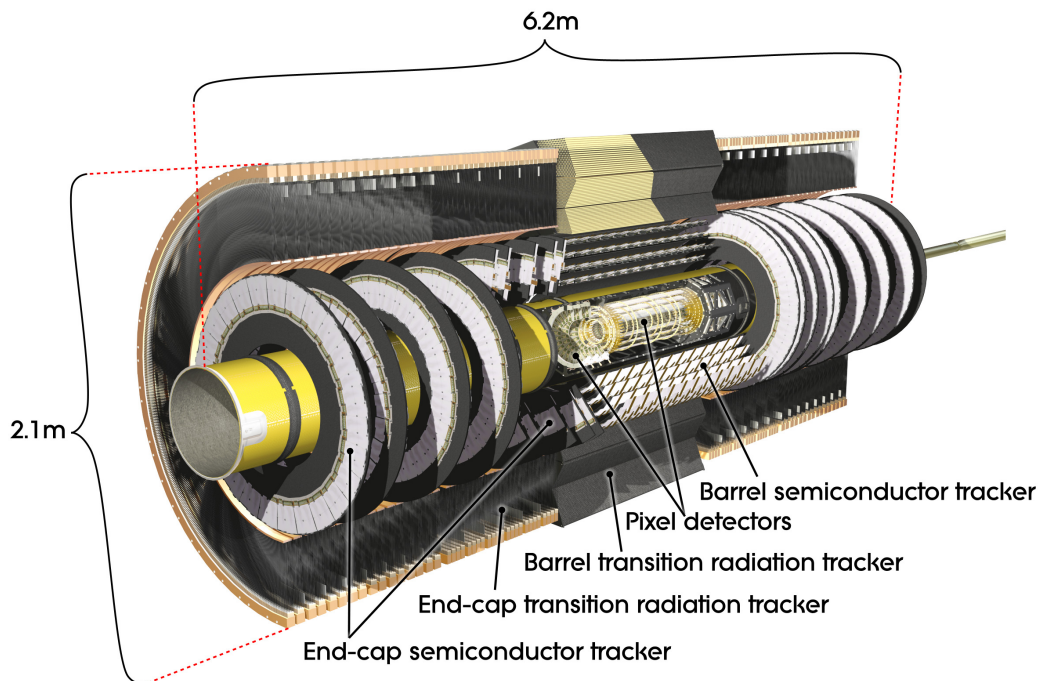


Figure 2.6: Cut-away diagram of the ATLAS Inner Detector. [19]

585 Pixel Detector

586 The Pixel Detector uses silicon semiconductor pixels to register particle hits from incident
 587 particles. Materials which exhibit semiconductive behaviour, such as silicon, have conduc-
 588 tivity between that of an insulator and a conductor. The silicon pixels used in the Pixel
 589 Detector are constructed using a p-n junction. A p-n junction is the boundary between two
 590 silicon semiconductors which are doped to have excess of electrons (n-doped), or an excess
 591 of holes (p-doped). By applying a forward bias voltage to the pixel, the free electrons and
 592 holes can migrate across the junction through the depletion region. Conversely, when ap-
 593 plying a reverse bias, the free electrons and holes are pulled away from the junction. When

Detector component	Modules	Pixel pitch [μm]	Resolution [μm]
Pixel Detector			
IBL	224	50 x 250	8 ($R - \phi$), 40 (z)
Barrel	1456	50 x 400	10 ($R - \phi$), 115 (z)
End-caps	288	50 x 400	10 ($R - \phi$), 115 (R)
SCT			
Barrel	2112	80	17 ($R - \phi$), 580 (z)
End-caps	1976	80	17 ($R - \phi$), 580 (R)

Table 2.1: Table giving a summary of the Pixel Detector and SCT module sizes and resolutions. [18, 20]

594 a sufficient reverse bias is applied, the pixel becomes fully depleted, meaning there is no
595 current flow between the p-doped and n-doped side of the pixel. When a charged particle
596 passes through a pixel, electrons and holes are liberated which drift to the electrodes of
597 the pixel due to applied bias voltage, resulting in the collection of charge which is read out
598 as a particle hit.

599

600 The Pixel Detector is the ID subsystem closest to the IP. It provides high-granularity,
601 high-precision measurements of charged particles at radii as little as 3.3cm from the beam
602 pipe. The system itself is constructed from three barrel modules at radii of $\sim 4\text{cm}$, $\sim 10\text{cm}$
603 and $\sim 13\text{cm}$, with five disks on either side at radii between 11cm and 20cm. The Pixel
604 detector has 1744 silicon pixel sensors with a nominal pixel pitch of $50 \times 400\mu\text{m}^2$ and a
605 thickness of $250\mu\text{m}$. The barrel layers of the Pixel Detector contain 67 million readout
606 channels, and the disks contain a further 13 million.

607

608 Since the initial detector design, a fourth layer has been added to the Pixel Detector,
609 at a radius of $\sim 3\text{cm}$. This layer is known as the ‘Insertable B-Layer’, or IBL. The IBL was
610 developed and installed to improve the tracking and b -tagging performance of the ID in
611 instantaneous luminosity conditions which exceeded the initial Pixel Detector design. The
612 Pixel Detector’s efficiency was expected to degrade due to the additional pileup produced
613 by the higher-than-design instantaneous luminosity, but the inclusion of the IBL helped
614 to combat this efficiency degradation while also providing an improvement to the impact
615 parameter resolution. The pixel sensors used in the IBL have a pitch of $50 \times 250\mu\text{m}^2$. Table
616 2.1 summarises the semiconductor modules used in both the Pixel Detector and SCT.

617 Semiconductor Tracker

618 The SCT surrounds the Pixel detector, using detection techniques similar to that previously
619 described for the Pixel detector. The SCT provides up to eight precision measurements

620 per track, aiding in high-precision measurement of charged particle momentum, as well as
621 contributing to the measurement of the impact parameter and vertex position. The SCT
622 is constructed from eight layers of silicon microstrip detectors, consisting of 4088 modules.
623 The eight layers of barrel SCT modules have a total of 2112 microstrip modules with $80\mu\text{m}$
624 pitch, at radii between 30cm and 52cm. The SCT provides spatial resolution of $16\mu\text{m}$ in $R\phi$
625 and $580\mu\text{m}$ in z , allowing for tracks to be distinguished if they are separated by $\sim 200\mu\text{m}$.

626 Transition Radiation Tracker

627 The TRT is the outermost layer of the ID, sitting at radii between $554\text{mm} < r < 1106\text{mm}$.
628 The TRT is a straw-tube detector, utilising drift tube detectors to provide upto 36 ad-
629 ditional measurements of each track. The drift tubes in the TRT are constructed from
630 Kapton tubes, each of 4mm diameter, with a gold-plated tungsten wire in the centre of
631 each drift tube with a diameter of $31\mu\text{m}$. The wire at the centre of each tube is at ground
632 potential, while the wall of the tubes are at -1.5 kV. The tubes are filled with a mixture
633 of xenon (70%), carbon dioxide (27%) and oxygen (3%). When a charged particle passes
634 through a straw tube, electrons from the gas are liberated through ionisation processes.
635 These electrons then drift toward the wire in the centre of the straw tube. The current
636 flow created by the free electrons is registered as a particle hit. In total, the barrel TRT
637 contains ~ 50000 straws, while the end-caps contain 320000. Polymer fibres and foils fill
638 the gaps between the straws in the barrel and endcap, respectively. The interface between
639 the straws and the polymers used to fill the gaps can cause highly-relativistic particles to
640 emit transition radiation. The probability of the emission of transition radiation depends
641 upon the relativistic factor $\gamma = E/m$, and is hence strongest for lighter particles. Particle
642 identification using transition radiation is performed to distinguish electrons from pions.

643 2.6 Calorimetry

644 The calorimeters in the ATLAS detector are designed to accurately measure the energy
645 of incident particles. The calorimeter system can be separated into the Electromagnetic
646 calorimeter (ECAL), the Hadronic calorimeter and the Forward Calorimeter (FCal) sys-
647 tems, all of which are sampling calorimeters. The ECAL is designed to measure the
648 energies of incident electrons and photons, as well as any electromagnetically-interacting
649 components of jets. The Hadronic Calorimeter is designed for measuring the energy of
650 strongly-interacting objects, namely jets.

651

652 The ATLAS calorimeter systems use alternating layers of absorber material and active
653 detector material. When a particle enters the absorber material of a calorimeter, a cascade
654 of particle decays is initiated, known as a shower. Particles which interact via the EM
655 interaction produce EM showers, in which photons pair-produce electrons and positrons,

656 both of which undergo Bremsstrahlung radiation of photons. Particles which interact via
 657 the strong force produce much more complex showers. Particle-nucleus interactions in the
 658 HCAL can produce additional hadrons, such as pions. Charged hadrons, will lose energy
 659 when traversing the absorber material through ionisation processes. In addition, neutral
 660 pions in their decay to two photons, $\pi^0 \rightarrow \gamma\gamma$, can induce an EM shower component.

661

662 The depth of the ATLAS calorimeters is optimised to contain EM showers within the
 663 ECAL and hadronic showers in the HCAL, hence minimising punch-through into the next
 664 detector layer. The radiation length, X_0 , of a material is the mean length over which an
 665 electron will lose all but $1/e$ of its initial energy, while the interaction length of a material,
 666 λ , characterises the mean distance a hadron will travel through a material before undergo-
 667 ing a nuclear interaction. The depth of each calorimeter is optimised to fully contain their
 668 respective shower type.

669

670 The two calorimeter systems provide full coverage in ϕ and calorimetry in the range
 671 $|\eta| < 4.9$. Complete ϕ coverage is needed for precise reconstruction of E_T^{miss} , a prin-
 672 ciple component of searches using ATLAS. A diagram of the ATLAS calorimeter system
 673 is shown in Fig. 2.7.

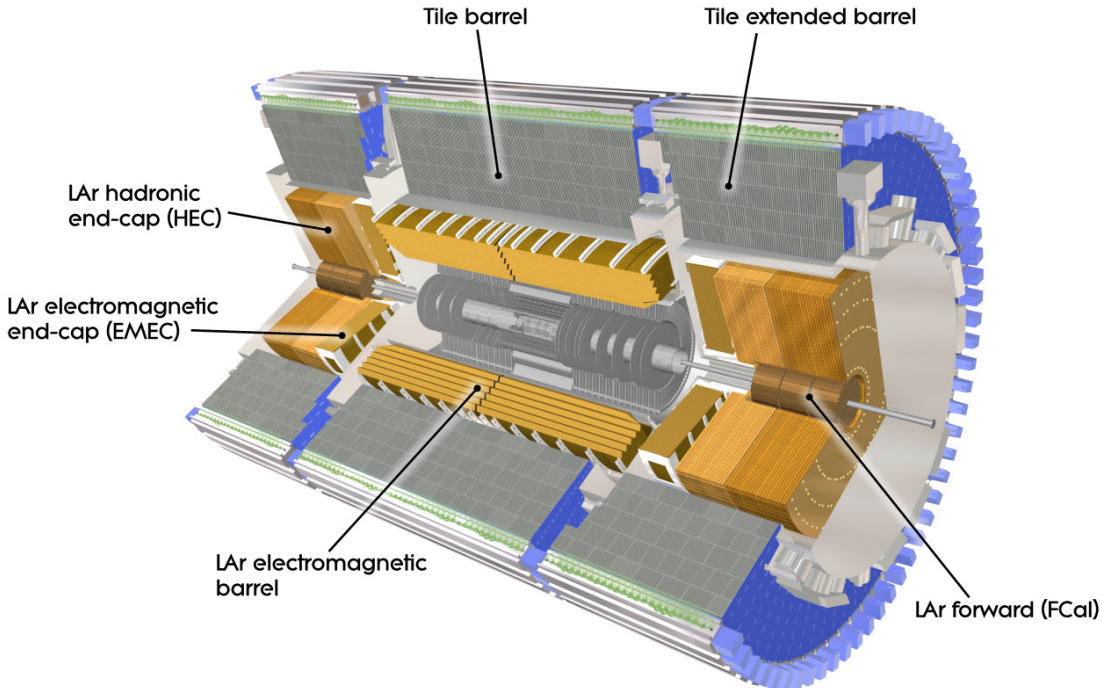


Figure 2.7: Cut-away diagram of the ATLAS Electromagnetic and Hadronic calorimeters. [19]

674 **Electromagnetic Calorimeter**

675 The ECAL is comprised of the barrel EM calorimeter which covers the pseudorapidity range
676 $|\eta| < 1.475$ and the two end-cap EM calorimeters, each covering $1.375 < |\eta| < 3.2$. The
677 ECAL is constructed using lead as the absorber material, while using liquid argon (LAr)
678 as the active material. When a charged particle passes through the LAr, ionisation occurs,
679 producing electrons. Using similar principles to the drift tubes described for the TRT, an
680 electric field is applied, such that the ionisation electrons drift toward the electrodes. The
681 thickness of the ECAL ranges from 22-38 radiation lengths to fully contain EM showers.

682 **Hadronic Calorimeter**

683 The Hadronic Calorimeter, as shown in Figure 2.7, can also be separated into several sub-
684 systems; the scintillating-tile calorimeter (HCAL), the LAr hadronic endcap calorimeter
685 (HEC) and the forward calorimeter (FCal).

686
687 The tile calorimeter covers the range $|\eta| < 1.7$ and sits adjacent to the the ECAL. It
688 is separated into a central barrel and two extended barrels. Each of these barrels is com-
689 prised of 64 modules with a size of $\Delta\phi \sim 0.1$ made of steel plate absorbers and scintillating
690 plastic tiles. When charged particles pass through these scintillating tiles, photons with UV
691 wavelengths are produced from polystyrene. These photons are absorbed and re-emitted
692 as visible-light photons by wavelength-shifting fluors. This light is collected by fibres and
693 is transmitted to photomultiplier tubes (PMTs).

694
695 The HEC is similar in construction to the ECAL, using LAr as the active medium, but
696 instead of using lead as an absorber, uses copper. The HEC provides coverage in the range
697 $1.5 < |\eta| < 3.2$. The HEC is constructed with two sets of wheels, one per end-cap, HEC1
698 and HEC2, respectively. Each of the four HEC wheels (a front and back wheel per end-cap)
699 is constructed from 32 identical wedge-shaped modules.

700 **Forward Calorimeter**

701 The FCal provides coverage over $3.1 < |\eta| < 4.9$. Each FCal is split into three components;
702 FCal1 is an electromagnetic module, while FCal2 and FCal3 are hadronic modules. FCal1
703 uses copper as an absorber material, whereas FCal2 and FCal3 use tungsten. All FCal
704 modules use LAr as the active component.

705 **2.7 Muon System**

706 The Muon Spectrometer (MS) is the outermost part of ATLAS. Muons pass through the
707 entire ATLAS detector before decaying, with a flight distance of $c\tau \sim 700\text{m}$, and do not

708 undergo EM showering in the same way as electrons or photons. The main purpose of the
 709 MS is to detect charged particles escaping the calorimeter systems and measure their mo-
 710 mentum within the $|\eta| < 2.7$ range, also providing triggering capabilities within $|\eta| < 2.4$.

711

712 The MS comprises four subsystems; Monitored Drift-Tube (MDT) chambers, Cathode
 713 Strip Chambers (CSCs), Resistive Plate Chambers (RPCs) and Thin Gap Chambers
 714 (TGCs). The 1150 MDTs cover the $|\eta| < 2.7$ range with a resolution of $35\mu\text{m}$ per cham-
 715 ber. At the innermost layer of the MS, the MDTs are replaced by CSCs in the range
 716 $2.0 < |\eta| < 2.7$ due to their higher rate capability. The CSCs have a z resolution of $40\mu\text{m}$,
 717 and a ϕ resolution of 5mm.

718

719 The triggering capability of the MS is provided by the RPCs and TGCs in the barrel
 720 and endcaps, respectively. The RPCs have a spacial resolution in z (ϕ) of 10mm (10mm)
 721 and a temporal resolution of 1.5ns, while the TGCs have a spacial resolution in R (ϕ) of
 722 2-6mm (3-7mm) and a temporal resolution of 4ns.

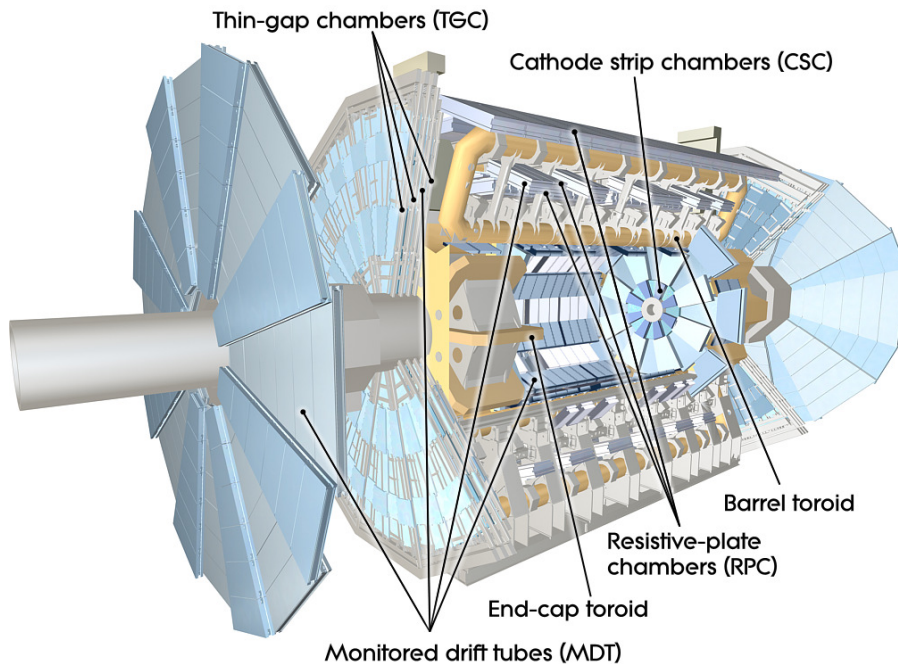


Figure 2.8: Cut-away diagram of the ATLAS Muon Spectrometer. [19]

723 2.8 ATLAS Trigger System

724 The temporal bunch-separation provided by LHC in Run-2 is 25ns, meaning the proton-
 725 proton bunch-crossing frequency is 40 MHz. However, saving all of these events to disk
 726 is not possible due to the huge bandwidth and storage required, with each event requir-

727 ing around 1.3MB of storage. Therefore, events which are deemed ‘uninteresting’ are not
 728 stored. To achieve this, ATLAS employs a trigger system, which makes rapid decisions on
 729 whether to save the event to disk.

730

731 The ATLAS trigger system consists of the Level-1 (L1) hardware trigger and the software-
 732 based High-Level trigger (HLT). The L1 trigger uses coarse detector information from the
 733 calorimeters and MS to identify muons, electrons, photons, jets and hadronically-decaying
 734 taus with high transverse momentum, or events containing large amounts of total trans-
 735 verse energy and E_T^{miss} . The L1 trigger uses a subset of the ATLAS subsystems; the RPC
 736 and TGC are used for muons, while the calorimeter subsystems are used for EM clusters,
 737 jets, tau leptons, E_T^{miss} and large total transverse energy. The L1 trigger operates at a
 738 maximum of 100kHz, with each decision being made in less than $2.5\mu\text{s}$. Regions-of-interest
 739 (RoIs) are identified by the L1 trigger; these are regions in η and ϕ containing potential
 740 physics objects. These RoIs are used as seeds in the HLT.

741

742 The software based HLT takes the full event information from the L1 RoI seeds and in-
 743 vestigates the RoIs. The event reconstruction used in the HLT is then used to accept or
 744 reject the event. The HLT further reduces the event rate to around 1.5kHz. A functional
 745 diagram of the trigger and data acquisition system is shown in Figure 2.9.

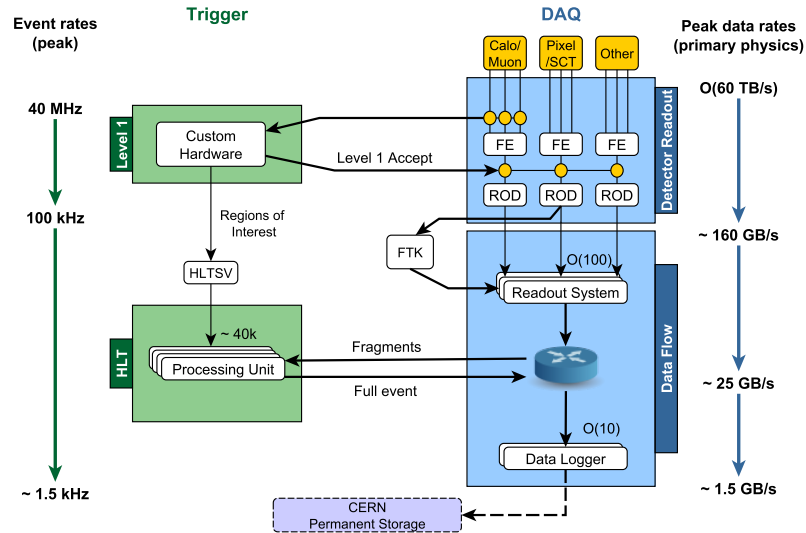


Figure 2.9: A functional diagram of the ATLAS trigger and data acquisition system (TDAQ). The diagram shows the flow of data from detector readout, through the L1 trigger, to the HLT and eventual disk storage. The steps following this are discussed in Chapter 4.

Chapter 3

Data and Monte Carlo samples

This Chapter discusses the datasets used in the physics analyses detailed in Chapter 6 and 7, discussing the running conditions during data-taking and the triggers used to collect the data. Along with the datasets, the procedure through which Monte Carlo (MC) samples are generated is discussed, along with a brief discussion of the generators used in the analyses in the subsequent Chapters. Finally, this Chapter discusses the complexities of simulating the single top Wt -channel process due to interference with the $t\bar{t}$ process, an effect which can generate uncertainties of $\mathcal{O}(100\%)$ on the predictions of the single top background. Studies are performed to quantify the impact of the interference in the analyses detailed in Chapters 6 and 7, where the single top process is one of the major SM backgrounds.

3.1 Datasets

The physics analyses discussed in Chapters 6 and 7 used data collected during the Run-2 data-taking period (2015-2018) in pp collisions at $\sqrt{s} = 13$ TeV, accumulating 139fb^{-1} ($\pm 1.7\%$) of collision data in total. The physics analysis described in Chapter 6 used a subset of this data, taken in 2015-2016, with a total integrated luminosity of 36.1fb^{-1} ($\pm 2.1\%$). The primary measurement of the luminosity is recorded by the LUCID detector [21], which sits 17m from the interaction point on both the A and C side of ATLAS and measures the visible number of interactions per bunch-crossing. In Run-2, proton bunches are separated by 25ns, compared to 50ns in Run-1. Each proton bunch contains $\mathcal{O}(10^{11})$ protons and as such each bunch-crossing can have multiple inelastic pp interactions. Each proton-proton collision which produces at least two tracks with $p_T > 0.4$ GeV is classed as an interaction point, being referred to as a collision vertex. The collision vertex in each bunch-crossing which has the highest $\sum p_T^2$ of tracks is identified as the Primary Vertex (PV). All other vertices are considered a background to the primary vertex, known as ‘pileup’, which is described in further detail in Chapter 2. Pileup at the LHC is one of the greatest challenges for accurate track reconstruction, and will continue to be so in the HL-LHC phase of operation. The pileup conditions for Run-2 are shown in Figure 2.3.

774 **Triggers**

775 As previously discussed, it is not possible to save all events to disk due to the huge band-
776 width required to readout, partially-reconstruct and trigger on events in real-time. Events
777 passing a L1 trigger are selected and processed with the HLT, and thus events are col-
778 lected at a reduced rate of approximately 1.5kHz. This reduced event rate integrated over
779 Run-2 still provides a huge dataset in which to search for evidence of New Physics. For
780 the New Physics models considered in this Thesis, a common signature of the production
781 of BSM particles is the presence of large amounts of E_T^{miss} in an event, due to the presence
782 of non-SM particles in the final state. The analyses described in Chapter 6 and 7 both
783 used E_T^{miss} triggers to select events in data which may contain non-SM particles. Table 3.1
784 shows the list of triggers used in each data-taking year for the analysis detailed in Chapters
6 and 7.

Year	Triggers
2015	HLT_xe70_mht
2016	HLT_xe90_mht_L1XE50
	HLT_xe100_mht_L1XE50
	HLT_xe110_mht_L1XE50
2017	HLT_xe90_pufit_L1XE50
	HLT_xe110_pufit_L1XE55
2018	HLT_xe110_pufit_xe70_L1XE50
	HLT_xe120_pufit_L1XE50
	HLT_xe110_pufit_xe65_L1XE50
	HLT_xe110_pufit_xe70_L1XE50

Table 3.1: A table showing the list of E_T^{miss} triggers used in the analyses described in Chapter 6 and Chapter 7.

785

786 The names of the triggers listed in Table 3.1 hold information of the trigger thresholds
787 and algorithms used. The inclusion of L1XE50, for example, indicates that the event must
788 pass the L1 trigger threshold which is specified by XE50, representing a trigger thresh-
789 old of 50 GeV. The HLT prefix indicates that an event must pass the HLT trigger where
790 the trigger threshold is specified in the form xe110, where the 110 after xe indicates the
791 HLT trigger threshold is 110 GeV. The HLT algorithm used to calculate the E_T^{miss} , which
792 are described in detail in [21], are denoted by mht or pufit where the former calculates
793 the E_T^{miss} based on jets while the latter uses a pileup-suppression technique to estimate
794 the E_T^{miss} . The cell-based algorithm, which uses the uncalibrated energy deposits in the
795 calorimeter to estimate the E_T^{miss} , omits any additional designation from the trigger name.
796 Where two separate xe thresholds are present in a name, the former refers to the threshold
797 for the pufit algorithm, while the latter refers to the threshold for the cell-based algorithm.

798

799 Due to the evolving conditions throughout each year of data-taking, there are frequently
 800 multiple triggers listed per year. These are ‘period-dependent’ triggers, and as instantane-
 801 ous luminosities grow and the pileup profile shifts to higher $\langle\mu\rangle$, as defined in Chapter
 802 2, so too do the trigger thresholds. The efficiency of the E_T^{miss} trigger is determined by,

$$\epsilon(\mathcal{S}_i) = \frac{N(\mathcal{S}_i|\text{trigger})}{N(\mathcal{S}_i)}, \quad (3.1.1)$$

803 where \mathcal{S}_i denotes some event selection criteria, the denominator is the number of events
 804 passing the selection \mathcal{S}_i and the numerator is the subset of those events which also pass
 805 the trigger requirements. When performing searches for New Physics processes which have
 806 low rates compared to the SM backgrounds, a high-trigger efficiency is required to retain
 807 as many candidate signal events as possible. The efficiency of the E_T^{miss} trigger in the years
 2015-2018 is shown in Figure 3.1 as measured in $Z \rightarrow \mu\mu$ events.

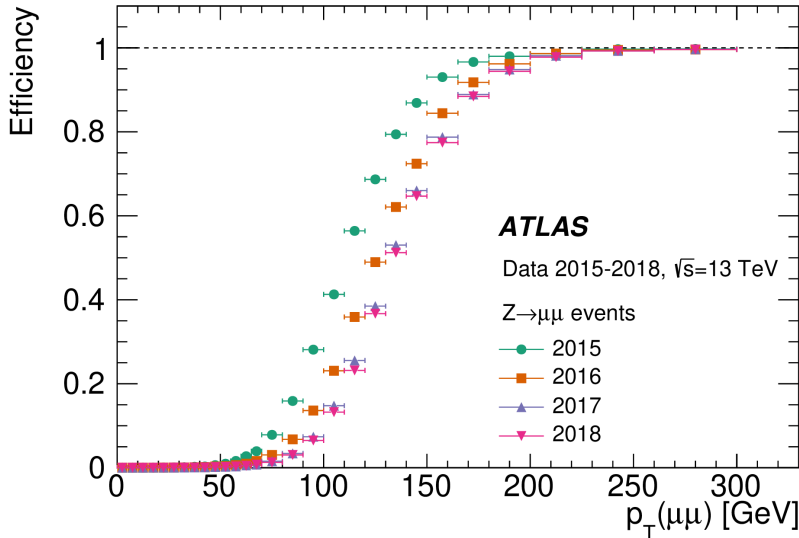


Figure 3.1: A plot showing the efficiency of the lowest unrescaled E_T^{miss} trigger from 2015-2018, known as the ‘turn-on’ curve.

808

809

810 In order to ensure the trigger accepts events in data and from all MC processes with
 811 equal efficiency, the analyses detailed in Chapters 6 and 7 require all events are on the
 812 trigger ‘plateau’, the region of constant efficiency, shown in the ‘turn-on’ curve in Figure
 813 3.1 at values above 200 GeV.

3.2 Monte Carlo simulation

An accurate, precise simulation procedure is required in order to make meaningful comparisons between SM predictions and the data collected by ATLAS. This is known as Monte Carlo (MC) simulation. A generic MC simulation works by randomly sampling a process-specific distribution many times to obtain a sample of predictions for that process. In the context of this Thesis, MC simulation is used to produce simulated samples of SM and BSM processes, produced at the LHC and subsequently detected by ATLAS. This simulation process is known as *event generation*.

MC event generation

Typically, the procedure for simulating physical processes through MC simulation involves: *matrix element calculations (ME)*, *parton showering (PS)*, *hadronisation* and simulation of the *underlying event (UE)*. This chain is represented in Figure 3.2.

The composite nature of protons is described by the parton model of hadrons, which describes the proton content as quarks and gluons collectively known as partons. In pp scattering events, the factorisation theorem enables the interaction of the protons to be *factorised* into terms describing the long-distance ‘hard-scatter’ interaction between two partons from the incoming protons and terms describing the short-distance distribution of the partons in the incident protons. The energy scale which separates the long-distance and short-distance phenomena is known as the factorisation scale, μ_F , and is introduced to remove low energy divergences from the cross-section calculation.

$$\sigma = \sum_{i,j} \overbrace{\int dx_1 f_i(x_1, \mu^2) \int dx_2 f_j(x_2, \mu^2)}^{\text{blah}} \underbrace{\sigma_{ij}(x_1, x_2, Q^2)}_{\text{blah}} \quad (3.2.1)$$

The incoming partons produce a PV, shown by the red circle and representing the ME calculation. The remaining partons from the incoming protons are also able to interact, producing multi-parton interactions (MPI), resulting in additional, softer particles. These softer interactions represent the UE and are shown by the additional blue partons and the purple oval. From the PV and the ME portion of the simulation, the PS is shown by the red cascade of partons being sequentially emitted. The light green ovals show the hadrons present after the PS and the subsequent green circles show the decay of these hadrons.

Each stage of the event generation procedure will be briefly discussed before summarising the MC simulations used to generate background samples used in the analyses detailed in Chapters 6 and 7. The details of the signal MC samples will be given in the relevant chapters.

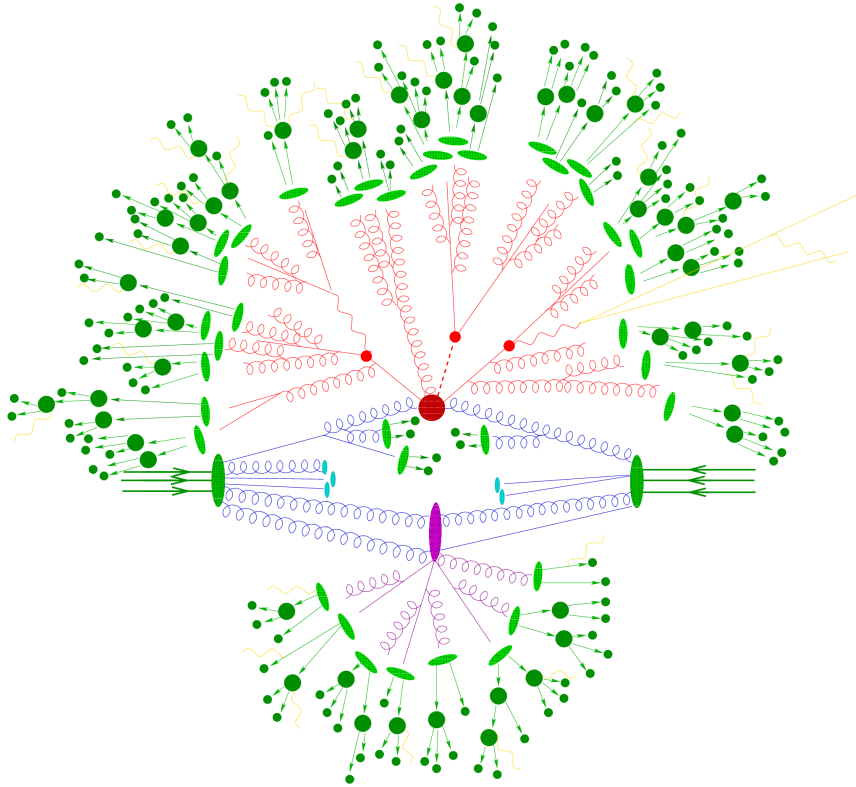


Figure 3.2: A representative diagram showing the MC simulation chain.

847 Hard scatter

848 The hard scatter calculation evaluates the process in which the incoming partons interact
 849 and undergo some transition into different final state particles, and is the highest-energy
 850 process evaluated during event generation. The hard scatter calculation is performed by
 851 evaluating the Feynman diagrams which represent the process of interest to yield the
 852 matrix element (ME). MEs can be calculated at different orders in QCD. LO MEs have
 853 two vertices, and hence the ME goes like $\mathcal{M} \propto g_s^2$, while the cross-section goes like $\sigma \propto$
 854 $|\mathcal{M}^2| \propto g_s^4$. Most processes relevant at the LHC are calculated at NLO, with $\mathcal{M} \propto g_s^3$. As
 an example, representative LO diagrams for $t\bar{t}$ are shown in Figure 3.3. The hard scatter

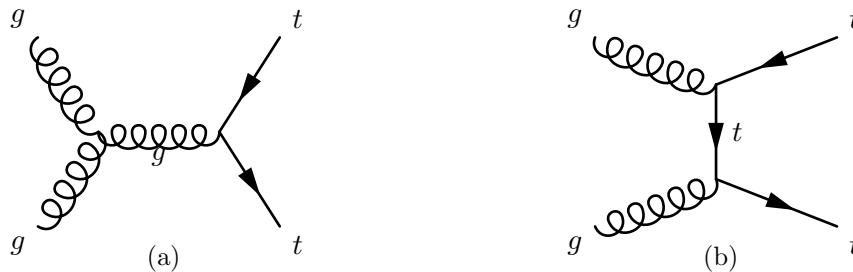


Figure 3.3: This figure shows LO Feynman diagrams for the $t\bar{t}$ process. These diagrams are also relevant for the discussion of $t\bar{t}$ - Wt interference later in this Chapter.

856 calculation often results in unstable particles in the final state. The subsequent stages of
857 the event generation process evolve these hard, unstable particles from the highest energy
858 levels down to softer, stable particles.

859 **Parton distribution functions**

860 Due to the composite nature of protons, the collisions at the LHC are actually interactions
861 of the partons within the proton; qq or gg , for example. Both the valence quarks (uud ,
862 for a proton) and sea quarks (virtual quark-antiquark pairs continually being created and
863 annihilated inside the proton) contribute to the parton-parton collisions. Therefore, to ac-
864 curately predict physical processes, the partons within the proton must be well-modelled,
865 along with the fraction of the total proton momentum that each parton carries, known as
866 the Bjorken x . Parton Distribution Functions (PDFs) predict the probability that a parton
867 of a given type is present inside the proton with a given x , at a squared energy-scale Q^2 .
868 PDF sets are determined through fits to data, namely deep inelastic scattering (DIS) data,
869 with data from ATLAS and CMS being included in the most recent global fits to data. [22]

870

871 PDFs can be calculated to differing orders in QCD, namely leading order (LO), next-to-
872 leading order (NLO) and next-to-next-to-leading order (NNLO). The treatment of quark
873 flavours is also a consideration when evaluating PDFs. The four-flavour scheme (4FS) and
874 five-flavour scheme are the most common treatments of partons for PDFs. In the 4FS,
875 b -quarks are treated as massive partons, unlike the other parton types, and the proton
876 content is limited to gluons and the u , d , c and s quarks. In the 5FS, all partons are
877 treated as massless and the proton can contain gluons and all quarks except the top quark.
878 In both flavour-schemes, the b -quark is included in the final state.

879 **Parton shower, Hadronisation and underlying event**

880 The PS procedure evolves the hard scatter from an energy scale Q^2 down to the hadronisa-
881 tion scale Q_0^2 , typically around the pion mass (~ 200 MeV), through sequential emissions
882 of quarks and gluons, including soft and co-linear emissions. This procedure is repeated
883 until all partons in the event reach the ‘cut-off’ point of the hadronisation scale, at around
884 1 GeV. This procedure takes the event from one with only a few final state particles to a
885 complex final state with many quarks and gluons.

886

887 Considerations must be made when applying a PS algorithm to events with additional
888 partons in the final state, such as MEs calculated at NLO. For example, an event with
889 n -jets in the final state can be produced in two ways; by evolving an event, through soft/-
890 colinear emission, produced at the ME-level with n partons in the final state, or by intro-
891 ducing an additional hard parton emission in the PS procedure to an $n - 1$ parton event.
892 The overlap between these two possibilities is treated using a matching/merging procedure.

893

894 The hadronisation procedure starts after the PS at the cut-off scale of around 1 GeV.
895 This procedure combines the partons present after the PS into colour-neutral states, as
896 required by QCD. There are two widely-used models of hadronisation; the Lund String
897 model [23], and the cluster model [24]. The former treats quark-antiquark pairs as the
898 ends of a string, with a potential energy between the quarks that is proportional to its
899 length such that the $q\bar{q}$ pair are linearly-confined. As the distance between the $q\bar{q}$ pair
900 increases, so too does the potential energy, until it is energetically-favourable for the string
901 to break, forming an additional quark-antiquark pair. The cluster model uses the property
902 of *preconfinement* in QCD, in which the partons in a shower cluster together into colourless
903 groups. These colour-singlets follow an invariant mass distribution which is independent
904 of the hard scatter process. Unstable hadrons are able to decay through allowed SM tran-
905 sitions until all particles in the final state are stable.

906

907 The underlying event refers to all partonic interactions other than the hard scatter. These
908 interactions can arise from the partons from the incoming protons not involved in the hard
909 scatter as well as from any additional partons radiated in the event. Additional jets can
910 arise from the UE, although these are typically much softer than jets produced in the hard
911 scatter.

912 Simulation of SM backgrounds

913 This section details the event generators used for simulating the SM background samples
914 for the analyses described in the subsequent chapters. For the HL-LHC prospects study
915 detailed in Chapter 8, the MC samples used were generated without being passed through
916 the ATLAS detector simulation, but instead a parameterised detector simulation for the
917 HL-LHC ATLAS detector. This is explained in more detail in Chapter 8 and Appendix A.

918 Top processes

919 The POWHEG event generator is used to simulate the hard scatter for both $t\bar{t}$ and single top
920 (t , s and Wt -channels) processes, where the ME is evaluated at NLO accuracy in QCD.
921 The ME generation is interfaced to PYTHIA for parton showering. The analysis detailed
922 in Chapter 6 uses PYTHIA6 for PS, while the analysis detailed in Chapter 7 uses a more
923 recent version, PYTHIA8. The CT10 PDF set is used and the samples are normalised to
924 the next-to-next-to-leading order and next-to-next-to-leading logarithmic (NNLL) cross-
925 sections. Simulating Wt -channel processes at NLO requires additional consideration due
926 to interference with the $t\bar{t}$ process, which will be discussed later in this chapter.

927

928 The $t\bar{t}V$ ($V = W, Z$) and tWZ processes are simulated using the aMC@NLO generator to
929 evaluate the ME at NLO accuracy, while tZ MEs are calculated by MadGraph. All setups

930 are interfaced to PYTHIA8 for PS and use the NNPDF2.3LO PDF set. $t\bar{t}V$ and tWZ back-
 931 grounds are normalised to NLO predictions, while the tZ background is normalised to LO.

932

933 The $t\bar{t}H$ process is also simulated using aMC@NLO for the ME calculation, but is inter-
 934 faced to HERWIG for PS. The CTEQ6L1 PDF set is used and the background is normalised
 935 to the NLO prediction.

936 Vector boson process

937 V +jets ($V = W, Z$) processes are simulated using SHERPA2.2.1 with upto 2 jets at NLO
 938 accuracy and upto 4 jets at LO. The ME calculation is interfaced to the SHERPA PS algo-
 939 rithm. The NNPDFNNLO PDF set is used for generation, with the samples normalised to the
 940 NNLO prediction.

941

942 Diboson processes (VV with $V = W, Z$) are simulated using the SHERPA2.2.1 genera-
 943 tor for the ME calculation, performed at NLO accuracy for upto 1 jet and LO for upto
 944 3 jets. The NNPDFNNLO PDF set is used for the event generation, and the predictions are
 945 normalised to NLO predictions.

946 3.3 Simulating Wt -channel single top at NLO

947 In many search channels, the $t\bar{t}$ and single top backgrounds are among the most prominent
 948 backgrounds due to their relatively high cross-sections and complex, irreducible, multi-
 949 particle final states which can exactly mimic the final states of many New Physics processes.
 950 Making predictions of these SM processes at the highest precision possible therefore enables
 951 searches for New Physics to set the best possible statistical limits, but particular care
 952 must be taken to treat the interference of $t\bar{t}$ and Wt -channel single top correctly. Both the
 953 $t\bar{t}$ and single top backgrounds are simulated at NLO and normalised to NNLO cross-section
 954 calculations. At LO, Wt -channel single top will almost always have a final state containing
 955 WWb , distinct from the $WWbb$ final state in $t\bar{t}$ production, as seen by comparing Figure
 3.3 and 3.4.

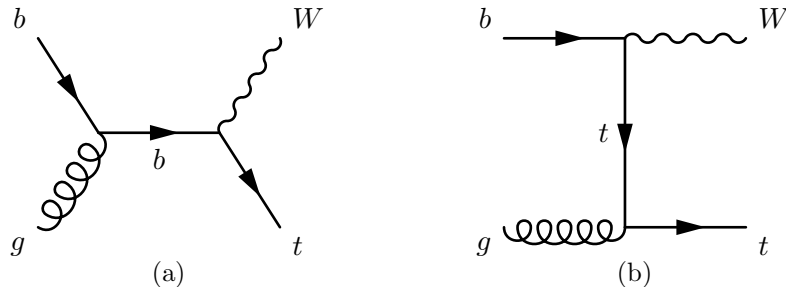


Figure 3.4: Feynman diagrams showing Wt -channel production at LO, where the final state is distinct from the $t\bar{t}$ process.

956

957 However, simulating Wt -channel single top at NLO introduces diagrams which have a
 958 $WWbb$ final state, meaning the $t\bar{t}$ and Wt processes can interfere. NLO diagrams for Wt -
 channel single top are shown in Figure 3.5. When considering the $WWbb$ final state, the

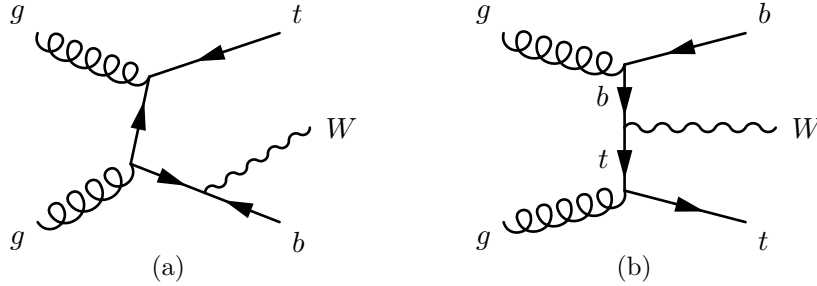


Figure 3.5: Feynman diagrams showing Wt -channel production at NLO. These diagrams interfere with the $t\bar{t}$ process due to their identical final state. The Wt diagrams at NLO can be separated into the number of resonant top quarks present. Figure 3.5b shows a ‘single-resonance’ diagram, while Figure 3.5a shows a ‘double-resonance’ diagram.

959

960 amplitude can be written as the sum of contributions from the $t\bar{t}$ and Wt process. As there
 961 is overlap between the two processes, diagrams with two resonant (on-shell) top quarks,
 962 known as ‘double-resonance’ diagrams are attributed to the $t\bar{t}$ process, while diagrams with
 963 a single resonant (on-shell) top quark are referred to as ‘single-resonance’ diagrams and
 964 are attributed to Wt production. The amplitude can be written as:

$$\mathcal{A}_{WWbb} = \mathcal{A}_{DR} + \mathcal{A}_{SR} \quad (3.3.1)$$

965 where DR and SR correspond to the double-resonant and single-resonant components,
 966 respectively. The production goes with the square of the amplitude, which is where the
 967 interference terms arise:

$$|\mathcal{A}_{WWbb}|^2 = |\mathcal{A}_{1R}|^2 + |\mathcal{A}_{2R}|^2 + 2\mathcal{R}e(\mathcal{A}_{1R}^* \mathcal{A}_{2R}) \quad (3.3.2)$$

968 The first term on the right side is the contribution from double-resonance diagrams, the
 969 second term from single-resonance diagrams and the last term from interference between
 970 the two sets of diagrams. All top-pair MC samples used in this Thesis are generated using
 971 only the diagrams which contribute to \mathcal{A}_{2R} , having exactly two resonant top quarks. The
 972 nominal choice for modelling the single top Wt -channel process uses only the diagrams
 973 which contribute to \mathcal{A}_{1R} , neglecting diagrams with two resonant top quarks and hence
 974 removing any interference from the cross-section. However, it is important to assess the
 975 size and impact of the interference, especially in the extreme regions of phase space often
 976 covered by searches for New Physics, as the interference becomes important in regions
 977 where $m_{Wb} \sim m_t$. Two schemes for assessing the impact of the $t\bar{t}$ - Wt interference are

978 used in this Thesis and will be discussed in the following subsections.

979 **Diagram removal vs. diagram subtraction**

980 As previously mentioned, the nominal method of simulating the Wt -channel single top
 981 process is to remove all diagrams with two resonant top quarks; this method is known
 982 as the *diagram removal* (DR) scheme [25]. An alternate scheme of generation, known as
 983 *diagram subtraction* (DS) [25] is defined such that single- and double-resonance diagrams
 984 are included, and the contribution from the double resonance diagrams is subtracted at
 985 the cross-section level as follows:

$$d\sigma^{DS} = d\sigma^{WWbb} - d\sigma^{subt} \quad (3.3.3)$$

986 In Equation 3.3.3, the first term on the right is proportional to Equation 3.3.2. In the
 987 analysis detailed in Chapter 6, the differences between the DR and DS schemes for gen-
 988 erating the Wt process were found to $\mathcal{O}(100\%)$ in *all* analysis regions due to poor MC
 989 statistics in the DS sample. The difference in the DR and DS prediction in the single top
 CR of this analysis (described in Table 3.3) is shown in Table 3.2. As seen in Table 3.2, the

Process	MC prediction
$t\bar{t}$	17.72 ± 1.85
Single top (DR)	28.54 ± 1.72
Single top (DS)	6.61 ± 1.9
W +jets	5.80 ± 1.32
$t\bar{t}V$	3.14 ± 0.27
Diboson	0.84 ± 0.26
Small backgrounds	0.10 ± 0.05
Total MC (DR)	56.1 ± 2.9
Total MC (DS)	34.2 ± 3.0
Data	64

Table 3.2: A table showing the estimated yields from MC of SM processes in CRST. The data-MC discrepancy is much larger with the DS Wt prediction and the region becomes dominated by top-pair production.

990

991 DR and DS schemes make drastically different predictions for the single top yield in this
 992 region. In the case of the DS prediction, the single top purity in this region is no longer
 993 dominant, becoming subdominant to top-pair production. The data-MC difference of the
 994 two predictions can be seen in Figure 3.6, showing the E_T^{miss} distributions in CRST with
 995 both the DR and DS Wt samples.

996 Due to the large differences in the DR and DS predictions observed, an alternate scheme
 997 for estimating the interference uncertainty was used, and is detailed in the next section.

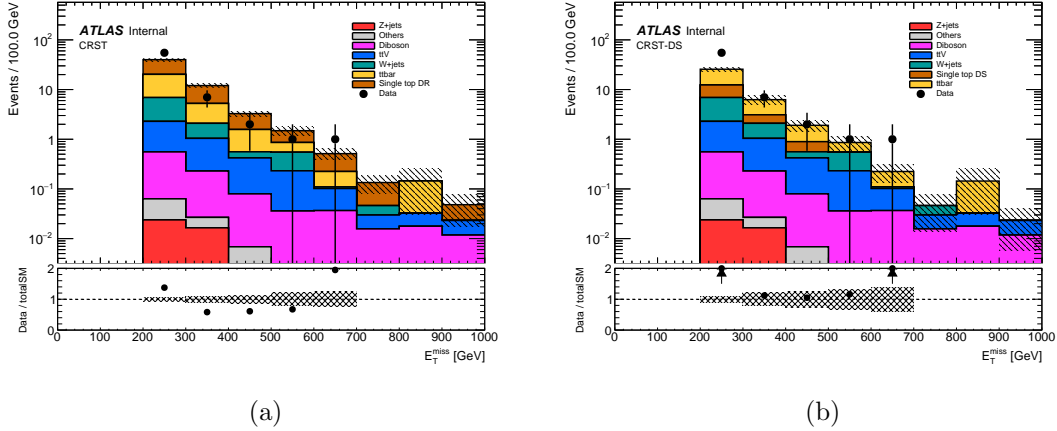


Figure 3.6: Plots showing the E_T^{miss} distribution in the single top CR of the analysis detailed in Chapter ???. Figure 3.6a shows the data-MC comparison using the DR single top sample, while Figure 3.6b shows the same comparison using the DS single top sample.

998 In the analysis detailed in Chapter 7, studies were performed to find a kinematic region to
 999 use as a CR for the Wt background, a relatively minor but irreducible background to the
 1000 signal. Using a similar method to those used to optimise the signal selection, as described
 1001 in Section 5.3, a region where the single top background was dominant was found using
 1002 a combination of an adapted random grid search and a genetic algorithm. The kinematic
 selections for this region are summarised in Table 3.3.

Variable	Selection
am_{T2}	> 220 GeV
m_W^{had}	< 60 GeV
m_T	$\in [40, 100]$ GeV
p_T^{b2}	> 50
$\Delta\phi(\ell, E_T^{miss})$	< 0.5

Table 3.3: This table shows the selections used, in addition to the preselection cuts listed in Table 7.2, for the single top CR study for the analysis detailed in Chapter 7.

1003
 1004 The estimated yields and purity obtained using these selections are given in Table 3.4.
 1005 The distributions of the subleading b -jet p_T and $\Delta\phi(\ell, E_T^{miss})$, used to define and isolate
 1006 the Wt background, is shown in Figure 3.7 for both the DR and DS schemes.
 1007 Due to the extreme differences in predictions between the DR and DS schemes, and the
 1008 relatively small contribution of Wt in the SR, this CR was not used in the final analysis,
 1009 detailed in Chapter 7.

Process	MC prediction
$t\bar{t}$	135.52 ± 1.87
Single top (DR)	253.39 ± 8.04
Single top (DS)	39.08 ± 3.2
W +jets	134.75 ± 4.35
$t\bar{t}V$	3.41 ± 0.25
Z +jets	0.83 ± 0.14
Diboson	7.66 ± 0.85
ttH	1.37 ± 0.1
tWZ	0.02 ± 0.03
Purity (DR)	47.2%
Purity (DS)	12.1%
Data	363

Table 3.4: This table shows the predicted background yields for all SM backgrounds considered, along with the purity of single top for both the DR and DS schemes, and finally the observed data in this region. As can be seen there is a huge discrepancy between the two Wt generation schemes, with the data being enveloped by the two predictions.

1010 Coherent simulation of $WWbb$ final state

1011 An alternative to the comparison of the DR and DS schemes was also used in the analy-
1012 sis detailed in Chapter 6. This approach uses three sets of complementary MC samples,
1013 ‘singleres’, ‘doubleres’ and ‘sum’, to simulate the $WWbb$ final state, generated at LO and
1014 at truth-level. The ‘singleres’ samples include diagrams with exactly one resonant top
1015 quark, corresponding to \mathcal{A}_{1R} , the ‘doubleres’ samples include diagrams with two resonant
1016 top quarks, corresponding to \mathcal{A}_{2R} and the ‘sum’ samples include all diagrams with at least
1017 one resonant top quark, corresponding to \mathcal{A}_{WWbb} . As these samples are generated at LO,
1018 these samples are used only as a comparison between themselves, and not the nominal DR
1019 prediction, generated at NLO. Figure 3.8 shows comparisons of the shape and normalisa-
1020 tion of the m_T and m_{CT} distributions for the three samples at preselection level and in
1021 the single top CR.

1022 Using the three sets of samples, it is possible to directly estimate the impact of the inter-
1023 ference, by comparing the MC prediction for the Wt process with and without interference
1024 effects. The estimated yield for the Wt process with the interference effects, N_{MC}^{Wt+int} , is
1025 given by:

$$N_{MC}^{Wt+int} = N_{MC}^{sum} - N_{MC}^{doubleres} \quad (3.3.4)$$

1026 This estimated yield can be directly compared with the prediction for the Wt process,
1027 N_{MC}^{Wt} . Table 3.5 shows a comparison of the nominal Wt DR prediction compared with the
1028 DS prediction, along with the predictions for the dedicated $WWbb$ samples, and finally

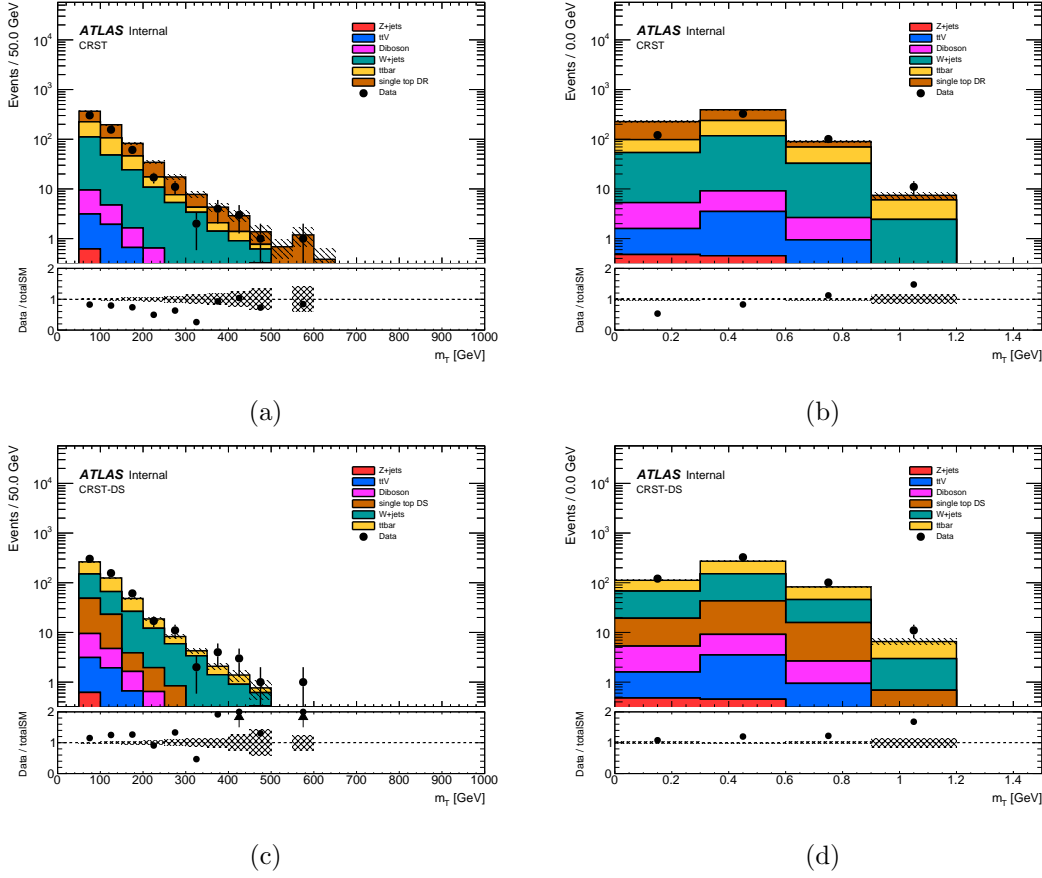


Figure 3.7: This figure compares the two key variables used to isolate the Wt background for the DR and DS schemes. Large differences are observed between the DR and DS schemes, with the observed data being enveloped by the two.

1029 showing the predicted Wt yield including interference effects, calculated using Equation 3.3.4. It is

Region	TRLM	TRMM	TRHM	STCR
Single top (DR)	22.81 ± 3.12	19.67 ± 1.51	53.11 ± 2.51	28.54 ± 1.72
Single top (DS)	12.25 ± 2.17	13.22 ± 2.16	28.43 ± 2.97	6.61 ± 1.9
WWbb singleres	6.68 ± 0.05	8.62 ± 0.06	21.38 ± 0.1	23.44 ± 0.11
WWbb doubleres	23.28 ± 0.38	80.73 ± 0.48	598.7 ± 1.29	22.26 ± 0.3
WWbb sum	25.37 ± 0.4	84.94 ± 0.5	610.37 ± 1.34	29.97 ± 0.34
WWbb singleres + interference	2.09 ± 0.55	4.21 ± 0.69	11.67 ± 1.86	7.71 ± 0.45

Table 3.5: This table shows a comparison of the nominal DR Wt prediction with the DS prediction, and the predictions of the three sets of $WWbb$ samples. The value quoted for the $WWbb$ singleres + interference prediction is calculated using Equation 3.3.4. The DR and DS predictions both use samples reconstructed with the full ATLAS detector simulation, while the $WWbb$ samples are generated at truth-level.

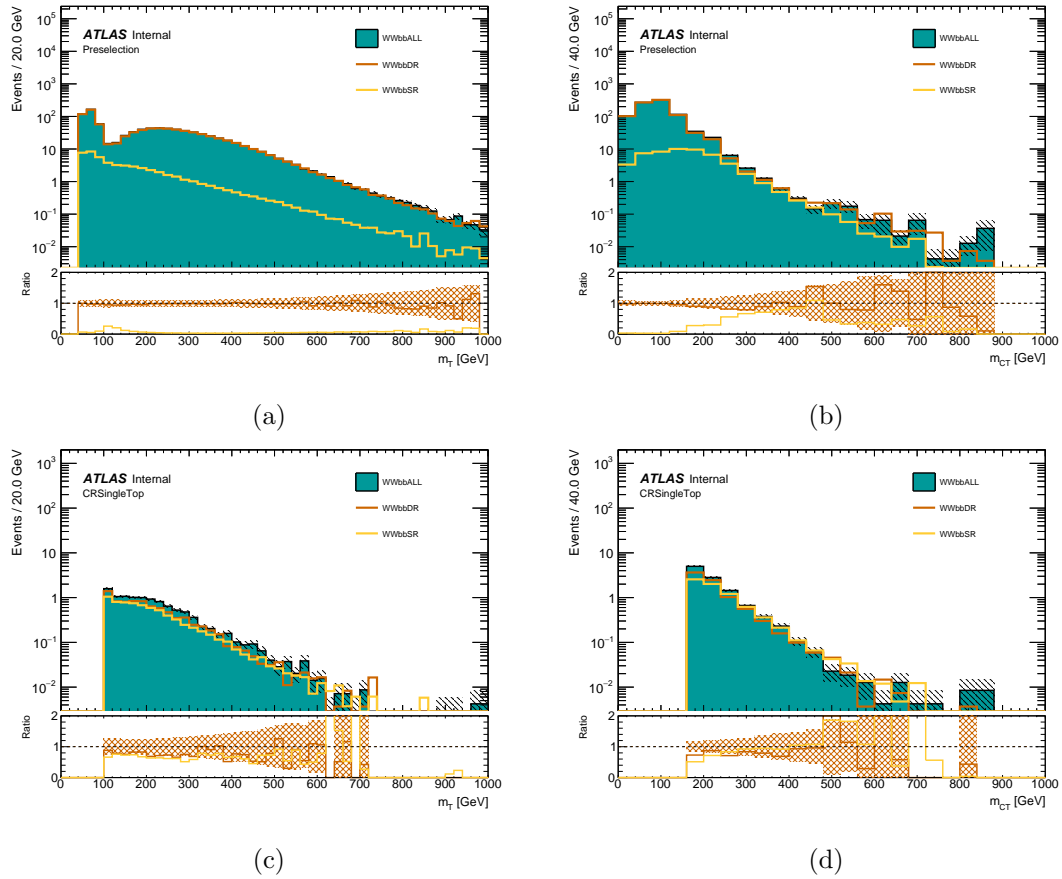


Figure 3.8: This figure shows the difference in shape and normalisation of for the $WWbb$ singleres, doubleres and sum samples. The ratio in the bottom panel shows the ratio of the singleres and doubleres to the sum, while the hatched error bar shows the sum in quadrature of the MC statistical uncertainty of the sum and doubleres sample. This error is equivalent to the statistical uncertainty on the estimate of the Wt singleres + interference.

1031 The uncertainties derived using these samples are detailed in Section ??.

Chapter 4

Object reconstruction

Particles produced in the pp collisions inside ATLAS can interact with the detector subsystems, as described in Chapter 2, with each type of particle leaving a unique signature. The combination of the tracking and calorimetry information enables the reconstruction of the underlying physics of an event. When combining this information, particles are referred to as physics ‘objects’, with the objects of interest to this Thesis being leptons, jets and E_T^{miss} . This Chapter begins by giving an overview of the different signatures of each particle type, before summarising the reconstruction techniques for each object.

4.1 Reconstruction overview

The interaction of particles with the detector subsystems is determined by several factors. Firstly, charged particles create small electrical signals when passing through the tracking layers of the detector due to ionisation effects, whereas neutral particles pass through the tracking layers without leaving a signature. Secondly, the particle type will determine the type of particle shower that occurs when entering the calorimeters, with electrons and photons depositing almost all of their energy in the ECAL, and particles which interact via the strong interaction depositing energy in the HCAL. Finally, the presence of particles which do not interact with the detector subsystems, namely neutrinos and any massive, weakly-interacting new particles produced in the event, can be inferred from the total transverse momentum imbalance of the system, the E_T^{miss} . This is defined as the magnitude of the negative vector sum of all of the visible particles measured by ATLAS in an event. Figure 4.1 shows a representative diagram of the signatures of various particle types which are reconstructed within ATLAS.

By introducing loose requirements on the combination of the tracking and calorimetry information, ‘baseline’ objects are defined, placing requirements on the p_T , η and isolation of the object. Particle signatures in the same region of the detector can be reconstructed into multiple objects simultaneously, and thus to circumvent double counting a procedure

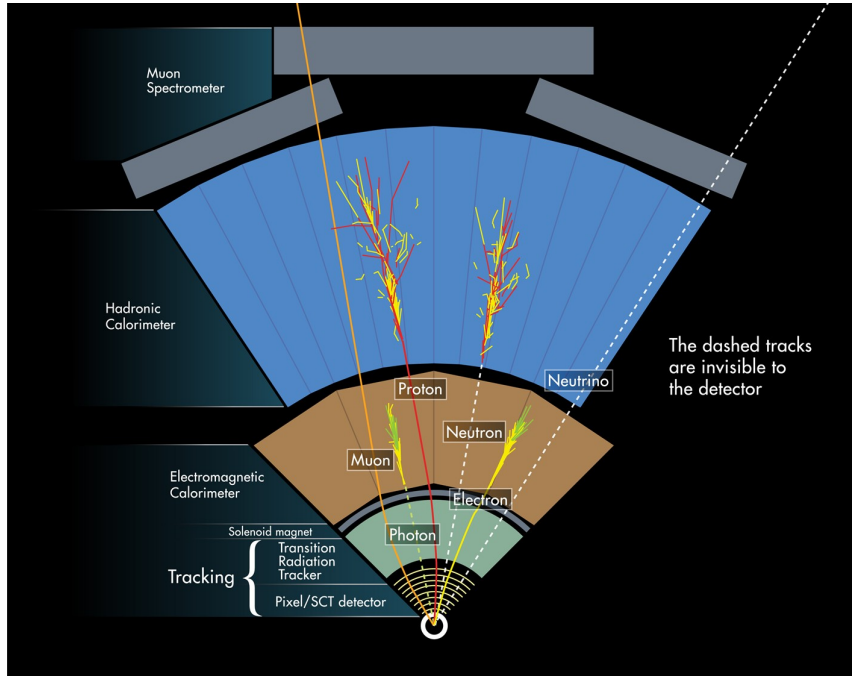


Figure 4.1: This diagram shows the various signatures left by different particles in the ATLAS detector. Solid lines represent a signature left in the corresponding detector subsystem, while dashed lines show the particle did not interact with that detector subsystem. [26]

1060 is defined to remove overlap between objects, described later in this Chapter. Finally, a
 1061 tighter set of requirements is placed upon the objects on a per-analysis basis, known as
 1062 ‘signal’ requirements, which define the objects ultimately used in a specific analysis.

1063 4.2 Leptons

1064 The signals of interest in the analyses detailed in Chapters 6 and 7 have a single, charged
 1065 lepton in the final state, which is required to be either an electron or muon. In both cases,
 1066 this lepton originates from the decay of a W boson to $\ell\nu$. This Section will describe the
 1067 reconstruction of electrons and muons, as well as briefly discussing the reconstruction of
 1068 photons and tau leptons.

1069 Electrons and photons

1070 The reconstruction of electrons and photons use information from the ID and ECAL. While
 1071 electrons interact with both subsystems, photons leave no hits in the ID, with their only
 1072 signature being an EM shower in the ECAL. However, photons can undergo a conversion to
 1073 an electron-positron pair when they interact with detector material, and hence the recon-
 1074 struction of electrons and photons proceeds in the same way. Both electrons and photons
 1075 are reconstructed within the range $|\eta| < 2.47$, such that full tracking coverage from the

1076 pixel detector and SCT are available [27,28]. For the first step of electron/ γ reconstruction,
 1077 the ECAL is segmented into a 200×256 grid in η, ϕ . The energy deposited by an electron
 1078 or photon at a given η, ϕ grid point is evaluated by summing the energy deposits in all
 1079 layers of the ECAL, forming a ‘tower’. A sliding-window of size 3×5 towers is scanned
 1080 over the η, ϕ grid; any point of the grid where the summed E_T of all towers within the
 1081 window exceeds 2.5 GeV is used as a seed for the clustering step. In order to identify the
 1082 ECAL cluster as an electron or photon, the seed clusters are loosely matched to tracks in
 1083 the ID. Tracks are extrapolated from the ID to the middle layer of the ECAL, with any
 1084 track satisfying $\Delta\eta < 0.05$ and $-0.10 < \Delta\phi < 0.05$ considered as matched to the seed
 1085 cluster. Seed clusters with at least one matched track are electron candidates while seed
 1086 clusters with 0 matched tracks are photon candidates. Finally, the reconstructed energy of
 1087 the candidate is determined by extending the window around the seed cluster to a size of
 1088 3×7 towers for $|\eta| < 1.37$ and 5×5 for $1.52 < |\eta| < 2.47$ and summing the energy deposits
 1089 within the extended window.

1090

1091 Identification algorithms are applied to electron and photon candidates in order to quan-
 1092 tify the quality of reconstruction and evaluate any potential misidentification. Photons
 1093 radiated by electrons through Bremsstrahlung can produce electron-positron pairs, which
 1094 subsequently interact with the detector material, providing a background to the prompt
 1095 electron from the PV. Electron identification is performed in the region $|\eta| < 2.47$ using
 1096 a likelihood discriminant, which takes as inputs tracking and calorimetry information, as
 1097 well as quantities constructed from a combination of both tracking and calorimetry in-
 1098 formation. Photon identification is performed using selections on calorimeter quantities,
 1099 such as quantities related to the shape of the EM shower in the ECAL, as described in [28].

1100

1101 In order to be applicable to a range of analyses, each with various electron selection ef-
 1102 ficiency and background rejection requirements, three working points are defined. The
 1103 working points, Loose, Medium and Tight, have efficiencies of 93%, 88% and 80% for a
 1104 prompt electron with $E_T = 40$ GeV, respectively. The efficiencies of the three working
 1105 points is shown as a function of electron E_T and η in Figure 4.2.

1106

1107 A characteristic signature of the prompt production of electrons is that there is rela-
 1108 tively little activity surrounding the particle when compared to the semileptonic decay of
 1109 heavy-flavour quarks, from misidentification or from photon conversion. The *isolation* of
 1110 an electron can be exploited as a tool for rejecting such backgrounds. Two sets of isolation
 1111 variables are defined, track-based and calorimeter-based, to evaluate how much activity
 1112 surrounds an electron. Nine electron isolation working points are defined, to enable a bal-
 1113 ance of signal electron efficiency and background rejection to be achieved by analyses [27].

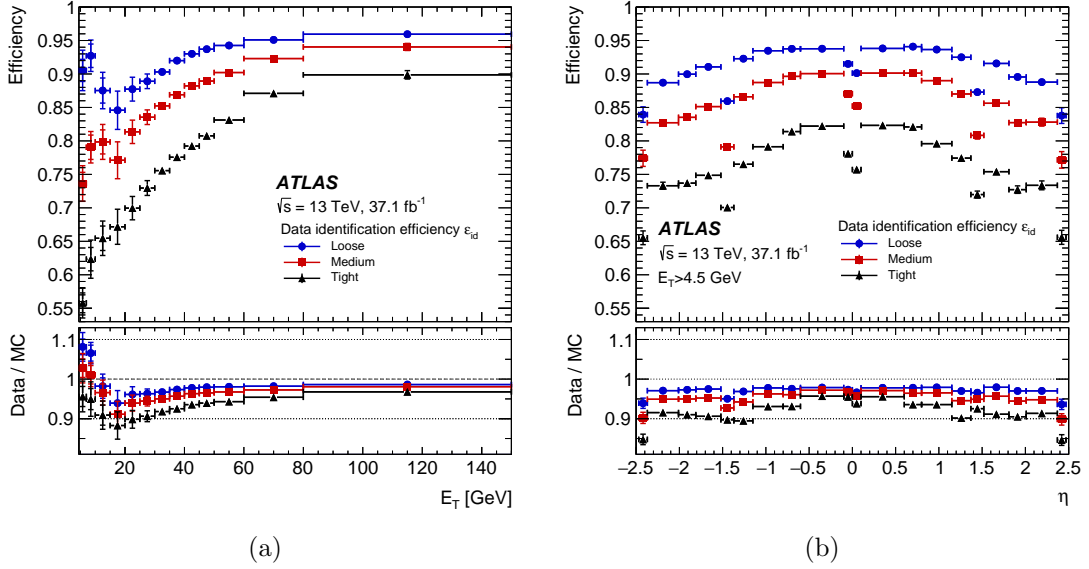


Figure 4.2: Plots showing the electron identification efficiencies for the Loose, Medium and Tight working points, measured in $Z \rightarrow ee$ events [27], as a function of electron p_T (4.2a) and η (4.2b).

1114 Muons

1115 Muons are identified using inputs from the ID and MS, with additional information being
 1116 provided by the calorimeters. The ID provides tracking information in the range $|\eta| < 2.5$,
 1117 while the MS provides tracking information in the range $|\eta| < 2.7$. Muon reconstruction
 1118 proceeds independently in the ID and MS; in the ID, tracks are built using information
 1119 from the IBL, Pixel detector, SCT and TRT, in the same way as for all charged parti-
 1120 cles. Muon reconstruction in the MS proceeds by first searching for hit patterns in the
 1121 individual MS cells, known as segments, and then fitting segments together from different
 1122 layers to form track candidates. There are four types of reconstructed muon in ATLAS;
 1123 *Combined (CB)*, *Segment-tagged (ST)*, *Calorimeter-tagged (CT)* and *Extrapolated (ME)*
 1124 muons. Combined muons use hits in both the ID and MS detectors to build muon tracks,
 1125 typically taking an ‘outside-in’ approach by starting reconstruction in the MS and match-
 1126 ing the track candidate to a track in the ID.

1127

1128 Similarly to electrons, working points are defined for muon identification, enabling analyses
 1129 to find an optimum balance of muon selection efficiency and background rejection. There
 1130 are four muon ID working points defined; Loose, Medium, Tight and High- p_T , determining
 1131 the quality of a muon reconstruction based upon the q/p significance and ρ' as well as the
 1132 normalised χ^2 of the combined track fit. The q/p significance is defined as the absolute
 1133 value of the difference between the measured charge-to-momentum ratio in the ID and MS,
 1134 divided by the quadratic sum of the uncertainties on the measurements, while ρ' is defined

1135 as the absolute value of the difference in the measured p_T in the ID and MS, divided by the
 1136 p_T of the combined track [29]. The muon reconstruction efficiency as a function of the η is
 shown in Figure 4.3 for each of the muon identification working points. Muons originating

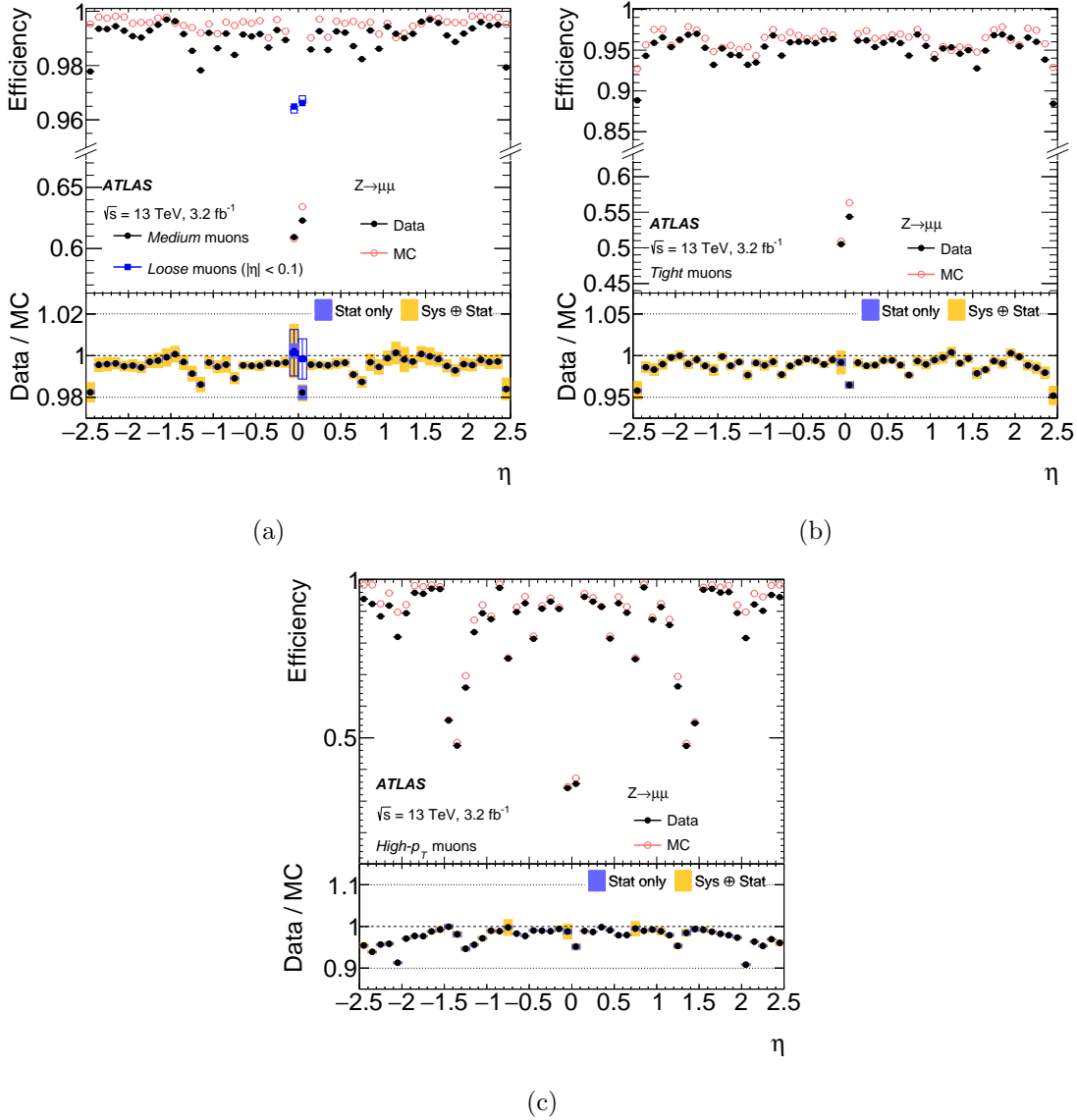


Figure 4.3: Plots showing the muon reconstruction efficiencies for the Loose and Medium (4.3a), Tight (4.3b) and High- p_T (4.3c) working points. All efficiencies are measured in $Z \rightarrow \mu\mu$ events.

1137 from heavy particles such as the W boson are often well separated from any surrounding
 1138 particles. Requiring that there is no surrounding activity from a muon, known as the
 1139 isolation criteria, can be extremely useful for rejecting backgrounds such as QCD. Two
 1140 muon isolation variables, one track-based and one calorimeter-based, are used to evaluate
 1141 if a muon is isolated. The distributions of the track- and calorimeter-based isolation vari-
 1142 ables can be seen in Figure 4.4. Seven muon isolation working points are defined to enable
 1143

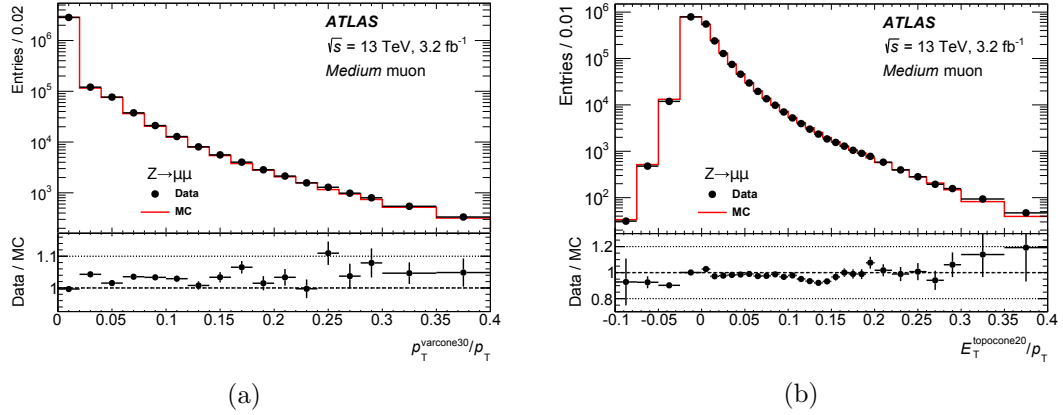


Figure 4.4: Plots showing the distribution of the muon track-based (4.4a) and calorimeter-based (4.4b) for muons identified in $Z \rightarrow \mu\mu$ events with the Medium working point.

1144 analyses to select an appropriate level of isolation for the signal under investigation. The
 1145 explicit definitions of the muon isolation working points is given in [29].

1146 **Taus**

1147 Taus, the heaviest of the charged leptons, can decay either leptonically ($\tau \rightarrow \ell \nu_\ell \nu_\tau$,
 1148 $\ell = e, \mu$) or hadronically ($\tau \rightarrow \text{hadrons } \nu_\tau$). The case with a leptonically-decaying tau,
 1149 denoted by τ_{lep} , is simply reconstructed as either an electron or muon, with the neutrinos
 1150 contributing to the real component of the E_T^{miss} . However, there is a dedicated reconstruc-
 1151 tion and identification flow for hadronically-decaying taus, denoted by τ_{had} . τ_{had} candidates
 1152 are seeded from jets (the reconstruction of which is detailed later in this Chapter), which
 1153 proceeds by matching tracks with $p_T > 1$ GeV which lie within $\Delta R < 0.2$ of a seed jet to a
 1154 collision vertex. Tau identification is then performed using a BDT, trained to reject QCD
 1155 backgrounds, using tracking information and the calorimeter clustering information used
 1156 to reconstruct jets.

1157

1158 **4.3 Jets**

1159 When proton bunches cross inside ATLAS, the environment is extremely dense with quarks
 1160 and gluons. Strong interactions between partons in the incoming bunches of protons can
 1161 result in the ejection of quarks and gluons in the transverse plane. The outgoing quarks
 1162 and gluons evolve through a sequence of hadronisation, gluon splittings and radiations, as
 1163 described in Section ?? into a complex, highly-collimated collection of particles known as
 1164 *jets*. The parton-dense environment of each bunch-crossing means pp collision events usu-
 1165 ally have numerous jets which can be from the hard scatter event, the proton remnants, or
 1166 from pileup events. Jets provide an experimental tool for studying the strong interactions

1167 of the hard scatter, and are extremely important in the analyses presented in Chapters
 1168 6 and 7, with both signal processes containing jets originating from the presence of b -quarks.

1169

1170 For the analyses detailed in Chapters 6 and 7, jet reconstruction begins by first clustering
 1171 calorimeter cells which are topologically-connected in 3-dimensions, known as ‘topoclus-
 1172 ters’ [30]. The requirement of cells being topologically-connected helps minimise the
 1173 misidentification of jets due to electronic noise and pileup, and makes use of the high-
 1174 granularity of the ATLAS calorimeters. Each calorimeter cell is expected to have a baseline
 1175 level of noise, σ_{noise} , which is defined as:

$$\sigma_{\text{noise}} = \sqrt{(\sigma_{\text{noise}}^{\text{electronic}})^2 + (\sigma_{\text{noise}}^{\text{pileup}})^2} \quad (4.3.1)$$

1176 The first step in reconstructing jets using topoclusters proceeds by finding calorimeter
 1177 cells where the energy deposit is $E_{\text{cell}} > 4\sigma_{\text{noise}}$. All cells with $E_{\text{cell}} > 4\sigma_{\text{noise}}$ form the
 1178 seed for ‘proto-clusters’, the seed for the following steps of the algorithm. The clustering
 1179 algorithm then proceeds by finding all cells neighbouring a seed which satisfy $E_{\text{cell}} > 2\sigma_{\text{noise}}$.
 1180 Finally, the clustering algorithm stops when no neighbouring cells satisfies $E_{\text{cell}} > 2\sigma_{\text{noise}}$
 1181 but satisfy $E_{\text{cell}} > 0$. In the context of this clustering algorithm, ‘neighbouring cells’ can
 1182 be either adjacent cells in the same layer of the calorimeter, or cells in different calorime-
 1183 ter layers which have some overlap in η, ϕ space. Any protocluster containing more than
 1184 one local maxima, a cell which has a greater energy deposition than its surrounding cells,
 1185 are separated around their respective maxima so as not to bias the jet clustering algorithm.

1186

1187 All topoclusters are calibrated to an appropriate energy scale, either hadronic or EM,
 1188 to account for the energy losses in reconstruction. The ATLAS calorimeters are non-
 1189 compensating, meaning that an incoming electron, e , and hadron, h , both of energy E ,
 1190 will have a ratio of measured energy $E_e/E_h > 1$. A fraction of the energy of hadronic
 1191 showers goes unmeasured as it is absorbed in the binding energy of nucleons which are
 1192 released as the shower evolves in the HCAL [31]. To account for this, corrections are ap-
 1193 plied to signals identified as coming from a hadronic source. Corrections are also applied
 1194 to estimate the true energy lost due to the noise-suppression requirements used for forming
 1195 proto-clusters, as well as corrections for energy loss in any inactive detector material in
 1196 the region near to the cluster.

1197 Jet clustering algorithms

1198 Jet reconstruction proceeds by clustering together the topoclusters described in the previ-
 1199 ous Section into jets which are determined to have originated from the same parton. Jet
 1200 clustering algorithms can be separated into cone algorithms and sequential algorithms.

1201 **Cone algorithms** The first jet clustering algorithm was developed in the 1970's and
 1202 used in $e^+e^- \rightarrow q\bar{q} \rightarrow 2j$ events. Events were identified as containing two jets if at least
 1203 $1-\epsilon$ of the event's total energy was contained in two cones with opening half-angle δ . The
 1204 choice of the parameters ϵ and δ is almost entirely arbitrary, and hence the algorithm can
 1205 reconstruct vastly different final state jets and multiplicities depending entirely upon the
 1206 parameter choice. In addition, in pp collisions the concept of total energy is obfuscated
 1207 by the fact that the interacting protons contain partons with only a fraction of the total
 1208 proton energy, with the residual energy either forming the underlying event or escaping
 1209 down the beam pipe.

1210

1211 Most cone algorithms reconstruct jets through an iterative procedure, hence being known
 1212 as iterative cones (IC). These algorithms proceed by first selecting a seed particle, i , and
 1213 summing the momenta of all particles, j , satisfying the below condition:

$$\Delta R_{ij} = \sqrt{(y_i - y_j)^2 + (\phi_i - \phi_j)^2} < R. \quad (4.3.2)$$

1214 In the equation above, R represents the jet radius, which is the modern-day equivalent of
 1215 the δ parameter discussed earlier. This process is repeated, each time taking the result
 1216 of the previous iteration as the new seed, until the resulting jet cone is stable. This class
 1217 of algorithms are not fully specified without specifying a definition for seed particles, and
 1218 without defining a procedure for removing overlap between cones. Cone algorithms are also
 1219 plagued by infrared and collinear (IRC) unsafety. An infrared-safe jet clustering algorithm
 1220 will reconstruct the same set of final state jets regardless of additional soft emissions in an
 1221 event, while a collinear-safe jet clustering algorithm will reconstruct the same set of final
 1222 state jets if a parton of energy E is replaced by two collinear partons whose summed energy
 1223 is equal to E . Most IC jet clustering algorithms use the hardest particle in an event as the
 1224 seed which can violate collinear safety if the hardest particle in the event is replaced by
 1225 two collinear particles. In this case, the hardest particle in the event may change, meaning
 1226 the reconstructed final state jets may also change.

1227 **Sequential algorithms** Sequential jet clustering algorithms work in a similar, iterative
 1228 manner as for IC algorithms, except using a 'bottom-up' approach to the clustering. The
 1229 first use of a sequential clustering algorithm was also in the context of electron-positron col-
 1230 lisions. There are three widely-used sequential clustering algorithms today; the inclusive- k_t
 1231 algorithm, the Cambridge/Aachen algorithm and the anti- k_t algorithm. All three of these
 1232 algorithms can be specified by the following equations.

$$d_{ij} = \min \left(p_{T,i}^{2p}, p_{T,j}^{2p} \right) \frac{\Delta R_{ij}^2}{R^2} \quad (4.3.3)$$

1233

$$\Delta R_{ij}^2 = (y_i - y_j)^2 + (\phi_i - \phi_j)^2 \quad (4.3.4)$$

1234

$$d_{iB} = p_{T,i}^{2p} \quad (4.3.5)$$

1235 In Equation 4.3.3 and 4.3.5, $p_{T,i}^{2p}$ and $p_{T,j}^{2p}$ represent the transverse momentum of the i th
 1236 and j th particle, respectively, raised to the power $2p$, where p is determined by the clus-
 1237 tering algorithm being used. In the inclusive- k_t algorithm, the value of p is set to $+1$. This
 1238 algorithm proceeds by iterating over all particles j within a radius R of i , calculating all
 1239 d_{ij} and d_{iB} and finding the minimum. If $d_{ij} < d_{iB}$, the two particles are combined into a
 1240 new particle and the algorithm proceeds from the start. If $d_{ij} > d_{iB}$, the particle i is deter-
 1241 mined to be a final-state jet and is removed from the list of particles, before the algorithm
 1242 restarts from the beginning. Due to the construction of d_{ij} in the inclusive- k_t algorithm,
 1243 an arbitrary number of particles can become final state jets, leading to extremely complex
 1244 events. The anti- k_t algorithm follows the same procedure as for the inclusive- k_t algorithm,
 1245 but provides resolution to this issue by setting $p = -1$ in Equation 4.3.5. Therefore, in
 1246 the anti- k_t algorithm, jet clustering proceeds from hard seeds, and sequentially adds softer
 1247 particles until the jet is stable and is classified as a final-state jet. In this thesis, the anti- k_t
 1248 algorithm is used to clustering all jets, with the jet radius parameter R set equal to 0.4 in
 1249 all analyses detailed in the subsequent Chapters.

1250

1251 Once jets are clustered, they must be calibrated to account for detector performance and
 1252 resolution effects. The jet energy scale (JES) calibration is applied to account for the non-
 1253 compensating behaviour of the ATLAS hadronic calorimeters, as described in Chapter 2.
 1254 The JES calibration depends upon the jet p_T and η , as well as the pileup conditions and the
 1255 flavour composition of the jet. These calibrations are derived by comparing data and MC
 1256 samples in dijet, Z +jets and γ +jets p_T balance measurements. Jets arising from pileup
 1257 events are suppressed using the Jet Vertex Tagger (JVT) discriminant [32]. The JVT uses
 1258 information of the fraction of the transverse momentum of a given jet to originate from the
 1259 PV to give a likelihood that a given jet is from the hard scatter event. By default, analyses
 1260 require that the JVT value is > 0.59 , with jets scoring less than this being rejected.

1261 4.4 Flavour-tagging

1262 For both measurements of SM processes and searches for BSM physics, identifying jets
 1263 originating from heavy flavour (c, b) quarks is extremely important. b -quarks produced
 1264 in the hard scatter hadronise and then travel a significant distance before decaying. The
 1265 lifetime of b -hadrons is relatively long at around $1.5ps$ because of suppression in the CKM
 1266 elements for V_{ub} and V_{cb} , meaning a b -hadron can travel several millimetres before decay-
 1267 ing. The result of this is the presence of a second decay vertex distinct from the PV, with

1268 tracks which have large impact parameters. The impact parameters of a track, d_0 and
 1269 z_0 , represent the transverse and longitudinal distance of closest approach to the PV, re-
 1270 spectively. This distinctive signature enables jets originating from a b -quark to be ‘tagged’.

1271

1272 The MV2c10 b -tagging algorithm is used to flavour-tag all b -jets in the analyses detailed
 1273 in this Thesis. This algorithm utilises a Boosted Decision Tree (BDT) classifier which has
 1274 21 input variables, such as the jet p_T and η as described in [33]. The MV2c10 algorithm
 1275 aims to distinguish b -jets from jets originating from a charm quark, named c -jets, jets
 1276 originating from hadronic tau decays, named τ -jets and all other jets, originating from
 1277 light-flavour quarks (u , d , s) and gluons, named ‘light-jets’. The output of the MV2c10
 1278 BDT is shown in Figure 4.5, applied to a simulated set of $t\bar{t}$ events with dileptonic final
 states. The output of the MV2c10 algorithm, as shown in Figure 4.5 applied to a simulated

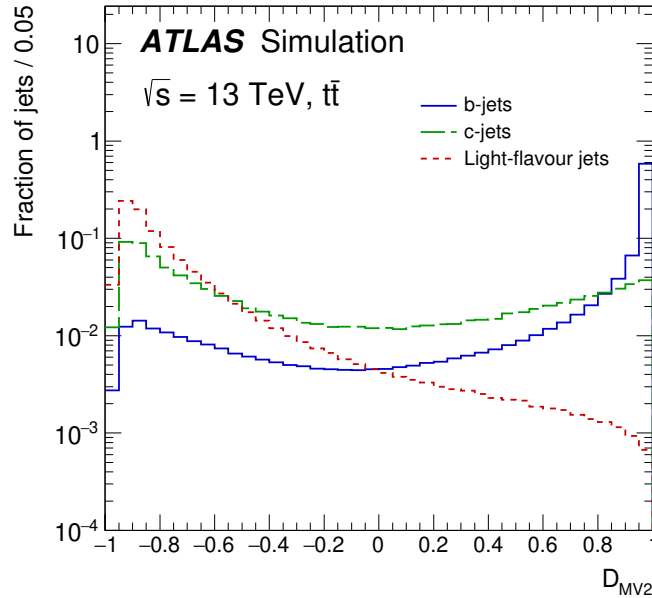


Figure 4.5: Figure showing the output of the BDT used by the MV2c10 algorithm to tag jets originating from b -quarks, using simulated $t\bar{t}$ events.

1279

1280 sample of dileptonic $t\bar{t}$ events, shows that the discriminant, D_{MV2} , peaks at values $\rightarrow 1$ for
 1281 b -tagged jets (detailed further for any generic ML classifier in Chapter 5), while showing
 1282 strong rejection of light-flavour jets. This discriminant is used by applying a lower-bound
 1283 selection on the output of the BDT, such that any jet satisfying this requirement is tagged
 1284 as a b -jet. Four b -tagging efficiency working points are defined, each corresponding to a
 1285 different selection on the output of the BDT, providing an optimal balance of b -tagging
 1286 efficiency, ϵ_b , and c/τ /light-jet rejection. The working point used in the analyses detailed
 1287 in Chapters 6 and 7 is the $\epsilon_b = 77\%$ working point, corresponding to a selection on the
 1288 BDT output > 0.64 , which has a c -jet rejection of 4.9, a τ -jet rejection of 15 and a light-jet

1289 rejection of 110. The jet rejection rate is defined as the inverse of the selection efficiency,
 1290 $1/\epsilon_j$, where $j = c, \tau, \text{light}$. The efficiency of the MV2c10 b -tagging algorithm as a function
 of jet p_T is shown in Figure 4.6, along with the corresponding MC scale factors.

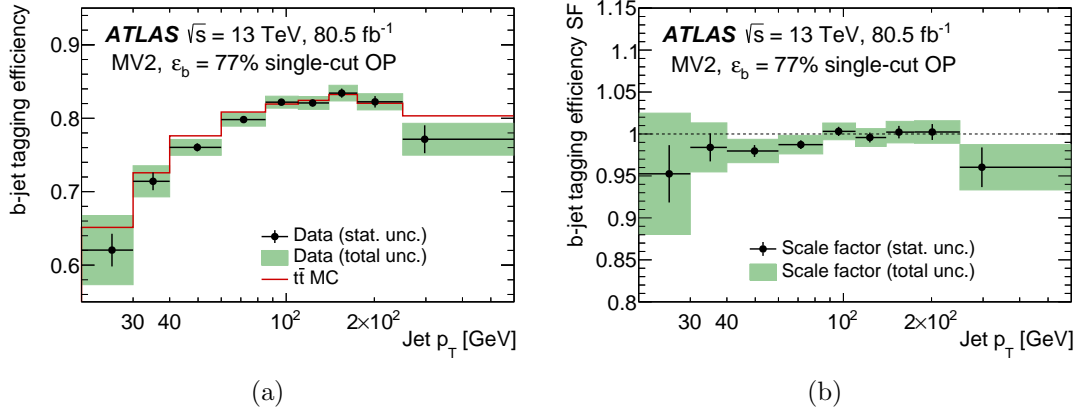


Figure 4.6: Figure showing the efficiency of the MV2c10 b -tagging algorithm as a function of the jet p_T (4.6a) and the corresponding MC scale factors (4.6b) for the $\epsilon_b = 77\%$ working point.

1291

1292 4.5 E_T^{miss}

1293 In searches for New Physics, it is expected that weakly-interacting BSM particles produced
 1294 in pp collisions will escape direct detection. Therefore, in order to perform such searches,
 1295 being able to reconstruct any momentum imbalance, indicating the presence of undetected
 1296 particles, is crucial. The hermetic design of the ATLAS detector with near 4π solid angle
 1297 coverage, as described in Chapter 2, enables the reconstruction of the momentum imbalance
 1298 in each event, with the magnitude of this vector sum known as the missing transverse
 1299 momentum, E_T^{miss} .

1300

1301 While the presence of E_T^{miss} is a signature of the production of weakly-interacting BSM
 1302 particles, it is not a unique signature of New Physics. As previously mentioned and as
 1303 shown in Figure 4.1, neutrinos pass through the entirety of the ATLAS detector without
 1304 interacting, and as such any SM decay involving neutrinos can be an irreducible back-
 1305 ground to a BSM signal. Aside from real E_T^{miss} from neutrinos, the accurate measurement
 1306 of the E_T^{miss} is complicated by detector imperfections; for example, physics objects being
 1307 mismeasured, or particles passing through inactive detector material.

1308

1309 The E_T^{miss} is calculated in x and y components, as shown in Equation 4.5.1, such that

1310 the E_T^{miss} vector is given by $\mathbf{E}_T^{\text{miss}} = (E_x^{\text{miss}}, E_y^{\text{miss}})$.

$$E_{x(y)}^{\text{miss}} = - \sum_i p_{x(y),i}^{\text{hard}} - \sum_i p_{x(y),i}^{\text{soft}}. \quad (4.5.1)$$

1311 The vectorial representation of E_T^{miss} allows both the magnitude and direction in ϕ to be
 1312 used in physics analyses. The magnitude and direction of the $\mathbf{E}_T^{\text{miss}}$, E_T^{miss} and ϕ^{miss} , are
 1313 given by Equations 4.5.2 and 4.5.3, respectively.

$$E_T^{\text{miss}} = \sqrt{(E_x^{\text{miss}})^2 + (E_y^{\text{miss}})^2} \quad (4.5.2)$$

1314

$$\phi^{\text{miss}} = \tan^{-1} \left(\frac{E_y^{\text{miss}}}{E_x^{\text{miss}}} \right) \quad (4.5.3)$$

1315 The reconstructed E_T^{miss} in ATLAS is constructed from two components; the ‘hard-event’
 1316 component, $E_T^{\text{miss, hard}}$, and the ‘soft-signal’ component, $E_T^{\text{miss, soft}}$. The former arises from
 1317 the reconstruction of the analysis-level electrons, photons, muons, τ_{had} , and jets, while the
 1318 latter arises from tracks and calorimeter deposits which are not associated with any of the
 1319 final state objects. The analyses described in Chapters 6 and 7 use the Track Soft Term
 1320 (TST) algorithm to calculate $E_T^{\text{miss, soft}}$, including all ID tracks associated with the PV
 1321 but not associated with any final state object. Using only tracks associated with the PV,
 1322 and excluded soft, neutral particle contributions, makes the soft E_T^{miss} term robust against
 1323 pileup effects.

1324 4.6 Overlap removal

1325 It is possible for multiple objects to be reconstructed from the same detector signatures,
 1326 such as calorimeter deposits, such that there are overlapping reconstructed objects. It is
 1327 therefore necessary to define a prescription through which to resolve this overlap. The
 1328 overlap removal procedure is performed on loosely reconstructed, ‘baseline’ objects and
 1329 proceeds as follows:

- 1330 - If two electrons share a track in the ID, the lower p_T electron is rejected.
- 1331 - If an electron shares an ID track with a muon, the electron is rejected.
- 1332 - Any non b -tagged jets within $\Delta R = 0.2$ of an electron are rejected, or within $\Delta R =$
 1333 0.2 of a muon if the jet has < 3 tracks or if the muon and jet are ghost-associated.
- 1334 - For the remaining jets, any electrons or muons satisfying $\Delta R < \min(0.4, 0.04 +$
 1335 $10\text{GeV}/p_T)$ are rejected.

1336 Objects remaining after the overlap removal procedure which pass the analysis-level recon-
 1337 struction criteria form the final analysis objects.

1338 4.7 Event cleaning

1339 In order to ensure recorded data events entering analyses are of good quality, a set of event
1340 cleaning requirements are used. These requirements aim to remove any events which has
1341 noisy detector signals or which are poorly measured. These are summarised below.

1342 **Good Run List** The Good Run List (GRL) is a record of all runs recorded by the
1343 ATLAS detector, which are deemed suitable for use in analyses. Typically, each run is
1344 broken down into 60s segments, known as *luminosity blocks*. Luminosity blocks in each
1345 run passing basic data quality requirements are included on the GRL. Events which were
1346 recorded in luminosity blocks or runs which are not included in the GRL are automatically
1347 rejected.

1348 **Trigger** Each analysis has differing trigger requirements depending on the signal topology
1349 of interest. In this Thesis, the E_T^{miss} triggers, listed in Table 3.1 are used.

1350 **Primary Vertex** All events must have a primary vertex (PV). As previously described,
1351 the PV is defined as the vertex having at least two tracks with the highest $\sum p_T^2$. Events
1352 which do not have a vertex satisfying these requirements are rejected.

1353 **SCT, LAr and Tile calorimeter cleaning** Noise bursts in the LAr calorimeter or
1354 Tile calorimeter trips can give incorrect measurements of the amount of electromagnetic
1355 or hadronic activity in an event, affecting the data quality. Events where such calorimeter
1356 activity was recorded are rejected. Events recorded during a reset of the SCT caused by
1357 a single particle upset (SEU) are also rejected. This occurs when there is a single particle
1358 upset (SEU) in a SCT module, which can cause the module to become extremely noisy
1359 until it is power-cycled.

1360 **Debug Stream** Events which cause the ATLAS software-level trigger, the HLT, to crash
1361 or timeout form the input to the debug stream. These events are stored and reconstructed
1362 offline, where they are assigned to the debug stream. It is particularly important for
1363 analyses searching for New Physics to check events in the debug stream.

1364 4.8 Object definitions summary

1365 The working points and selections on acceptance used to define ‘signal’ objects in the
1366 analyses detailed in Chapters 6 and 7 are summarised in Table 4.1. The procedures through
1367 which objects are reconstructed have sets of associated systematic uncertainties which will
1368 be discussed in Chapter 5.

Dataset	SUSY $1l\bar{b}b + E_T^{\text{miss}}$ 36.1fb^{-1}	139fb^{-1}	2HDM+a tW + E_T^{miss} 139fb^{-1}
<i>Electrons</i>			
ID	TightLLH		
Isolation	Gradient (Loose)	FCLoose (FCHighPtCaloOnly for $p_T > 200$ GeV)	FCLoose
p_T	> 25 GeV	> 7 GeV	> 20 GeV
$ \eta $	< 2.47		
<i>Muons</i>			
ID	Medium		
Isolation	Gradient (Loose)	FCLoose	FCLoose_FixedRad
p_T	> 25 GeV	> 6 GeV	> 20 GeV
$ \eta $	< 2.7	< 2.5	< 2.5
<i>Jets</i>			
Algorithm	anti- k_t , R = 0.4		
p_T	> 25 GeV	> 30 GeV	> 30 GeV
$ \eta $	< 2.8	< 2.8	< 2.5
<i>b-jets</i>			
Tagger	MV2c10		
p_T	> 25 GeV	> 20 GeV	> 20 GeV
$ \eta $	< 2.5		
<i>b</i> -jet efficiency	FixedCutBEff, $\epsilon = 77\%$		

Table 4.1: A summary of the object definitions used in the analyses detailed in Chapters 6 and 7.

1369 Chapter 5

1370 Analysis methods

1371 This Chapter aims to summarise the methods and tools used to perform the searches for
1372 New Physics described in the subsequent Chapters. Firstly, the general analysis strategy
1373 used in a search for New Physics is presented, with more relevant and specific detail given in
1374 Chapters 6 and 7. The key discriminatory variables used in this Thesis to select candidate
1375 signal events are described in Section 5.2. Section 5.3 of this Chapter describes some
1376 of the multivariate and machine learning (ML) methods used to select and optimise the
1377 acceptance of signal into the analyses, giving an overview of both conventional and more
1378 modern data selection techniques. Finally, Section 5.5 gives an overview of the statistical
1379 analysis performed and the methods used to draw statistical conclusions from the analyses
1380 detailed in the subsequent Chapters.

1381 5.1 General search analysis strategy

1382 Physics analyses targeting a BSM scenario generally define three classes of regions of phase
1383 space. *Signal regions* (SRs) are defined as regions of kinematic phase space which are en-
1384 riched in the signal of interest. SRs can be defined by placing selections on kinematic and
1385 angular observables, such as the E_T^{miss} or the angular difference between two jets $\Delta\phi(j_1, j_2)$,
1386 or through more abstract techniques such as placing a selection on some classifier trained
1387 to distinguish the signal of interest from the SM background. The latter will be discussed
1388 in Section 5.3.

1389

1390 *Control regions* (CRs) are defined as regions whose composition is dominated by a par-
1391 ticular background process, such as $t\bar{t}$, while also having negligible signal contamination.
1392 Generally, SRs in searches are in an extreme part of kinematic phase space, far from where
1393 the SM background MC was validated, hence it is necessary to ensure reasonable agree-
1394 ment between data and the SM predictions for the background estimates in the CRs. A SM
1395 estimate is made for the controlled background in the corresponding CR by normalising
1396 the MC predictions to the observed data in that CR by fitting a floating normalisation

1397 factor, typically denoted by μ_{process} . The background normalisation factor, μ_{process} , is both
 1398 determined from and subsequently applied to all analysis regions included in the statistical
 1399 analysis. This will be discussed further in Section 5.5.

1400

1401 *Validation regions* (VRs) are used as a method of ensuring the background estimation
 1402 from the CR extrapolated to the SR is robust. Generally, this is achieved by defining VRs
 1403 which differ from the SR definition by inverting only one SR selection. By defining multiple
 1404 VRs, each with a different SR selection inverted, the extrapolation from CR to SR can be
 1405 validated. However, VRs must also have low signal contamination, such that it is indeed
 1406 the background estimate that is being validated.

1407

1408 A simplified diagram showing how CRs, VRs and SRs can be defined in terms of two
 observables is shown in Figure 5.1.

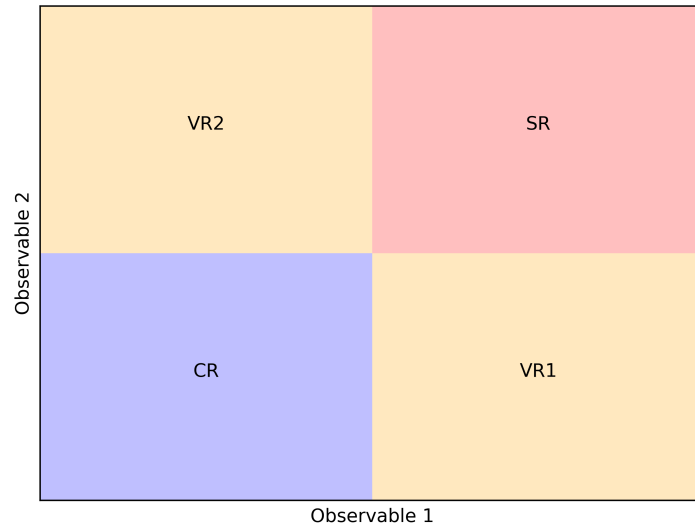


Figure 5.1: A simplified schematic diagram showing an example of a CR, VRs and an SR, all defined by placing orthogonal selections on two observables. The background estimation made in the CR is extrapolated and validated through VR1 and VR2 into the SR.

1409

1410 5.2 Discriminant variables

1411 The analyses detailed in Chapters 6 and 7 have similar final states signatures including a
 1412 single lepton, b -tagged jets and $E_{\text{T}}^{\text{miss}}$, and hence have very similar SM backgrounds to the
 1413 respective signals. In particular, the presence of intermediate W bosons and $E_{\text{T}}^{\text{miss}}$ in the
 1414 signal processes presented in Chapters ?? and 7 makes SM processes involving W bosons
 1415 which decay leptonically an irreducible background to the signal. In addition, backgrounds

1416 containing at least one top quark, where an intermediate W boson from $t \rightarrow Wb$ decays
 1417 leptonically, are also irreducible due to the presence of a lepton, E_T^{miss} and b -tagged jets.
 1418 In the analyses presented in Chapters 6 and 7, the $t\bar{t}$, Wt and W +jets processes are the
 1419 largest, irreducible backgrounds to the signals of interest. This Section aims to summarise
 1420 the variables used to reject these SM backgrounds while retaining the signal.

1421

1422 The first, and perhaps most obvious, variable used to discriminate between a BSM signal
 1423 and the SM backgrounds is E_T^{miss} . The construction of the E_T^{miss} is described in Chapter 4.
 1424 Processes which contain BSM particles have real E_T^{miss} if the BSM particles do not decay
 1425 to visible particles, and hence could produce an excess of events in the E_T^{miss} distribution.
 1426 In such events, the amount of E_T^{miss} is expected to be larger than the SM background,
 1427 due to the presence of the additional BSM particles. However, real E_T^{miss} from neutrinos
 1428 in $W \rightarrow \ell\nu$ or $Z \rightarrow \nu\nu$ decays as well as E_T^{miss} from misreconstructed jets can obscure
 1429 a BSM signal. Therefore, a combination of applying selections on the E_T^{miss} distribution
 1430 with other kinematic selections is employed.

1431

1432 The transverse mass variable, m_T , can be used to reconstruct a single, massive particle
 1433 undergoing a semi-invisible decay to one visible particle and one invisible particle. In this
 1434 Thesis, the m_T variable is used to reconstruct W bosons, decaying to a charged lepton and
 1435 a neutrino. In the case of an event with no BSM contributions, the only source of E_T^{miss} is
 1436 from the neutrino produced in the decay of the W boson and as such the m_T distribution
 1437 has a kinematic endpoint around m_W . Detector effects smear the kinematic endpoint of
 1438 the m_T distribution to around 100 GeV. The presence of E_T^{miss} from BSM particles will
 1439 produce a significantly different m_T distribution with a significantly longer tail compared
 1440 to a SM-only case, and is therefore a powerful discriminant. The definition of m_T is given
 1441 in Equation 5.2.1.

$$m_T = \sqrt{2p_T(\ell)E_T^{\text{miss}}(1 - \cos\Delta\phi(\mathbf{p}_T(\ell), \mathbf{p}_T^{\text{miss}}))} \quad (5.2.1)$$

1442 In Equation 5.2.1, $p_T(\ell)$ is the transverse momentum of the lepton in the event while
 1443 $\Delta\phi(\mathbf{p}_T(\ell), \mathbf{p}_T^{\text{miss}})$ specifies the azimuthal angle between the lepton and the E_T^{miss} . For the
 1444 signal process of interest in the analysis detailed in Chapter 7, there are two intermediate
 1445 W bosons, producing the single lepton final state as follows: $Wt \rightarrow W(Wb) \rightarrow (\ell\nu)(qq')b$.
 1446 In addition to reconstructing the leptonically-decaying W boson using the m_T variable,
 1447 the reconstruction of the hadronically-decaying W boson was achieved using an iterative
 1448 reconstruction procedure, as described in [34]. The algorithm begins by clustering all of
 1449 the $R = 0.4$ anti- k_t jets in an event into large, $R = 3.0$ jets. The radius of these large
 1450 jets is then iteratively reduced until a radius which matches the p_T of the jet, defined by
 1451 $R(p_T) = 2 \times m_W/p_T$, is reached. The mass of these ‘reclustered’ W boson candidates is
 1452 denoted m_W^{had} .

1453

1454 The contranverse mass [35, 36], m_{CT} , is designed to reconstruct the masses of pair-
 1455 produced particles which both decay in the same, semi-invisible manner. This is par-
 1456 ticularly useful for rejecting the $t\bar{t}$ process, where both legs decay into a W boson and a
 1457 b -quark, followed by a subsequent decay of the W bosons. The m_{CT} is defined in Equation
 1458 5.2.2.

$$m_{CT}^2 = (E_T(v_1) + E_T(v_2))^2 - (\mathbf{p}_T(v_1) - \mathbf{p}_T(v_2))^2 \quad (5.2.2)$$

1459 The version of m_{CT} shown in Equation 5.2.2 violates Lorentz invariance under boosts of
 1460 the laboratory centre-of-mass frame, and hence a modified, ‘boost-corrected’ version [36] is
 1461 used in the analysis detailed in Chapter ?? . For this analysis, the visible particles v_1 and
 1462 v_2 are identified as the two b -jets in the event, b_1 and b_2 , in order to partially reconstruct
 1463 the $t\bar{t}$ system. As described in [36], the m_{CT} distribution has a kinematic endpoint which
 1464 can be calculated as shown in Equation 5.2.3.

$$m_{CT}^{\max} = \frac{m_{heavy}^2 - m_{invisible}^2}{m_{heavy}} \quad (5.2.3)$$

1465 Identifying $m_{heavy} = m_{top}$ and $m_{invisible} = m_W$ gives a kinematic endpoint around 135
 1466 GeV for $t\bar{t}$ production, which is the most dominant background in the analysis detailed in
 1467 Chapter 6.

1468

1469 The transverse mass variable, m_{T2} [37] is closely related to the transverse mass vari-
 1470 able, m_T . It is again designed to reconstruct the mass of pair-produced particles, most
 1471 relevantly here $t\bar{t}$, where each particle decays semi-invisibly. The m_{T2} is shown in Equation
 1472 5.2.4 for a two-lepton final state.

$$m_{T2} = \min_{\mathbf{q}_T} [\max(m_T(\mathbf{p}_T(\ell_1), \mathbf{q}_T), m_T(\mathbf{p}_T(\ell_2), \mathbf{p}_T^{\text{miss}} - \mathbf{q}_T))] \quad (5.2.4)$$

1473 An asymmetric form of m_{T2} [38, 39], known as am_{T2} , is used in the analysis detailed
 1474 in Chapter 7. When a pair of top quarks are produced and subsequently decay semi-
 1475 leptonically, a selection applied to m_T above the W boson threshold will reject most
 1476 events. However, for dileptonic $t\bar{t}$ where one lepton is not reconstructed, cuts applied on
 1477 the m_T variable will not be enough to reject this process, as there is E_T^{miss} from both legs
 1478 due to the neutrinos. Selections on the am_{T2} variable can be applied in combination with
 1479 selection on m_T to reject both semi- and dileptonic $t\bar{t}$ decays.

1480 5.3 Selection optimisation methods

1481 Searches for New Physics often involve signals which have cross-sections orders of magni-
 1482 tude lower than those of SM processes. It is therefore necessary to design analyses which

1483 minimise the background contributions in the SRs, while also maintaining a high accep-
 1484 tance and selection efficiency for the signal of interest. Optimising SRs to satisfy these
 1485 criteria is non-trivial, particularly when considering a large number of observables, and
 1486 can often result in unreasonable computing times and loads.

1487

1488 Placing simple selections on the discriminating variables described previously does not
 1489 give sensitivity to the signals of interest due to the huge irreducible SM backgrounds. In
 1490 order to separate signals from the SM background, more sophisticated optimisation meth-
 1491 ods are used which take advantage of numerous discriminative variables in parallel. The
 1492 methods used for region optimisation in this Thesis can be divided into two categories;
 1493 ‘grid-based’ methods, and machine learning methods. Grid-based methods aim to find the
 1494 optimum selection on each of the discriminative variables used in an analysis. For each
 1495 variable, a set of proposed selections is defined. Each candidate region is defined as one
 1496 combination of the proposed selections, with the full set of proposed regions forming a
 1497 ‘grid’. The total number of candidate regions is given by the product of the number of
 1498 proposed selections for each variable, and hence rapidly grows as additional variables are
 1499 added, or more proposed selections are tested. Therefore, for a grid with many candidate
 1500 regions it is often impossible to test every region, and hence some grid-based algorithms
 1501 aim to search the grid for an optimal solution without explicitly testing each candidate
 1502 region. Machine learning (ML) classifiers do not explicitly optimise selections on individual
 1503 discriminative variables and instead aim to classify events based upon the values of the
 1504 variables. The inputs to ML classifiers are generally the discriminative variables of interest
 1505 in an analysis. The classifier is trained to discriminate between the signal and the SM
 1506 backgrounds by repeatedly being given events from each class and learning the differences
 1507 between the distributions. ML classifiers make predictions on an event being signal-like or
 1508 background-like, by outputting a number in the range $\in [-1, 1]$ or $\in [0, 1]$, depending on
 1509 the classifier implementation, where predictions $\rightarrow 1$ represent a signal-like event. For ML
 1510 classifiers, the SRs are defined by applying a lower bound selection to the distribution of
 1511 the ML classifier predictions. The location of this selection is optimised by scanning over
 1512 cuts and determining the optimal selection.

1513

1514 In order to determine the optimal solution in grid-based methods and determine the loca-
 1515 tion of the optimal cut on the ML classifier output, the *significance* metric is defined. The
 1516 definition of the significance metric used to assess the sensitivity of a region in this Thesis,
 1517 denoted by Z and described in detail in [40], is shown in Equation 5.3.1.

$$Z = k \sqrt{2 \left(n \ln \left[\frac{n(b + \sigma^2)}{b^2 + n\sigma^2} \right] - \frac{b^2}{\sigma^2} \ln \left[1 + \frac{\sigma^2(n - b)}{b(b + \sigma^2)} \right] \right)} \quad (5.3.1)$$

1518 In Equation 5.3.1, n is the number of observed events, b is the expected number of events,
1519 and σ is the uncertainty on the prediction b . The factor $k = 1$ for $n \geq b$, while $k = -1$
1520 for $n < b$. The significance is typically evaluated for several benchmark signal models
1521 with specific parameter choices, targeting a particular region of the signal kinematic phase
1522 space. In this Thesis, the σ is estimated as being 30%, representing a conservative estimate
1523 of the dominant modelling and experimental systematics. A well-optimised SR will max-
1524 imise the significance for the targeted signal phase space, while keeping SM background
1525 contributions to a minimum. However, in maximising the significance, it must be ensured
1526 that the SR is robust against statistical limitations arising from the MC. A SR which is
1527 underpopulated in MC events can give an unreasonably-high estimated significance, and
1528 as such it is typically required that there are at least 10 events in the MC for each major
1529 SM background, and also for the signal MC sample(s) used for region optimisation.

1530

1531 Details on the specific grid-based and ML methods used are given in the following subsec-
1532 tions.

1533 **Grid-based methods**

1534 Grid-based optimisation methods define a grid of proposed regions, each defined by unique
1535 selections on each of the discriminative variables. For each variable, there are N_i test cuts,
1536 where i denotes the given variable, such that the total number of combinations of cuts,
1537 N , is given by $N = \prod_{i=1}^M N_i$. As N is given by a product, the number of combinations
1538 rapidly grows with grid granularity and the number of variables tested. In addition, these
1539 methods are often run on several benchmark signal models, each with different parameter
1540 choices. This ensures good sensitivity can be achieved across a wide range of the available
1541 kinematic phase space. Numerous grid-based methods were used in this Thesis, and will
1542 now be discussed.

1543 **Inclusive grid search**

1544 An ‘inclusive’ grid search finds the optimal combination of selections by calculating the
1545 significance for each benchmark signal model for *every* candidate region and returning the
1546 region with highest significance for each signal. While this method is guaranteed to find
1547 the region with the highest significance for each benchmark signal model, the number of
1548 tests rapidly grows with increasing numbers of input variables or with a large number of
1549 proposed regions. The limiting factor of this method is the computational time required
1550 to find the optimal region through evaluating the significance for every combination. The
1551 subsequent grid-based methods evade this issue by randomly sampling points on the grid
1552 of candidate regions.

1553 **Random grid search**

1554 The random grid search (RGS) algorithm samples random points from the grid of candidate
1555 regions, evaluating the significance for each. To alleviate the computational requirements
1556 of the ‘inclusive’ grid search, the RGS algorithm typically samples a small portion of the
1557 grid, running for i iterations, calculating the significance at that point, and then removing
1558 that point from the grid. Due to the random nature of the RGS algorithm, it is never
1559 guaranteed that the algorithm will find an optimal solution without sampling the entire
1560 grid. Therefore, the RGS algorithm is run numerous times to ensure the highest significance
1561 combination it achieved can not be improved. Additionally, the RGS algorithm is run for
1562 several benchmark signal models, to ensure sensitivity across the kinematic phase space.

1563 **Adaptive random grid search**

1564 The RGS algorithm enables a large portion of a potential signal phase space to be probed
1565 without the computational expensive of studying the phase space grid at every point in-
1566 clusively. However, the RGS method, by definition, randomly samples the grid of points
1567 with no ‘awareness’ of the significance. Hence, the RGS algorithm can sample a point with
1568 high significance, potentially close to the optimal solution, before randomly moving to a
1569 region of low significance. To circumvent this, a modified version of the RGS algorithm,
1570 known as the *adaptive* random grid search (ARGS), was developed. Instead of allowing the
1571 movement between any two points on the grid, the ARGS algorithm adapts the step size
1572 in a significance-aware way. Around regions of high significance, where $Z \geq 2$, the step size
1573 shrinks to allow a high-granularity study of the phase space around the point of interest.
1574 Once the significance falls below $Z = 2$, the step size grows again to allow bigger steps
1575 between grid points. Finally, once the significance drops below the activation threshold,
1576 $Z = 0.5$, the algorithm is free to move between any points on the grid, and is equivalent
1577 to the RGS algorithm.

1578 **Genetic algorithm**

1579 The genetic algorithm (GA) takes inspiration from the process of natural selection, in
1580 which the ‘fittest’ individuals survive the sequential evolution of the system. The GA
1581 starts by generating a ‘population’ of N combinations of cuts. The significance of each
1582 combination is calculated, with the lowest 50% of combinations discarded. The surviving
1583 50% of combinations, known as the ‘parents’, are then copied, and undergo ‘cross-over’
1584 and ‘mutation’, to produce ‘offspring’. For the cross-over step, the offspring are ordered
1585 in terms of significance. In the cross-over step, adjacent offspring randomly switch values
1586 of cuts, while in the subsequent mutation step, random cut values are smeared using
1587 a Gaussian distribution. The significance of both the parents and the offspring are re-
1588 evaluated, and the process repeats, selecting the best-performing 50%. This process repeats

1589 for a predefined number of iterations, $i = 100$, terminating early if the best significance
1590 found doesn't improve in 10 iterations.

1591 Machine learning methods

1592 Machine learning (ML) techniques are a wide and active area of research, and this section
1593 does not aim to review the state of ML research. Instead, it aims only to give an overview
1594 of the usage of ML in this context and describe the ML methods used in this Thesis, in
1595 particular the use of supervised learning ML *classifiers* to separate a signal from the SM
1596 background. Two types of classifier are relevant in this Thesis; Boosted Decision Trees
1597 (BDTs) and Deep Neural Networks (DNNs). Each will be described in their own section,
1598 along with details of their implementation.

1599

1600 ML models are, when first created, a completely general model described by a set of
1601 parameters, known as *hyperparameters*. The set of hyperparameters used are chosen to
1602 maximise the performance of the model, while allowing the model to be robust against un-
1603 seen data. The ML models used in this Thesis, as previously mentioned, act as classifiers,
1604 predicting on an event-by-event basis which of a finite number of classes an event belongs
1605 to. This is particularly useful in searches, where one wishes to discriminate a signal from an
1606 often irreducible SM background. To give these models the ability to discriminate between
1607 the SM backgrounds and signal, they undergo *training*. The models are trained on MC,
1608 meaning the class of each event is known during the training phase, which is known as
1609 *supervised* learning. ML models can be susceptible to learning the input events and hence
1610 become unable to make meaningful predictions about unseen data, known as *overtraining*.
1611 In order to overcome this, the performance of the model is evaluated on a statistically-
1612 independent sample of events, known as the *validation* sample.

1613

1614 While the structure of each type of ML model is different, the inputs to and outputs
1615 of the models are the same. The inputs to the ML models used in this Thesis are physical
1616 observables, such as the amount of E_T^{miss} or the transverse momentum of the objects in
1617 the event. The outputs of the ML models used are a number within in a fixed range. In
1618 the case of binary classification, where only two classes are defined, the output of the ML
1619 model is in the range $\in [-1, 1]$ for classifiers implemented in TMVA [41], and otherwise
1620 $\in [0, 1]$. For multiclass classification, where the number of classes $N_{\text{class}} > 2$, the ML
1621 model outputs N_{class} values in the range $\in [0, 1]$, the sum of which are 1, where each value
1622 represents the prediction for a given class. In this case, events are assigned a class based
1623 upon which class score was highest.

1624 Boosted Decision Trees

1625 Boosted Decision Trees (BDTs) are constructed from an ensemble of decision trees, known
 1626 as *weak classifiers*. Decision trees are constructed from nodes and leaves, with each node
 1627 representing a test condition on one of the input variables, and each leaf representing a
 1628 class label. Each individual decision tree has limited discrimination power when evaluated,
 1629 and hence techniques such as *boosting* [42] are used to create an ensemble of weak classifiers
 1630 with strong discrimination power. The boosting technique proceeds by iteratively creat-
 1631 ing trees and assigning each tree a corresponding weight, w_i , related to the classification
 1632 accuracy of the tree.

1633

1634 During the training phase, the boosting procedure is used to minimise the differences
 1635 between the prediction of the classifier, $F(\mathbf{x})$, given the inputs \mathbf{x} , and the true class of the
 1636 input data, y_{truth} . The difference between the prediction of a classifier and the true class
 1637 of an event is calculated using a *loss function*. The BDTs implemented in TMVA utilise
 1638 the AdaBoost algorithm [43], while the BDTs implemented in XGBoost [44] use gradient
 1639 boosting. During training, the AdaBoost algorithm proceeds by adjusting the weight of
 1640 each decision tree in the ensemble to minimise an exponential loss function. However,
 1641 the gradient boosting algorithm creates a new tree at each training iteration, fitted to the
 1642 residual $y_{\text{truth}} - F(\mathbf{x})$, to minimise a logarithmic loss function.

1643

1644 The studies performed in Chapter 8 use BDTs implemented with TMVA. These BDTs
 1645 use an inverse sigmoid transformation on the output of the form $y' = -\tau^{-1} \ln(y^{-1} - 1)$,
 1646 where $\tau = 15$ [41]. The studies presented in Section 6.6 use BDTs implemented with
 1647 XGBoost.

1648 Neural Networks

1649 Neural Networks (NNs) take inspiration from the structure of neural connections in the
 1650 brain. A neural network is constructed from an input layer, an output layer and one or
 1651 more hidden layers. A NN with 1 hidden layer is classed as a ‘shallow’ NN, while NNs with
 1652 more than 1 hidden layer are classed as a ‘deep’ NN (DNN). Each layer in a NN is con-
 1653 structed from nodes, with the number of nodes in the input layer being determined by the
 1654 number of input variables, and the number of nodes in the output layer being determined
 1655 by the classification mode of the network. For binary classification, the NN will have a
 1656 single node in the output layer, while for multiclass classification there will be N_{class} nodes,
 1657 one for each class.

1658

1659 The connections between the nodes in the layers depends upon the structure of the NN. In
 1660 this Thesis, the NNs used are ‘fully-connected’, meaning each node is connected to all of
 1661 the nodes in the previous and next layer. These connections, known as *synapses*, each have

1662 a corresponding weight w_i , where i represents the index of the input node in the previous
 1663 layer. The input to a node in a layer is given by the weighted sum of the outputs of the
 1664 nodes in the previous layer, as follows:

$$y = \sum_i w_i x_i + b . \quad (5.3.2)$$

1665 In Equation 5.3.2, w_i represents the synaptic weight connecting the i th node in the previous
 1666 layer to the given node, x_i is the output of the i th node in the previous layer and b is the
 1667 bias. Each layer in a NN has a defined *activation function*, which acts upon the input to
 1668 a node to produce an output value. The hidden layers in the NNs used in this Thesis use
 1669 a Rectified Linear Unit (ReLU) activation, which is defined as $y(x) = \max(0, x)$. For the
 1670 output layer, the sigmoid activation function is used for binary classification, while the
 1671 softmax activation function is used for the multiclass case.

1672 5.4 Estimating systematic uncertainties

1673 There are two, broad classes of systematic uncertainties that need to be considered when
 1674 performing an ATLAS analysis; *experimental* uncertainties, related to uncertainties in the
 1675 reconstruction of the physics objects in an event, and *modelling* uncertainties, related to
 1676 choices made in the MC simulation employed to aid in the estimate of the SM background
 1677 or signal process.

1678 Experimental uncertainties

1679 Uncertainties arise in the simulation and reconstruction of the physics objects described
 1680 in Chapter 4. Experimental uncertainties can affect both the normalisation and shape of
 1681 distributions, meaning the number of reconstructed objects, e.g. leptons, passing region
 1682 selections can vary. This Section briefly describes the experimental systematics evaluated
 1683 in the analyses detailed in Chapters 6 and 7.

1684 **Luminosity** The integrated luminosity of the dataset is determined using van Der Meer
 1685 scans, first described in [45] and elaborated upon for ATLAS in [46]. The luminosity un-
 1686 certainty affects the normalisation of MC predictions, and ultimately the model-dependent
 1687 and model-independent limits of an analysis. For the analysis detailed in Chapter 6, which
 1688 uses data collected in 2015-2016, the luminosity uncertainty is determined to be 2.1%,
 1689 while for the analysis detailed in Chapter 7, using the full Run-2 dataset collected between
 1690 2015-2018, the luminosity uncertainty is determined to be 1.7%.

1691 **Jets** As previously described in Section 4.3, the energy of reconstructed jets must be
 1692 corrected to account for calorimeter non-compensation, detector acceptance and defects

1693 and pileup. The JES calibration is derived using MC simulation and data [47], and the
 1694 JES uncertainties arise from choices made when developing this calibration. The full
 1695 JES uncertainty set totals around 100 nuisance parameters, while a reduced set of JES
 1696 uncertainties totalling 7-8 parameters is also provided for analyses which are insensitive to
 1697 small variations in the calibration [48].

1698 The energy of jets cannot be measured exactly, despite the corrections to the jet energy
 1699 from the JES calibration. The Jet Energy Resolution (JER) is defined as the width of
 1700 the Gaussian distribution describing the measured jet energy at the calibrated jet energy
 1701 scale. The JER is determined from both data and MC [49], with its uncertainty arising
 1702 from choices made when determining the JER.

1703 **Flavour-tagging** Uncertainties arise in the b -tagging calibration from experimental and
 1704 modelling sources. The flavour-tagging efficiencies are derived from the comparison of
 1705 dileptonic $t\bar{t}$ events, and as such choices made in the generation of the $t\bar{t}$ MC affect the
 1706 measured efficiencies.

1707 **Leptons** Uncertainties that arise in the reconstruction of leptons are related to the lep-
 1708 ton energy resolution and scale calibrations, as well as the efficiencies corresponding to
 1709 the reconstruction, identification and isolation. In this Thesis, lepton trigger efficiency
 1710 uncertainties are neglected due to the use of the E_T^{miss} triggers in the analyses detailed in
 1711 Chapters 6 and 7.

1712 **Missing transverse energy** The uncertainties on the E_T^{miss} are separated into uncer-
 1713 tainties affecting the $E_T^{\text{miss, hard}}$ and the $E_T^{\text{miss, soft}}$ components, as described in Section 4.5.
 1714 The uncertainties on the hard E_T^{miss} term are derived by propagating the individual energy
 1715 scale and resolution uncertainties on the physics objects in an event to the E_T^{miss} . The
 1716 energy scale and resolution of the soft E_T^{miss} term are evaluated using data and MC as
 1717 described in [50].

1718 Modelling uncertainties

1719 Numerous sources of uncertainty arise in the modelling of SM backgrounds and signal.
 1720 Typically, the dominant modelling systematics come from the specific choice of generator
 1721 used to evaluate the ME and the choice of algorithm used to model the PS. In terms
 1722 of specific modelling uncertainties, the interference between the $t\bar{t}$ and Wt processes is
 1723 often large, as described in Section 3.3. Modelling systematics are evaluated by simulating
 1724 the same physical process with two MC production configurations, taking the difference
 1725 between the nominal and variation MC predictions as the 1σ uncertainty. This uncertainty
 1726 is then applied in the statistical analysis as a 2-sided systematic affecting the normalisation
 1727 and/or shape of the nominal distributions of the corresponding process. A general overview

1728 of the sources of modelling uncertainty are described here, while specific information on
 1729 the procedure used to evaluate the individual modelling uncertainties are given in Chapters
 1730 ?? and 7.

1731 **Uncertainty calculation** As previously mentioned, modelling uncertainties are calcu-
 1732 lated by comparing two MC predictions and taking the difference as the 1σ variation, which
 1733 is known as a 2-point systematic. For backgrounds which are estimated using MC-only, the
 1734 systematic in a given analysis region is calculated using the difference of the predictions
 1735 of the two MC samples, as shown in Equation 5.4.1. The MC sample used as a variation
 1736 can either be a statistically-independent sample, generated in a different configuration, or
 1737 a weight-based variation of the nominal sample, where an alternate MC weight is applied
 1738 to the nominal MC.

$$\alpha_{\text{syst}}^{\text{process}} = \pm \left| \frac{N(\text{MC})_{\text{variation}}^{\text{process}} - N(\text{MC})_{\text{nominal}}^{\text{process}}}{N(\text{MC})_{\text{nominal}}^{\text{process}}} \right| \quad (5.4.1)$$

1739 For the analysis detailed in Chapter 6, the modelling uncertainties on the $t\bar{t}$, Wt and
 1740 W +jets processes are estimated using transfer factors between the CR and SR/VR. The
 1741 transfer factor between the CR and SR for a given process is shown in Equation 5.4.2.

$$\text{TF}_{\text{syst}}^{\text{process}} = \frac{N(\text{MC}, \text{SR})_{\text{syst}}^{\text{process}}}{N(\text{MC}, \text{CR})_{\text{syst}}^{\text{process}}} \quad (5.4.2)$$

1742 The uncertainty in the SR is then given by the difference in transfer factors estimated
 1743 using the nominal and variation MC samples, as shown in Equation 5.4.3.

$$\alpha_{\text{syst}}^{\text{process}} = \Delta \text{TF}_{\text{syst}}^{\text{process}} = \pm \left| \frac{\text{TF}_{\text{variation}}^{\text{process}} - \text{TF}_{\text{nominal}}^{\text{process}}}{\text{TF}_{\text{nominal}}^{\text{process}}} \right| \quad (5.4.3)$$

1744 The transfer factor approach is not used in the analysis detailed in Chapter 7 as the SR
 1745 bins each have a very different $E_{\text{T}}^{\text{miss}}$ spectrum, while the CRs are defined using a single
 1746 $E_{\text{T}}^{\text{miss}}$ bin, and hence the extrapolation from the single-bin CRs to SR bins is difficult
 1747 to validate. Therefore, modelling uncertainties in this analysis are evaluated using the
 1748 prescription described in Equation 5.4.1.

1749 **PDF uncertainties** The uncertainty due to the choice of the nominal PDF set was
 1750 found to be $\mathcal{O}(1\%)$ on the dominant backgrounds, which is far less than the dominant
 1751 systematics and statistical uncertainties. Hence, PDF uncertainties are neglected in this
 1752 Thesis.

1753 **Generator uncertainties** The choice of generator used to model the hard scatter is
 1754 typically driven by the agreement between the MC predictions and data, with the generator
 1755 which best reproduces the data across a range of phase space being deemed the nominal

1756 choice. In order to ensure the estimate of the nominal generator is robust in the analysis
 1757 phase space, the uncertainty on the calculation of the ME is evaluated by generating an MC
 1758 sample which uses a different generator for the hard scatter, but is interfaced to the same
 1759 PS algorithm. Variations of the generator uncertainty are not available for all processes;
 1760 in this Thesis, the generator uncertainties are evaluated for the top-pair, single top and
 1761 $t\bar{t}V$ processes.

1762 **Parton showering uncertainties** Similarly to generator uncertainties, the nominal
 1763 choice of PS algorithm is driven by the agreement between data and MC predictions.
 1764 To estimate the impact of using a different PS algorithm, the nominal configuration is
 1765 compared with a MC sample which is produced using the same generator for the hard
 1766 scatter but using a different PS algorithm. Again, this is evaluated only for the top-pair,
 1767 single top and $t\bar{t}V$ processes.

1768 **Scale uncertainties** Numerous choices of scale are made when producing MC samples,
 1769 such as the value of α_S , μ_R and μ_F . For the W/Z +jets, diboson and triboson backgrounds,
 1770 the predictions of 7 variations of μ_R and μ_F are evaluated, with the values of μ_R and μ_F
 1771 being evaluated at $0.5\times$, $1.0\times$ and $2.0\times$ the nominal values. The maximum downwards
 1772 and upwards variation then define the asymmetric uncertainty on these scale choices. As
 1773 mentioned in Section 3.2, there can be overlap between a LO with PS and NLO process,
 1774 and hence matching and/or merging is used to remove the overlap. For the W/Z +jets
 1775 backgrounds, the choice of scale used to perform such matching is varied from the nominal
 1776 value of 20 GeV to 15 GeV and 30 GeV.

1777 5.5 Statistical analysis

1778 All statistical analyses performed in this Thesis were implemented in the HistFitter frame-
 1779 work [51]. This framework requires an analysis structure similar to that shown in Figure
 1780 5.1. The use of CRs in the fit allows background process yields to be corrected to data,
 1781 such that any mismodelling of data by the MC can be minimised in the SRs.

1782
 1783 Fits using this framework utilise the background CRs to make estimates of the back-
 1784 grounds in the SR by normalising the expected number of background events from the MC
 1785 to data. Each background with a corresponding CR, known as a *normalised* background,
 1786 acquire a normalisation factor, μ_p . This normalisation factor is derived by comparing the
 1787 number of expected and observed events in a given CR for a given normalised background,
 1788 enabling an extrapolation to the SR as shown in Equation 5.5.1.

$$N_{\text{process}}^{SR}(\text{Exp}) = \mu_p \cdot N_{\text{process}}^{SR}(\text{MC}) \quad (5.5.1)$$

1789 In Equation 5.5.1, the number of expected events in a given region for a given process,
 1790 $N_{\text{process}}^{SR}(\text{Exp})$, is calculated by multiplying the expected number of events for that process
 1791 in that region from the MC, $N_{\text{process}}^{SR}(\text{MC})$, by the process-specific normalisation factor, μ_p ,
 1792 which is calculated automatically when performing the fit.

1793

1794 Fits are performed by constructing a likelihood function, L , depending upon the expected
 1795 number of MC events in each CR and SR, the systematic uncertainties arising from statisti-
 1796 cal, experimental and theoretical sources on these backgrounds, and the observed number
 1797 of events in each CR and SR. The likelihood function used by HistFitter is shown in
 1798 Equation 5.5.2.

$$L(n, \theta^0 | \mu_{\text{sig}}, b, \theta) = P(n_S | \lambda_S(\mu_{\text{sig}}, b, \theta)) \times \prod_{i \in CR} P(n_i | \lambda_i(\mu_{\text{sig}}, b, \theta)) \times C_{\text{syst}}(\theta^0, \theta) \quad (5.5.2)$$

1799 The likelihood function is constructed around a product of Poisson distributions of ob-
 1800 served (n_S, n_i) and expected (λ_S, λ_i) events in the SR and CRs, respectively. The Poisson
 1801 expectations, λ_S and λ_i , depend upon the background prediction, b and the corresponding
 1802 nuisance parameters representing the systematic uncertainties, θ , as well as the signal
 1803 strength parameter, μ_{sig} . The signal strength parameter can be set to 0 to remove signal
 1804 being considered in the fit, or if considering signal can be set to 1 to include the nominal
 1805 signal yield estimate for a signal under consideration. The systematics term, $C_{\text{syst}}(\theta^0, \theta)$,
 1806 shown in Equation 5.5.3 is defined as a product of Gaussian constraints, θ_j , each represent-
 1807 ing a systematic variation, which are varied around $\theta_j^0 = 0$ when maximising the likelihood
 1808 function.

$$C_{\text{syst}}(\theta^0, \theta) = \prod_{j \in S} G(\theta_j^0 - \theta_j) \quad (5.5.3)$$

1809 In searches for New Physics, test statistics are used to quantify the agreement between the
 1810 expected and observed yields in a given region. Of particular interest in this Thesis are the
 1811 p -value and the CL_s . The p -value, given a hypothesis H_0 , is interpreted as the probability
 1812 that the alternate hypothesis, H_1 , can provide a result at least as incompatible with H_0 as
 1813 the observed result. The definition of the p -value is given in Equation 5.5.4.

$$p = \int_{t_{\text{obs}}}^{+\infty} g(t|H_0) dt \quad (5.5.4)$$

1814 In Equation 5.5.4, $g(t|H_0)$ is the probability density of the test statistic, t , under the as-
 1815 sumption of the hypothesis, H_0 . In the event of a discrepancy between the expected and
 1816 observed results, it is desirable to be able to quantify the size of a discrepancy, which is
 1817 done using the significance, Z . This significance is defined such that a result which is Z
 1818 standard deviations from the mean of a Gaussian distribution has an integral equal to the
 1819 p -value.

1820

1821 The test statistic used for the purposes of setting limits on New Physics signals is the
 1822 profile log likelihood ratio, shown in Equation 5.5.5.

$$t_{\mu_{\text{sig}}} = -2\log\left(\frac{L(\mu_{\text{sig}}, \theta)}{L(\mu_{\text{sig}}, \hat{\theta})}\right) \quad (5.5.5)$$

1823 In Equation 5.5.5, L is the likelihood function defined in Equation 5.5.2, where the denomi-
 1824 nator has parameter choices such that the likelihood is maximised, while the numerator has
 1825 parameter choices that maximise the likelihood for the specific signal hypothesis under test.

1826

1827 In the context of searches for New Physics, the p -value can be used to claim a discov-
 1828 ery of New Physics, or exclude a given signal hypothesis. To claim the discovery of New
 1829 Physics, one must reject the hypothesis that only the SM background contributes to the
 1830 observed result to a level of $Z = 5\sigma$, corresponding to $p < 2.87 \times 10^{-7}$. The requirements
 1831 to exclude a signal hypothesis are less stringent, requiring the rejection of the SM back-
 1832 ground plus BSM signal hypothesis with values of $p < 0.05$, corresponding to $Z = 1.64$.
 1833 This exclusion limit correspondes to a 95% confidence limit.

1834

1835 One issue with using the p -value as the metric by which exclusion is performed is the
 1836 case where the rates of the BSM process are small enough such that the SM-only and
 1837 SM plus BSM signal distributions are very similar. In the case where an analysis has low
 1838 sensivity to a particular signal hypothesis, or where there is a downwards fluctuation of
 1839 data, the signal hypothesis can be rejected. To circumvent this, the CL_s method [52] was
 1840 developed, where the CL_s is defined as shown in Equation 5.5.6.

$$CL_s = \frac{p_1}{1 - p_0} = \frac{\int_{t_{\text{obs}}}^{+\infty} g(t|H_1)dt}{1 - \int_0^{t_{\text{obs}}} g(t|H_0)dt} \quad (5.5.6)$$

1841 In Equation 5.5.6, p_1 corresponds to the p -value that the alternate hypothesis, H_1 , is at
 1842 least as incompatible with H_0 as the observed result, while p_0 corresponds to the p -value
 1843 that the observed result is compatible with the null hypothesis, H_0 .

1844 Background-only fit

1845 The background-only fit is independent of any signal model assumptions, including only
 1846 SM background MC in the fit. In this scenario, μ_{sig} is set equal to 0. This fit type includes
 1847 only the CRs in the fit, and hence is not affected by the observed events in the SRs. The
 1848 purpose of this fit is to estimate the background yields in the SRs and VRs in a signal-
 1849 agnostic way, under the assumption that the CRs have negligible signal contamination.
 1850 Additionally, the results of the background-only fit can be used to test the sensitivity of a

1851 given analysis to a different signal than the one under study using the p -value hypothesis
1852 test previously described.

1853 **Model-dependent fit**

1854 The model-dependent fit regime includes background events and a specific signal model,
1855 fitting all processes together in both the CRs and SRs, including a signal strength param-
1856 eter μ_{sig} . The signal is included in *all* regions, to allow any signal contamination in the
1857 CRs to be correctly accounted for when calculating the background normalisation factors,
1858 μ_p . The model-dependent fit is performed on every signal point generated, such that the
1859 entire phase space of signal parameters is probed.

1860 **Model-independent fit**

1861 The model-independent fit is used to set limits on any potential BSM process present in
1862 the SRs. This fit includes both the CRs and SRs, but does not include a signal model or
1863 allow signal contamination in the CRs. In this fit regime, the SRs are implemented as an
1864 inclusive, single-bin region. The result of this fit is used to set upper limits on the visible
1865 cross-section, σ_{vis} , of a generic BSM process.

1866

Part II

1867

Searches for New Physics in Run-2

1868

ATLAS data

1869 Chapter 6

1870 Searches for $\tilde{\chi}_1^\pm \tilde{\chi}_2^0$ pair-production

1871 This Chapter presents an overview of searches for the pair-production of a chargino, $\tilde{\chi}_1^\pm$ and
1872 next-to-lightest neutralino, $\tilde{\chi}_2^0$, performed during the Run-2 period of data-taking. This
1873 Chapter focuses mainly on an analysis undertaken using data taken in 2015-2016, totalling
1874 36.1fb^{-1} . Later in this Chapter, the results of an analysis using the full Run-2 dataset of
1875 139fb^{-1} is presented, along with additional studies using machine learning to improve the
1876 sensitivity to the signal. Chapter 8 presents sensitivity studies for this signal at the High-
1877 Luminosity LHC, using a dataset of 3000fb^{-1} collected at $\sqrt{s} = 14$ TeV. The results of
1878 these analyses are interpreted in the context of a simplified SUSY model **INSERT REF**,
1879 in which the $\tilde{\chi}_1^\pm$ and $\tilde{\chi}_2^0$ are unstable and each decay to the lightest neutralino, $\tilde{\chi}_1^0$, via a
1880 SM W boson and Higgs boson. The Higgs boson in this process, h , is the lightest CP-even
1881 Higgs from the extended SUSY Higgs sector, and is assumed to be a SM-like Higgs boson,
1882 with $m_h = 125$ GeV and with the branching fraction of $\text{BR}(h \rightarrow b\bar{b}) = 58\%$. The final
1883 state of interest in this Chapter, and in Chapter 8, contains a single electron or muon
1884 from the decay of the W boson, two b -tagged jets from the decay of the Higgs boson, and
1885 E_T^{miss} from the neutrino and the two $\tilde{\chi}_1^0$. The $h \rightarrow b\bar{b}$ decay is the most frequent decay of
1886 the Higgs boson, with a branching fraction of 58%, and therefore this channel is expected
1887 to have far higher signal yields than channels targeting other decay modes of h . A diagram
1888 of the signal process relevant for this Chapter is shown in Figure 6.1.

1889

1890 A search for this process was undertaken in Run 1 using 20.3fb^{-1} taken at $\sqrt{s} = 8$ TeV in
1891 this final state, as well as the dilepton, trilepton and diphoton final states. 95% confidence
1892 limits were set on this signal, excluding the process upto $\tilde{\chi}_1^\pm/\tilde{\chi}_2^0$ masses of around 275 GeV
1893 for a massless $\tilde{\chi}_1^0$. The results for all four channels, as well as the statistical combination,
1894 are shown in Figure 6.2.

1895

1896 This Chapter first describes the simplified SUSY model used in both this Chapter and
1897 in Chapter ???. The event selection used to describe candidate SUSY events is then de-
1898 scribed, followed by the background estimation strategy, before presenting the results of

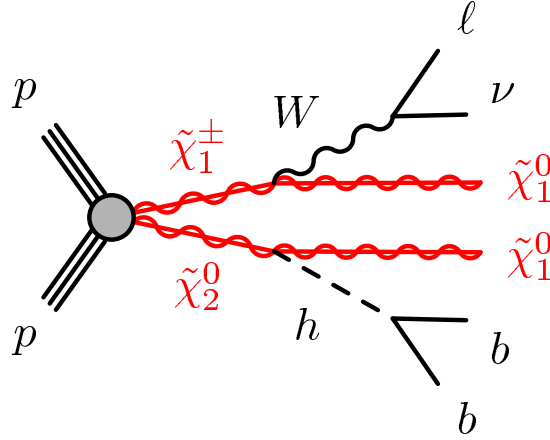


Figure 6.1: Diagram showing $\tilde{\chi}_1^\pm \tilde{\chi}_2^0$ pair-production, with the chargino and neutralino decaying via a SM W boson and a Higgs, respectively. The assumptions made in simplified SUSY model are summarised in Table 6.1.

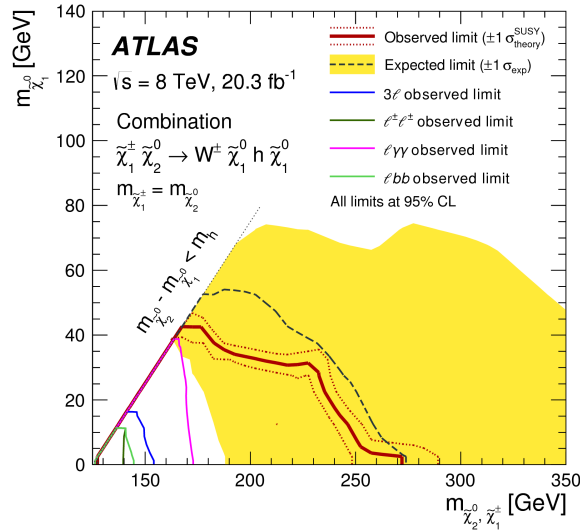


Figure 6.2: A plot showing the four exclusion limits obtained from searches for $\tilde{\chi}_1^\pm \tilde{\chi}_2^0$ pair-production during the Run-1 data-taking period.

1899 this analysis.

1900 6.1 SUSY signal model

1901 As discussed in Chapter 1, SUSY provides resolution to the hierarchy problem through
 1902 the introduction of fermionic (bosonic) superpartners to the SM bosons (fermions). As
 1903 of the time of writing, there has been no experimental observation of these superpartners
 1904 and hence it is concluded SUSY is a broken symmetry, such that the superpartners have
 1905 different masses to their SM partners. If the masses of the squarks and gluinos, the super-
 1906 partners to the SM quarks and gluon, are much heavier than charginos and neutralinos, the

1907 electroweak production of SUSY particles is expected to dominate at the LHC. The mass
 1908 eigenstates of the charginos, $\tilde{\chi}_i^\pm$ where $i = 1, 2$, and neutralinos, $\tilde{\chi}_j^0$ where $j = 1, 2, 3, 4$, are
 1909 ordered from smallest to largest mass. In this Thesis, the lightest supersymmetric particle
 1910 (LSP) corresponds to the lightest neutralino, $\tilde{\chi}_1^0$, and is a DM candidate in the case where
 1911 R-parity is conserved, meaning the LSP is stable and weakly-interacting.

1912

1913 SUSY models have an enormous parameter space with over 100 free parameters, such
 1914 as the sparticle masses and couplings. Simplified models vastly reduce the number of free
 1915 parameters, such that a single analysis can be sensitive to a large region of the SUSY model
 1916 phase space. As previously mentioned, it is assumed the Higgs boson present in the decay
 1917 of the $\tilde{\chi}_2^0$ is SM-like, such that it has a mass of $m_h = 125$ GeV and $\text{BR}(h \rightarrow b\bar{b}) = 0.58$.
 1918 It is assumed that the branching ratios of the $\tilde{\chi}_1^\pm \rightarrow W\tilde{\chi}_1^0$ and $\tilde{\chi}_2^0 \rightarrow h\tilde{\chi}_1^0$ are both 100%.
 1919 Therefore, the only free parameters of the simplified model used in both this Chapter and
 1920 Chapter 8 are $m(\tilde{\chi}_1^\pm)$, $m(\tilde{\chi}_2^0)$ and $m(\tilde{\chi}_1^0)$. The further assumption that the $\tilde{\chi}_1^\pm$ and $\tilde{\chi}_2^0$
 1921 are degenerate in mass reduces the number of free parameters to just two; $m(\tilde{\chi}_1^\pm/\tilde{\chi}_2^0)$ and
 1922 $m(\tilde{\chi}_1^0)$. The simplified model assumptions are listed again for reference in Table 6.1.

Model parameter	Assumption
$\text{BR}(\tilde{\chi}_1^\pm \rightarrow W\tilde{\chi}_1^0)$	100%
$\text{BR}(\tilde{\chi}_2^0 \rightarrow h\tilde{\chi}_1^0)$	100%
$\text{BR}(h \rightarrow b\bar{b})$	58%
m_h	125 GeV
Sparticle masses	$m(\tilde{\chi}_1^\pm) = m(\tilde{\chi}_2^0)$

Table 6.1: A table summarising the model parameter assumptions for the simplified SUSY model used in this Chapter and Chapter 8.

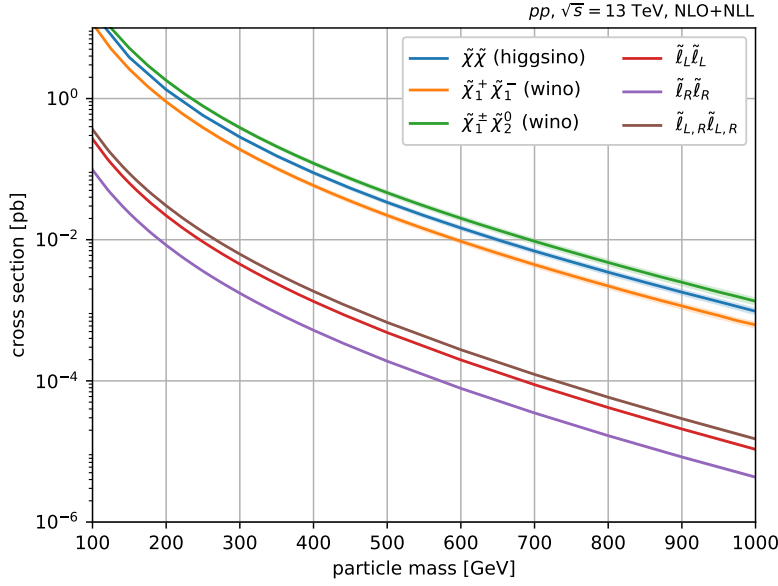


Figure 6.3

6.2 Event selection

Candidate events for this analyses are first selected using a set of loose, preliminary selections, known as ‘preselection’. The preselection cuts, summarised in Table 6.2, target events with an event topology which matches that of the signal, in particular events with a single lepton, two b -jets and E_T^{miss} . All events are required to have exactly 1 electron or muon passing the signal lepton requirements, with any extra baseline leptons being vetoed. Events are required to have either 2 or 3 jets with transverse momentum greater than 25 GeV, and exactly two jets being b -tagged using the MV2c10 algorithm. The b -tagged jets are also required to have transverse momentum greater than 25 GeV. Some data/MC discrepancies were seen at low m_{bb} and m_T , and hence lower bound requirements on these variables are placed. Finally, all events are required to pass one of the E_T^{miss} triggers detailed in Section 3.1.

6.3 Background estimation

The $t\bar{t}$, single top and W +jets backgrounds are the most dominant backgrounds in the three SR bins. Each of these major backgrounds have corresponding CRs defined in which to evaluate the process-specific normalisations, μ_{process} . The $t\bar{t}$ CR is defined with 3 m_T bins, matching the m_T ranges of the 3 SR bins, named $\text{CR}(t\bar{t})\text{-LM}$, $\text{CR}(t\bar{t})\text{-MM}$ and $\text{CR}(t\bar{t})\text{-HM}$, respectively. The top-pair CRs invert the selection on the m_{CT} variable described in Chapter 5 to target the production of a pair of top quarks, while the selection on m_{bb} is inverted as the distribution is not expected to peak around the Higgs masses. A single-bin

Variable	Selection
N_ℓ^{baseline}	= 1
N_ℓ^{signal}	= 1
$p_T(\ell_1)$	> 27 GeV
N_{jet}	= 2 or 3
$p_T(\text{jet})$	> 25 GeV
$N_{b\text{-jet}}$	= 2
$p_T(b - \text{jet})$	> 25 GeV
m_T	> 40 GeV
m_{bb}	> 50 GeV

Table 6.2: A summary of the preliminary event selection used in the 36.1fb^{-1} search for $\tilde{\chi}_1^\pm \tilde{\chi}_2^0$ pair-production.

	SRLM	SRMM	SRHM
m_{bb}	$\in [105, 135]$ GeV		
m_{CT}	> 160 GeV		
E_T^{miss}	> 200 GeV		
m_T	$\in [100, 140]$ GeV	$\in [140, 200]$ GeV	> 200 GeV

Table 6.3: A summary of the signal region selections used in the 36.1fb^{-1} search for $\tilde{\chi}_1^\pm \tilde{\chi}_2^0$ pair-production.

1943 CR for the single top background, $\text{CR}(t)$, and a single-bin CR for the W +jets background,
 1944 $\text{CR}(W)$, are also defined. The single-top CR is defined by requiring the m_{bb} is large to
 1945 target the presence of b -quarks coming from the decay of a top quark and the initial state
 1946 gluon splitting. Finally, the W +jets CR exploits the m_T variable, as described in Chapter
 1947 5, to target the decay of a single leptonic W boson, while rejecting the $t\bar{t}$ background. The
 1948 full definitions of these regions are given in Table 6.4.

Variable	Region				
	$\text{CR}(t\bar{t}\text{-LM})$	$\text{CR}(t\bar{t}\text{-MM})$	$\text{CR}(t\bar{t}\text{-HM})$	$\text{CR}(t)$	$\text{CR}(W)$
m_T [GeV]	$\in [100, 140]$	$\in [140, 200]$	> 200	> 100	$\in [40, 100]$
m_{CT} [GeV]	< 160	< 160	< 160	> 160	> 160
m_{bb} [GeV]	$\notin [105, 135]$	$\notin [105, 135]$	$\notin [105, 135]$	> 195	< 80
E_T^{miss} [GeV]	> 200	> 200	> 200	> 200	> 200

Table 6.4

1949 6 VRs are defined, 3 targeting m_{bb} values in a window around the Higgs peak, $m_{\text{bb}} \in$
 1950 $[105, 135]$ GeV, with 3 further VRs targeting m_{bb} values in the sideband region. The

former VRs are referred to as ‘on-peak’ regions, denoted by VR_{on} , while the latter are referred to as ‘off-peak’ regions and are denoted by VR_{off} . Each set of VRs mirrors the SR binning in the m_T variable. The explicit VR definitions are given in Table 6.5.

Variable	Region					
	$\text{VR}_{\text{on}}(\text{LM})$	$\text{VR}_{\text{on}}(\text{MM})$	$\text{VR}_{\text{on}}(\text{HM})$	$\text{VR}_{\text{off}}(\text{LM})$	$\text{VR}_{\text{off}}(\text{MM})$	$\text{VR}_{\text{off}}(\text{HM})$
m_T [GeV]	$\in [100, 140]$	$\in [140, 200]$	> 200	$\in [100, 140]$	$\in [140, 200]$	> 200
m_{CT} [GeV]	< 160	< 160	< 160	> 160	> 160	> 160
m_{bb} [GeV]	$\in [105, 135]$	$\in [105, 135]$	$\in [105, 135]$	$< 95 \parallel \in [145, 195]$		
E_T^{miss} [GeV]	> 200	> 200	> 200	> 180	> 180	> 180

Table 6.5

1953

1954 6.4 Systematic uncertainties

Three sources of uncertainty are considered in this analysis; statistical uncertainties, arising from the finite statistics in both data and the MC, experimental systematics and modelling systematics. Section 5.4 describes the experimental systematics evaluated in this analysis. Modelling uncertainties are evaluated using the transfer factor prescription described in Section **REF**.

Source	Size (%)
	Modelling systematics
$t\bar{t}$ modelling	
Single top modelling	
	Experimental systematics
JES	
JER	
b -tagging	

Table 6.6: Table showing a summary of the dominant experimental and modelling uncertainties.

1959

1960 6.5 Results

1961 Background-only fit results

The results of the background-only fit in the CRs, VRs and SRs for the $1\ell + b\bar{b} + E_T^{\text{miss}}$ channel are shown in Tables 6.7, **REF** and 6.8, respectively. As explained in Chapter 5.5, the

1963

1964 background-only fit configuration uses only the CRs to normalise the dominant back-
 1965 grounds, in this case $t\bar{t}$, single top and W +jets. The $t\bar{t}$ background has 3 separate nor-
 1966 malisation factors, one for each m_T bin, such that data/MC differences in each region can
 1967 be corrected independently of each other. The results of the background-only fit are then
 1968 extrapolated to the VRs and SRs, such that an estimate of the backgrounds in the SR
 1969 can be derived without bias from any potential excesses in the SRs, or assumptions on the
 1970 signal model itself. Excellent data/MC agreement is observed in the CRs and most of the
 1971 VRs. In $VR_{\text{on-HM}}$ and SR_{MM} , there are excesses between $1.5 - 2\sigma$.

1972

1973 The normalisation factors derived for the $t\bar{t}$, single top and W +jets backgrounds using
 1974 the background-only fit configuration are given in Table 6.9. All values are compatible
 with unity, with the

Control regions	CR($t\bar{t}$)-LM	CR($t\bar{t}$)-MM	CR($t\bar{t}$)-HM	CR(W)	CR(t)
Observed events	192	359	1115	72	65
Fitted bkg events	192 ± 14	359 ± 19	1115 ± 34	72 ± 9	65 ± 8
$t\bar{t}$	147 ± 33	325 ± 32	1020 ± 90	15 ± 14	20_{-20}^{+23}
Single top	28 ± 25	22_{-22}^{+24}	60_{-60}^{+70}	4_{-4}^{+6}	33 ± 25
W +jets	16 ± 7	7.3 ± 2.7	25 ± 11	51 ± 17	8 ± 4
$t\bar{t}V$	1.16 ± 0.20	2.8 ± 0.4	6.9 ± 1.1	0.079 ± 0.022	3.2 ± 0.6
Diboson	0.57 ± 0.24	0.92 ± 0.29	1.3 ± 0.4	2.1 ± 1.1	0.84 ± 0.28
Others	0.125 ± 0.032	0.20 ± 0.06	1.9 ± 0.5	0.24 ± 0.17	0.10 ± 0.04

Table 6.7

1975

Signal regions	SRLM	SRMM	SRHM
Observed events	6	7	5
Fitted bkg events	5.7 ± 2.3	2.8 ± 1.0	4.6 ± 1.2
$t\bar{t}$	3.4 ± 2.9	1.4 ± 1.0	1.1 ± 0.6
Single top (Wt)	$1.4^{+1.4}_{-1.4}$	$0.8^{+0.9}_{-0.8}$	1.2 ± 1.1
W + jets	0.6 ± 0.4	0.20 ± 0.11	1.6 ± 0.6
$t\bar{t}V$	0.10 ± 0.04	0.32 ± 0.09	0.54 ± 0.14
Diboson	$0.12^{+0.15}_{-0.12}$	0.05 ± 0.03	0.08 ± 0.02
Others	0.10 ± 0.05	0.03 ± 0.01	0.04 ± 0.02

Table 6.8

1ℓ analysis	
$\mu(t\bar{t}\text{-LM})$	1.02 ± 0.14
$\mu(t\bar{t}\text{-MM})$	1.15 ± 0.13
$\mu(t\bar{t}\text{-HM})$	$0.89^{+0.21}_{-0.20}$
$\mu(W)$	1.40 ± 0.5
$\mu(t)$	$1.10^{+0.7}_{-1.1}$

Table 6.9

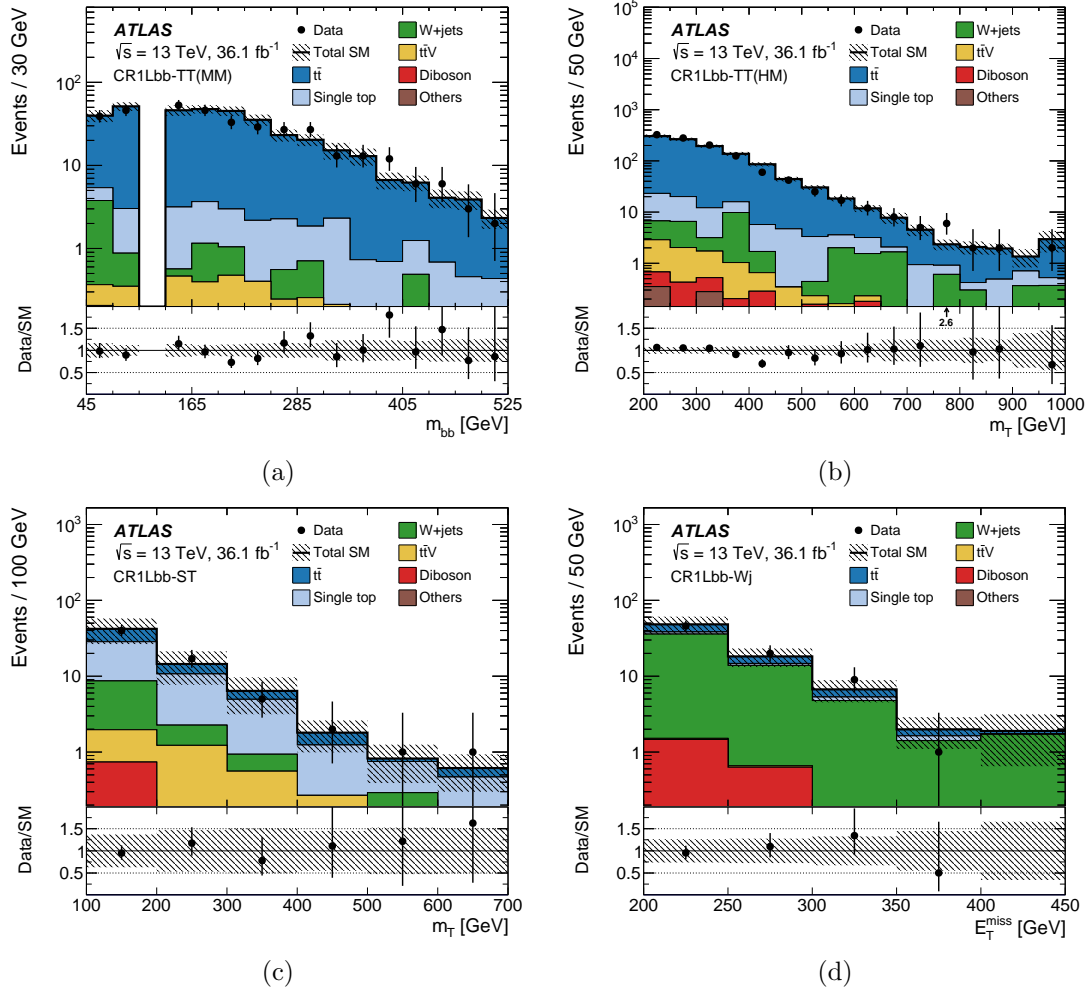


Figure 6.4

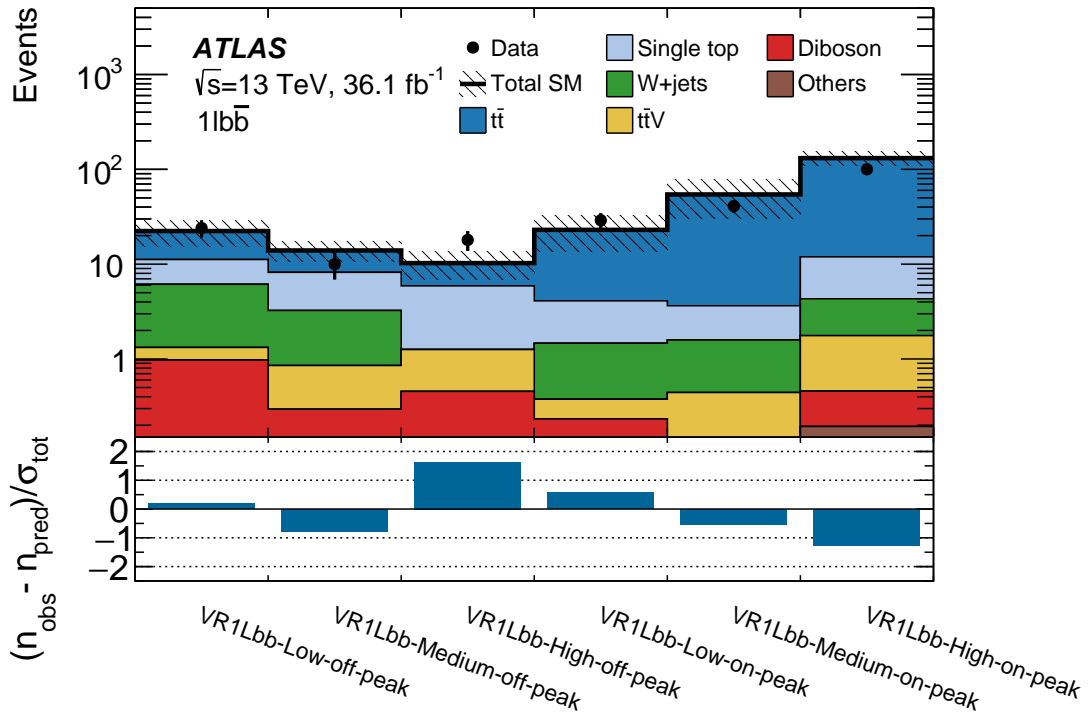


Figure 6.5

1976 **Model-dependent results**

1977 As shown in the background-only fit results presented previously, no significant excesses are
 1978 observed in the SRs. In this case, model-dependent exclusion limits are set on $\tilde{\chi}_1^\pm \tilde{\chi}_2^0$ pair-
 1979 production decaying via the Wh signature to the $1\ell + b\bar{b} + E_T^{\text{miss}}$ final state. As described in
 1980 Section 5.5, the model-dependent fit configuration uses both the CRs and SRs to set 95%
 1981 confidence limits on the presence of a given signal model. The model-dependent exclusion
 1982 limits for the analysis using a dataset of 36.1fb^{-1} collected at $\sqrt{s} = 13$ TeV is shown in
 Figure 6.6, excluding $\tilde{\chi}_1^\pm/\tilde{\chi}_2^0$ masses upto 550 GeV for a massless $\tilde{\chi}_1^0$.

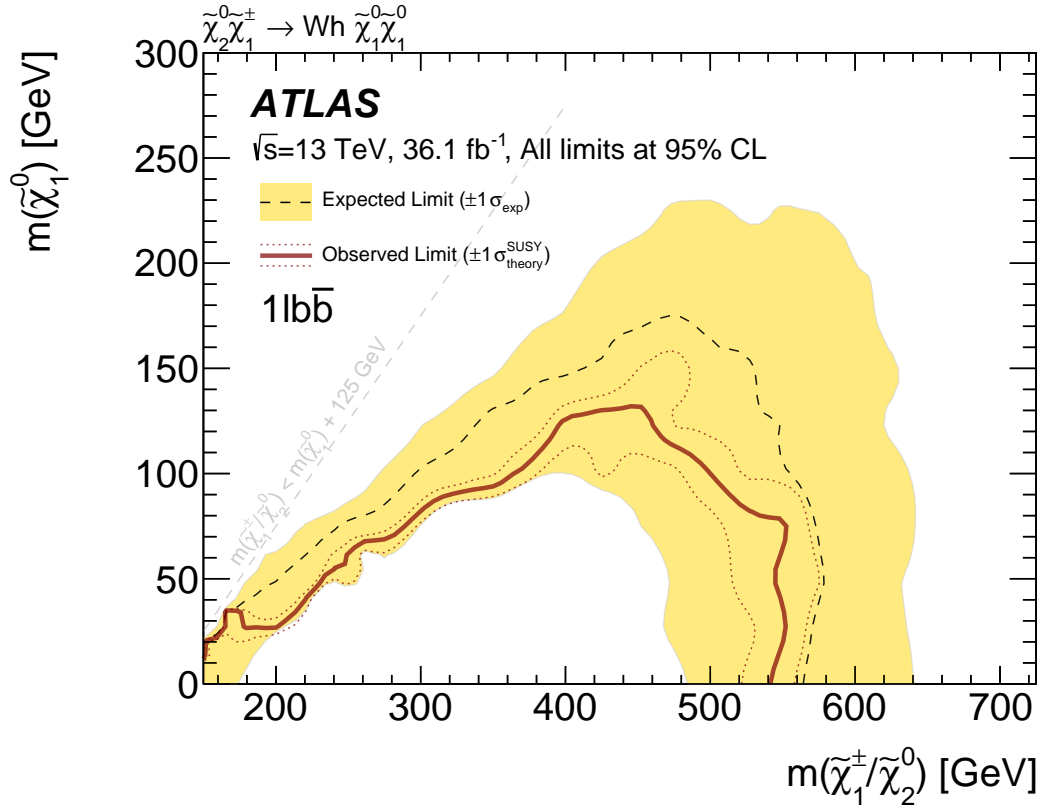


Figure 6.6

1983

1984 **Model-independent limits**

1985 In addition to the model-dependent fit, 95% confidence limits are set on a generic BSM
 1986 process using the model-independent fit strategy detailed in Section ???. A visible cross-
 1987 section, σ_{vis} , is derived which represents the product of the signal selection efficiency, ϵ , the
 1988 detector acceptance, A and the production cross-section for the BSM process, σ_{BSM} . The
 1989 model-independent limits on σ_{vis} derived using the SRs defined early are shown in Table
 1990 6.10, as well as limits on the expected and observed number of signal events.

	σ_{vis} [fb]	S_{obs}^{95}	S_{exp}^{95}	p_0 -value
SRLM	0.23	8.3	$8.0_{-2.2}^{+3.3}$	0.46
SRMM	0.28	10.0	$5.6_{-1.7}^{+2.9}$	0.04
SRHM	0.18	6.4	$6.1_{-1.9}^{+3.1}$	0.44

Table 6.10: From left to right, the observed 95% CL upper limits on the visible cross-sections σ_{vis} , the observed (S_{obs}^{95}) and expected (S_{exp}^{95}) 95% CL upper limits on the number of signal events with $\pm 1\sigma$ excursions of the expectation, and the discovery p -value (p_0), truncated at 0.5.

1991 **6.6 Studies with 139fb^{-1}**

1992 **ML studies**

1993 **Reoptimised analysis results**

1994 Chapter 7

1995 Search for Dark Matter produced 1996 in association with a Top Quark

1997 This Chapter presents a search for the production of Dark Matter (DM) in association
1998 with a single top quark, also referred to as DMt , using the full Run-2 dataset collected by
1999 ATLAS of 139fb^{-1} . The results of the analysis are interpreted in the context of a simpli-
2000 fied model of DM production, where the DM is coupled to an extended SM Higgs sector
2001 (2HDM) by a massive, spin-0, pseudoscalar mediator, a .

2002

2003 This Chapter focuses mainly on the $tW+E_T^{\text{miss}}$ signature with a single lepton final state.
2004 A complementary analysis of the two lepton final state was also performed, as documented
2005 in [53], and will not be detailed here. In addition to the $tW+E_T^{\text{miss}}$ signature, it was found
2006 that the sensitivity of these analyses to DM produced in association with a $t\bar{t}$ pair, referred
2007 to as $DMt\bar{t}$, was non-negligible. The overall sensitivity of this analysis to the $DMt+t\bar{t}$ signal
2008 was evaluated and is detailed in the fit results. Finally, in addition to the independent anal-
2009 yses of the single- and two-lepton final states, both channels were statistically-combined
2010 to increase the sensitivity to the DMt and $DMt+t\bar{t}$ signals.

2011

2012 This Chapter begins with a description of the simplified DM model used to interpret the
2013 results, focusing on the experimental signature of interest, the $tW+E_T^{\text{miss}}$ signature. The
2014 SR optimisation and selections, as well as the background estimation strategy are doc-
2015 umented, before finally presenting the analysis results. Firstly, the background-only fit
2016 results in the CRs and SRs are presented, before presenting the model-dependent and
2017 model-independent results.

2018 7.1 2HDM+ a signal model

2019 As described in Section ??, there is a strong motivation for performing searches for the pro-
2020 duction of Dark Matter (DM) at the LHC. Many searches for DM production have already

2021 been carried out using ATLAS data, with the results of the searches being interpreted
 2022 in the context of the LHC DM simplified models, as described in [54–56]. These models
 2023 introduce a new, spin-0 pseudoscalar mediator which couples the SM to DM. However,
 2024 such models have a limited phenomenology [57], and examples of these models violating
 2025 gauge invariance and unitarity have also studied [58]. Therefore, while the DM simplified
 2026 models serve as an excellent benchmark in searches for DM production, a more complete
 2027 and theoretically-consistent description of DM production is needed.

2028

2029 The simplest extension to the LHC DM simplified models adds a second Higgs doublet
 2030 to the SM (2HDM). This enables the mixing of the spin-0 mediator with the SM, while
 2031 also not violating constraints set on the SM Higgs couplings. The particular model of
 2032 interest in this thesis is the case of a 2HDM model, with an additional pseudoscalar medi-
 2033 ator, a . For this model, the $tW + E_T^{\text{miss}}$ signature has not been previously studied, but has
 2034 been shown to have promising potential in sensitivity studies [57]. The dominant Feynman
 2035 diagrams for this signature are shown in Figure 7.1. The diagram shown in Figure 7.1a
 2036 is present in the LHC DM simplified models, while the diagram shown in Figure 7.1b
 2037 is only present in the 2HDM+ a model. The latter diagram gives an approximate order-of-
 2038 magnitude enhancement to the $pp \rightarrow tW\chi\chi$ cross-section through the on-shell production
 2039 of the charged Higgs, H^- . The additional diagrams from the 2HDM+ a model also interfere
 2040 destructively with the diagrams from the LHC DM simplified model, restoring unitarity.

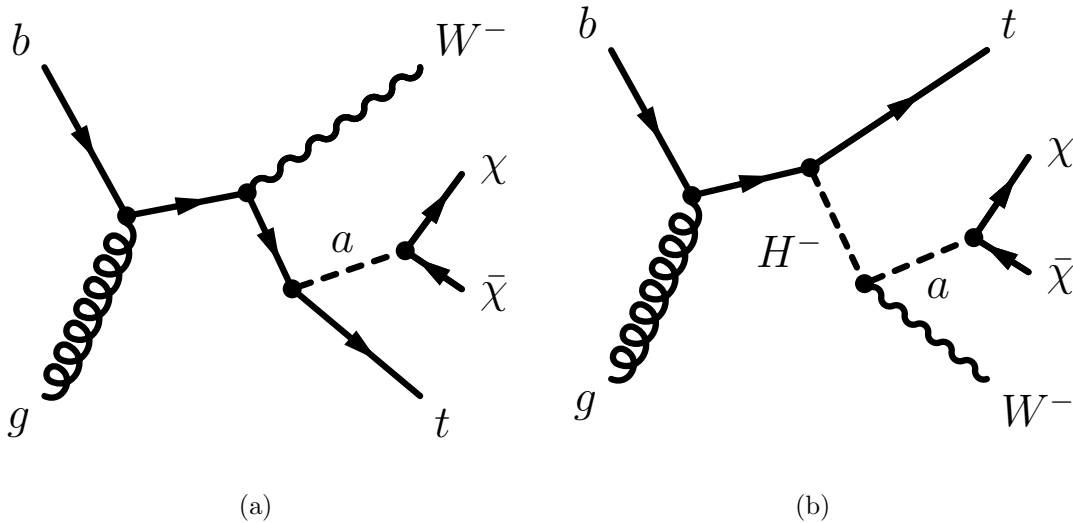


Figure 7.1: Feynman diagram for dark matter production in the Wt channel, in the context of a 2HDM+ a model. This chapter documents studies done in the single lepton channel, where one of the W bosons in the event decays leptonically.

2041 In addition to the $tW + E_T^{\text{miss}}$ signature, the analysis described in the later sections of
 2042 this Chapter is also sensitive to the $t\bar{t} + E_T^{\text{miss}}$ signature of associated DM production. A
 2043 rescaling procedure is applied to the $DMt\bar{t}$ process, which is generated, using the DMSimp

2044 framework [59], in the context of a simplified DM production model in which the pseu-
 2045 doscalar mediator a directly couples to the SM. The Feynman diagram for this process
 2046 is shown in Figure 7.2. The predictions of this simplified model are rescaled to correctly
 2047 model the prediction using the 2HDM+ a model using the procedure described in [60],
 2048 which also includes contributions from the heavy pseudoscalar A .

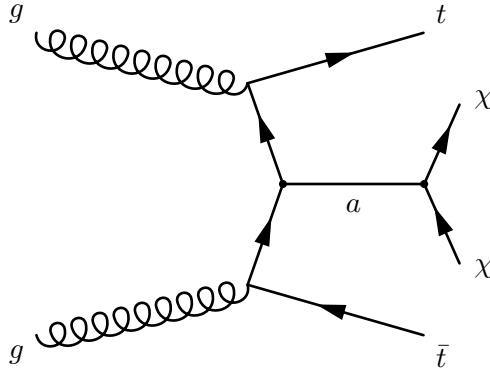


Figure 7.2: Diagram of DM produced in association with a $t\bar{t}$ pair, in the context of the 2HDM+ a model under study in this Chapter. The sensitivity of the analysis described later in this Chapter to this signal is shown in Section 7.5.

2049 The model under study in this Chapter is described in detail in [60], but an overview
 2050 of the most prominent parameters and the choices assigned is given here. As previously
 2051 described in Section ??, models with a second Higgs doublet comprise five physical states;
 2052 the CP-even scalars h and H , the CP-odd pseudoscalar A , and two charged Higgs bosons
 2053 H^\pm . The coupling of the extended Higgs sector is of Type-II, such that one Higgs doublet
 2054 couples to up-type fermions while the other couples to down-type fermions. The mixing in
 2055 the extended Higgs sector is specified by three mixing angles, α , θ and β . α represents the
 2056 mixing angle of the two CP-even states, θ represents the mixing of the CP-odd states, and
 2057 $\tan\beta$ represents the ratio of the VEVs of the two Higgs doublets. The *alignment limit* is
 2058 assumed, where $\cos(\beta - \alpha) = 0$, such that h can be identified with the SM Higgs boson. To
 2059 enhance the sensitivity to this model, it is assumed that there is maximal mixing between
 2060 the Higgs sector and the mediator, A and a , and as such it is assumed that $\sin\theta = 1/\sqrt{2}$.
 2061 As described in [60], it is assumed the masses of the CP-even neutral Higgs, the CP-odd
 2062 Higgs and the charged Higgs states are degenerate, and the mass of the DM, m_χ is set
 2063 equal to 10 GeV. Finally, the DM coupling to a is set equal to unity, $y_\chi = 1$. Therefore,
 2064 there are three free parameters; $\tan\beta$, m_{H^\pm} and m_a . In order to set model-dependent
 2065 limits on this process, two planes are defined to cover the largest possible region of the
 2066 available model phase space. The first is a scan in the m_a, m_{H^\pm} plane, assuming $\tan\beta = 1$,
 2067 while the second plane is a scan in the $m_{H^\pm}, \tan\beta$ plane, assuming $m_a = 250$ GeV. The
 2068 cross-section dependence on $\tan\beta$ for the DM t and DM $t\bar{t}$ processes is shown in Figure 7.3,
 2069 with $m_a = 250$ GeV and $m_{H^\pm} = 600$ GeV. As seen, the cross-section for the DM $t\bar{t}$ process
 2070 has a $1/\tan^2\beta$ dependence, while the DM t has a more complex dependence on the value of

2071 $\tan\beta$. A summary of the model parameter choices is given in Table 7.1.

Fixed parameters	Assumption
$\sin\theta$	$= 1/\sqrt{2}$
$\cos(\beta - \alpha)$	$= 0$
m_h	$= 125$ GeV
$m_H, m_A, m_{H\pm}$	Degenerate
m_χ	$= 10$ GeV
y_χ	$= 1$

Table 7.1: A table summarising the model parameter assumptions for the simplified 2HDM+ a model of DM production as described in [60].

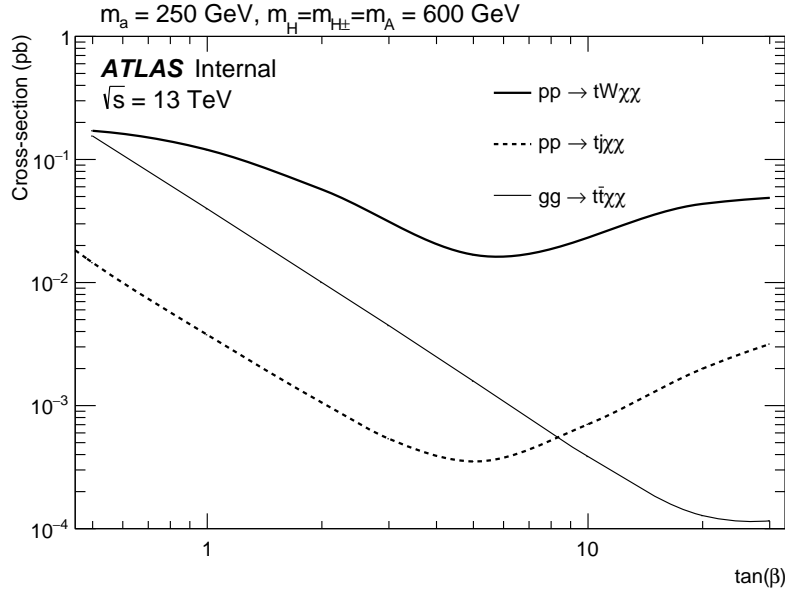


Figure 7.3: Diagram showing the production cross-section of DM produced in association with tW , t and $t\bar{t}$. The associated $t\bar{t}$ production cross-section is proportional to $1/\tan^2\beta$ as described in [61].

2072 7.2 Event selection

2073 The event selection for this analysis begins with a set of preliminary, loose selections, known
 2074 as ‘preselection’. The preselection cuts aim to select events matching the signal topology,
 2075 while rejecting events with different topologies. All events are required to have exactly
 2076 1 electron or muon in the final state, with any additional reconstructed leptons failing
 2077 the ‘signal’ lepton requirements being rejected. At least three jets are required, to target
 2078 events with at least one hadronically-decaying W boson, and at least one b -tagged jet is

2079 required to select events with a top quark. To minimise the background contribution from
 2080 $t\bar{t}$, events with a second b -tagged jet required it has a transverse momentum $p_T(b_2) < 50$
 2081 GeV. The jets and E_T^{miss} must have an angular separation of at least 0.5 rad, to reject
 2082 events which have mismeasured jets. All events are required to pass the event cleaning
 2083 procedure described in Section 4.7, as well as passing one of the E_T^{miss} triggers as described
 2084 in Section 3.1. In order to ensure a constant E_T^{miss} trigger efficiency, all events are required
 2085 to have $E_T^{\text{miss}} > 250$ GeV. The full preselection requirements for this analysis are defined
 2086 in Table 7.2. The definitions for the objects used in this analysis are described in Chapter
 2087 4.

Variable	Selection
N_ℓ^{baseline}	= 1
N_ℓ^{signal}	= 1
$p_T(\ell_1)$	> 30 GeV
N_{jet}	≥ 3
$p_T(\text{jet})$	> 30 GeV
$N_{b\text{-jet}}$	≥ 1
$p_T(b\text{-jet})$	> 50 GeV
E_T^{miss}	> 250 GeV
m_T	> 30 GeV
$ \Delta\phi $	> 0.5 [rad]

Table 7.2: Preliminary selections used for the $tW + E_T^{\text{miss}}$ analysis. All events are also required to pass the E_T^{miss} trigger, and the event cleaning requirements detailed in Section 4.7. The object definitions used are detailed in Chapter 4.

2088 At the preselection-level, the dominant backgrounds, estimated from MC-only, are $t\bar{t}$
 2089 (67%), W +jets (18%) and single top production (11%), where the percentages in parenthe-
 2090 sis represents the contribution of that process to the total background. Four key variables
 2091 were identified which enabled rejection of the backgrounds while maintaining a reasonably
 2092 high signal selection efficiency; E_T^{miss} , m_T , am_{T2} and m_W^{had} . These variables are defined in
 2093 Section 5.2. The am_{T2} , m_T and m_W^{had} variables formed the inputs to simultaneous adaptive
 2094 random grid search and genetic algorithms, as described in Section 5.3. The SR selections
 2095 are summarised in Table 7.3.

2096 7.3 Background estimation

2097 The major backgrounds in the E_T^{miss} bins of the SR vary, depending on bin, between $t\bar{t}$ and
 2098 W +jets, with smaller contributions from Wt -channel single top production, $t\bar{t} + V$ and
 2099 the diboson backgrounds. A single-bin CR for the $t\bar{t}$ background, $\text{CR}(t\bar{t})$ and a 2-bin CR
 2100 for the W +jets background, $\text{CR}(W)$, are defined. For the W +jets background, the CR is

Variable	Selection
$p_T(b_2)$	< 50 GeV
m_T	> 200 GeV
am_{T2}	> 220 GeV
m_W^{had}	> 60 GeV
E_T^{miss} [binned]	$\in [250, 300]$ GeV
	$\in [300, 400]$ GeV
	$\in [400, 500]$ GeV
	$\in [500, 600]$ GeV
	> 600 GeV

Table 7.3: A table of the SR definitions, based on the

2101 separated into 2 bins of lepton charge to exploit the charge asymmetry of W^\pm production.
 2102 The definitions of the CRs are given in Table 7.4.

Region	CR($t\bar{t}$)	CR(W)
N_ℓ^{signal}	= 1	
p_T^{b1}	> 50	
p_T^{b2}	> 50	< 50
E_T^{miss}	> 250	
am_{T2}	< 220	> 220
m_T	> 200	$\in [40, 100]$
m_W	–	< 60

Table 7.4: Control region definitions for the $tW + E_T^{\text{miss}}$ analysis. The W +jets CR is split into two bins of lepton charge, such that the W^\pm production charge asymmetry can be exploited.

2103 6 validation regions are defined which are in a region of kinematic phase space that is
 2104 between the CRs and SRs. Two $t\bar{t}$ VRs are defined in order to validate the extrapolation
 2105 of am_{T2} and m_W , while for the W +jets background, two VRs are defined to validate the
 2106 extrapolation of m_T and m_W . Each of the W +jets VRs is split into two bins of lepton
 2107 charge to mirror the CR definition. The VR definitions are explicitly defined in Table 7.5.

2108 7.4 Systematic uncertainties

2109 In addition to statistical uncertainties in the MC and on data, systematic uncertainties are
 2110 evaluated on all MC background and signal samples, from both experimental and modelling
 2111 sources. The experimental systematics considered are described in Section 5.4. The dom-
 2112 inant experimental systematics in the SRs are from the JES, JER and b -tagging efficiency

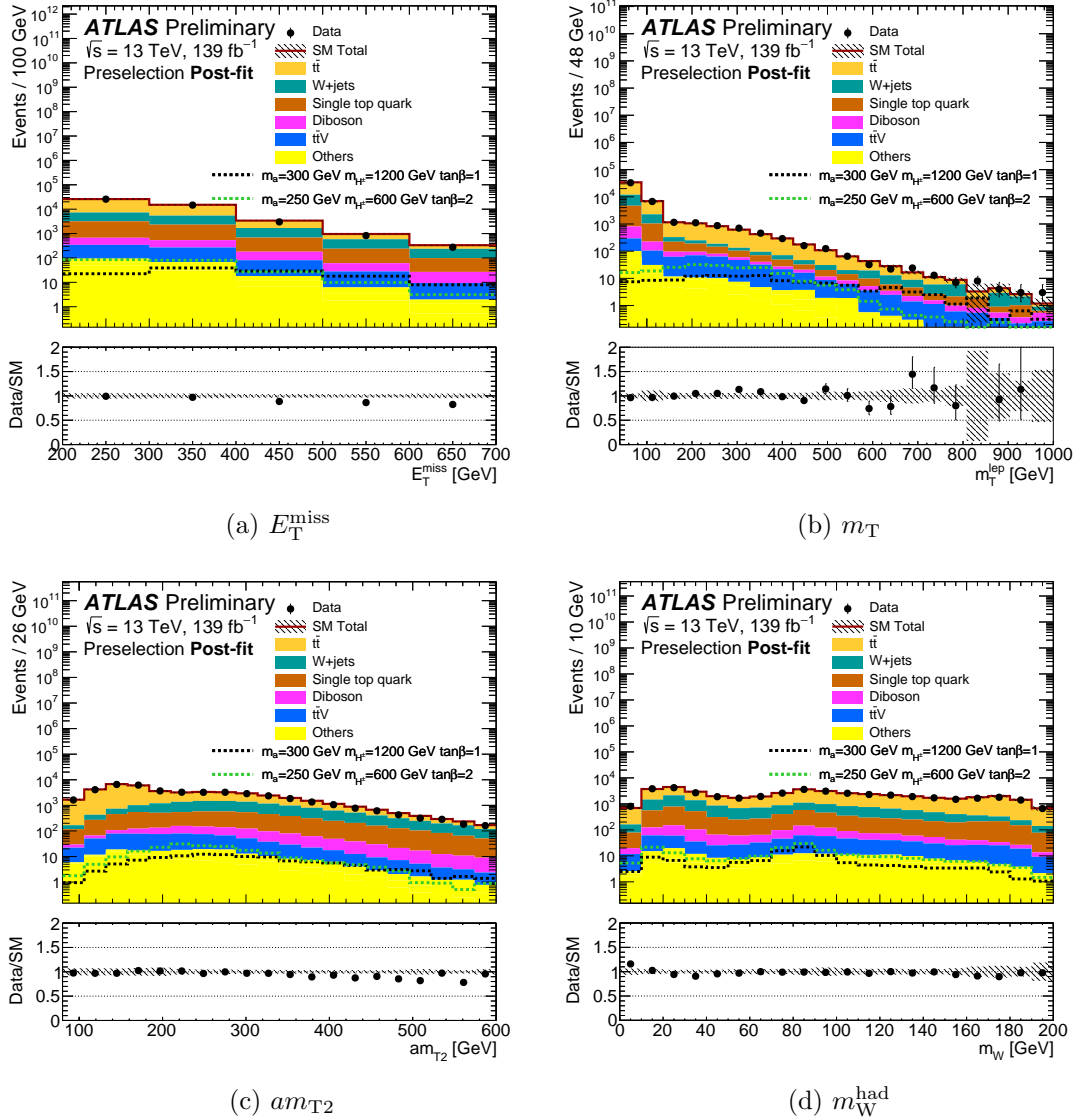


Figure 7.4: Post-fit plots of the key kinematic variables. The uncertainty band in the ratio plot contains only the MC statistical uncertainty and the experimental uncertainties.

2113 systematics. The modelling uncertainties on the $t\bar{t}$ and single top backgrounds are the dom-
 2114 inant modelling systematics in the SRs. The impact of the choice of the hard-scattering
 2115 generator for the $t\bar{t}$ and single-top backgrounds is evaluated by comparing the `Powheg-Box`
 2116 nominal prediction with `MadGraph5_aMC@NLO`, both interfaced to `Pythia8`. To assess the
 2117 impact of the PS and hadronisation modelling, the nominal `Powheg+Pythia8` configuration
 2118 is compared with the nominal hard-scatter generator configuration interfaced to `Herwig7`.
 2119 As previously described in Section ??, the uncertainty due to the modelling of the interfer-
 2120 ence between the $t\bar{t}$ and Wt processes is evaluated by comparing the DR and DS schemes,
 2121 with the derived uncertainty applied to the nominal Wt prediction. The uncertainty due to
 2122 the choice of renormalisation and factorisation scales, as well as the ISR and FSR param-

Region	VR1($t\bar{t}$)	VR2($t\bar{t}$)	VR1(W)	VR2(W)
N_ℓ^{signal}			= 1	
p_T^{b2}			< 50	
E_T^{miss}			> 250	
am_{T2}	< 220	> 220	> 220	> 220
m_T	> 200	> 200	$\in [40, 100]$	> 100
m_W	–	< 60	> 60	< 60

Table 7.5: Validation region definitions for the $tW + E_T^{\text{miss}}$ analysis. The W +jets VRs, like the CR, are each split into two bins of lepton charge.

eters are varied using internal weights in the nominal sample. Table 7.6 gives an overview of the size of the dominant systematics in this analysis.

Source	Size (%)
	Modelling systematics
$t\bar{t}$ modelling	
Single top modelling	
	Experimental systematics
JES	
JER	
b -tagging	

Table 7.6: Table showing a summary of the dominant experimental and modelling uncertainties.

2124

2125 7.5 Results

2126 Background-only fit results

2127 The background-only fit results in the CRs, VRs and SR bins for the single lepton channel
 2128 are shown in Tables 7.7, 7.8 and 7.9, respectively. In this configuration, only the CRs enter
 2129 the fit, allowing an estimate of the backgrounds in the VRs and SRs without any signal
 2130 assumptions. Generally, excellent data/MC agreement is observed in the CRs and VRs,
 2131 while in the SRs there are $\sim 1\sigma$ excesses in bins 0 and 1 and an $\sim 1\sigma$ underfluctuation of
 2132 data in bin 4.

2133

2134 The background normalisation factors for the $t\bar{t}$ and W +jets backgrounds, which are de-
 2135 rived in the CRs, are shown in Table 7.10. These show excellent compatibility with the
 2136 SM, agreeing with unity within 1σ .

2137

2138 Figures 7.5, 7.6 and 7.7 show the key kinematic variables for the CRs, VRs and SRs, re-
 2139 spectively, including background normalisation factors from the background-only fit. Good
 modelling is seen in these variables.

Control regions	CR($t\bar{t}$)	CR(W^+)	CR(W^-)
Observed events	911	3143	1653
Fitted bkg events	907.41 ± 30.52	3135.45 ± 56.87	1665.08 ± 37.50
Fitted Top1L events	846.96 ± 34.11	748.75 ± 83.42	720.78 ± 86.33
Fitted SingleTop events	19.82 ± 11.53	276.59 ± 69.50	257.00 ± 70.15
Fitted Wjets events	3.18 ± 0.75	2005.00 ± 98.23	625.41 ± 42.11
Fitted Zjets events	$0.13^{+0.16}_{-0.13}$	6.63 ± 0.99	8.39 ± 1.29
Fitted Diboson events	0.87 ± 0.25	88.85 ± 15.55	46.05 ± 8.01
Fitted ttV events	31.01 ± 7.12	8.16 ± 2.69	5.96 ± 1.52
Fitted ttH events	4.37 ± 0.41	1.12 ± 0.17	1.17 ± 0.11
Fitted tWZ events	1.07 ± 0.29	0.36 ± 0.13	0.32 ± 0.11
MC exp. SM events	887.37 ± 88.05	3189.60 ± 85.25	1759.71 ± 97.50
MC exp. Top1L events	824.87 ± 86.06	801.90 ± 36.82	785.78 ± 51.79
MC exp. SingleTop events	21.98 ± 11.84	307.91 ± 73.54	292.39 ± 77.62
MC exp. Wjets events	3.06 ± 0.75	1973.56 ± 21.27	619.13 ± 17.57
MC exp. Zjets events	$0.14^{+0.17}_{-0.14}$	6.62 ± 0.99	8.46 ± 1.33
MC exp. Diboson events	0.88 ± 0.25	89.91 ± 15.87	46.48 ± 8.12
MC exp. ttV events	30.96 ± 7.19	8.19 ± 2.74	5.96 ± 1.53
MC exp. ttH events	4.40 ± 0.42	1.14 ± 0.17	1.18 ± 0.11
MC exp. tWZ events	1.07 ± 0.29	0.36 ± 0.13	0.33 ± 0.11

Table 7.7: Results of the background-only fit in the control regions for the single lepton channel of the search targeting the 2HDM+ a $tW+E_T^{\text{miss}}$ signature. This fit includes only the control regions used to normalise the $t\bar{t}$ and W +jets backgrounds.

2140

Validation regions	VR1(tt)	VR2(tt)	VR1(W^+)	VR1(W^-)	VR2(W^+)	VR2(W^-)
Observed events	1389	482	6127	4479	651	464
Fitted bkg events	$1394.19 \pm 87.29463.79$	$\pm 33.546721.98$	$\pm 451.825025.60$	$\pm 440.57613.26$	$\pm 69.87475.28$	± 49.85
Fitted Top1L events	$1221.12 \pm 70.15282.62$	$\pm 28.473644.44$	$\pm 331.573570.86$	$\pm 354.94282.17$	$\pm 40.09285.73$	± 41.18
Fitted SingleTop events	$53.19^{+59.36}_{-53.19}$	56.98 ± 24.51	626.01 ± 280.23	612.94 ± 274.02	71.09 ± 36.09	73.39 ± 38.19
Fitted Wjets events	39.07 ± 8.23	$68.62 \pm 11.942245.29$	± 131.23	$719.06 \pm 48.51203.16$	± 42.05	70.12 ± 12.03
Fitted Zjets events	3.97 ± 2.14	2.67 ± 0.46	7.66 ± 1.05	7.33 ± 1.00	3.56 ± 0.93	2.38 ± 0.39
Fitted Diboson events	15.29 ± 3.21	27.15 ± 5.48	160.21 ± 28.44	85.60 ± 15.61	34.51 ± 7.06	25.89 ± 5.81
Fitted ttV events	54.42 ± 12.05	22.54 ± 5.03	32.39 ± 2.79	23.86 ± 3.07	16.34 ± 3.79	15.27 ± 3.53
Fitted ttH events	3.57 ± 0.27	0.71 ± 0.04	4.48 ± 0.33	4.37 ± 0.43	0.69 ± 0.03	0.71 ± 0.05
Fitted tWZ events	3.56 ± 0.82	2.50 ± 0.62	1.51 ± 0.17	1.58 ± 0.22	1.72 ± 0.44	1.79 ± 0.46
MC exp. SM events	$1372.55 \pm 136.76479.15$	$\pm 31.636531.69$	$\pm 623.894916.48$	$\pm 572.80646.06$	$\pm 76.28513.95$	± 55.99
MC exp. Top1L events	$1196.25 \pm 120.04295.27$	$\pm 11.813446.89$	$\pm 545.333431.71$	$\pm 495.53307.24$	$\pm 29.76315.14$	± 29.76
MC exp. SingleTop events	$56.60^{+61.50}_{-56.60}$	60.42 ± 24.75	663.43 ± 286.28	650.26 ± 279.62	79.55 ± 36.91	82.83 ± 38.83
MC exp. Wjets events	38.71 ± 7.57	67.65 ± 10.70	2213.59 ± 60.05	$710.50 \pm 27.57202.11$	± 38.29	69.50 ± 10.63
MC exp. Zjets events	3.90 ± 2.12	2.67 ± 0.47	7.73 ± 1.07	7.40 ± 1.03	3.53 ± 0.94	2.40 ± 0.40
MC exp. Diboson events	15.47 ± 3.26	27.35 ± 5.53	161.45 ± 28.79	86.62 ± 15.95	34.78 ± 7.11	26.22 ± 5.91
MC exp. ttV events	54.45 ± 12.19	22.57 ± 5.09	32.55 ± 2.84	23.97 ± 3.11	16.41 ± 3.85	15.34 ± 3.58
MC exp. ttH events	3.60 ± 0.28	0.72 ± 0.04	4.52 ± 0.34	4.42 ± 0.44	0.70 ± 0.03	0.72 ± 0.05
MC exp. tWZ events	3.58 ± 0.83	2.52 ± 0.63	1.52 ± 0.18	1.59 ± 0.23	1.73 ± 0.44	1.80 ± 0.46

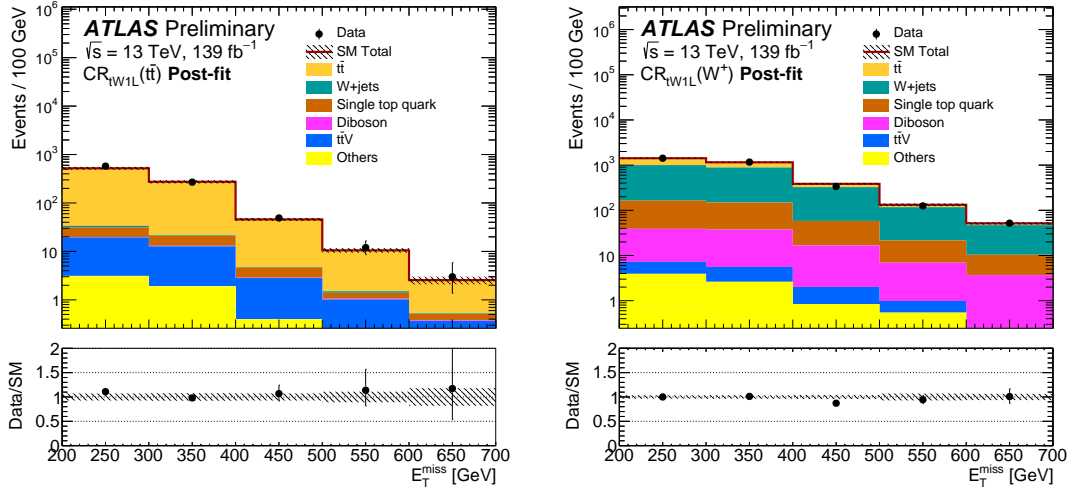
Table 7.8: Results of the background-only fit in the validation regions for the single lepton channel of the search targeting the 2HDM+ a $tW + E_T^{\text{miss}}$ signature. This fit includes only the control regions used to normalise the tt and W +jets backgrounds.

Signal regions	SR1LBin0	SR1LBin1	SR1LBin2	SR1LBin3	SR1LBin4
Observed events	182	191	60	24	12
Fitted bkg events	169.12 ± 13.98	171.28 ± 13.34	54.70 ± 6.05	20.16 ± 2.84	15.55 ± 2.79
Fitted Top1L events	101.34 ± 11.94	83.65 ± 11.53	20.07 ± 4.56	5.12 ± 1.70	2.31 ± 1.48
Fitted SingleTop events	16.28 ± 5.19	17.26 ± 5.22	5.42 ± 3.23	2.00 ± 1.77	$1.68^{+2.02}_{-1.68}$
Fitted Wjets events	27.77 ± 4.02	37.05 ± 4.34	14.24 ± 2.44	6.11 ± 0.97	5.87 ± 1.08
Fitted Zjets events	2.02 ± 0.91	1.10 ± 0.68	0.33 ± 0.09	0.15 ± 0.04	0.15 ± 0.02
Fitted Diboson events	7.20 ± 1.69	9.65 ± 2.00	4.59 ± 1.00	2.24 ± 0.47	2.59 ± 0.65
Fitted ttV events	12.28 ± 1.36	19.55 ± 3.51	8.71 ± 1.20	4.05 ± 0.72	2.53 ± 0.45
Fitted ttH events	0.56 ± 0.06	0.60 ± 0.06	0.17 ± 0.02	0.06 ± 0.02	0.03 ± 0.00
Fitted tWZ events	1.66 ± 0.21	2.42 ± 0.46	1.17 ± 0.15	0.42 ± 0.09	0.39 ± 0.09
MC exp. SM events	172.49 ± 16.86	174.00 ± 14.12	55.72 ± 6.71	20.60 ± 3.05	16.76 ± 3.15
MC exp. Top1L events	103.13 ± 12.92	85.61 ± 10.81	20.39 ± 4.67	5.28 ± 1.72	2.92 ± 1.51
MC exp. SingleTop events	17.86 ± 5.85	18.63 ± 5.36	6.02 ± 3.34	2.33 ± 1.85	2.35 ± 2.17
MC exp. Wjets events	27.59 ± 3.69	36.22 ± 4.24	14.21 ± 2.25	6.06 ± 0.87	5.75 ± 1.00
MC exp. Zjets events	2.08 ± 0.91	1.09 ± 0.67	0.33 ± 0.09	0.15 ± 0.04	0.15 ± 0.02
MC exp. Diboson events	7.30 ± 1.72	9.73 ± 2.01	4.64 ± 1.02	2.24 ± 0.47	2.62 ± 0.66
MC exp. ttV events	12.30 ± 1.38	19.67 ± 3.59	8.77 ± 1.22	4.06 ± 0.72	2.55 ± 0.46
MC exp. ttH events	0.56 ± 0.06	0.61 ± 0.06	0.18 ± 0.02	0.06 ± 0.02	0.03 ± 0.00
MC exp. tWZ events	1.67 ± 0.22	2.44 ± 0.46	1.18 ± 0.15	0.42 ± 0.10	0.39 ± 0.09

Table 7.9: Results of the background-only fit in the signal region for the single lepton channel of the search targeting the 2HDM+ a $tW + E_T^{\text{miss}}$ signature. This fit includes only the control regions used to normalise the $t\bar{t}$ and W +jets backgrounds.

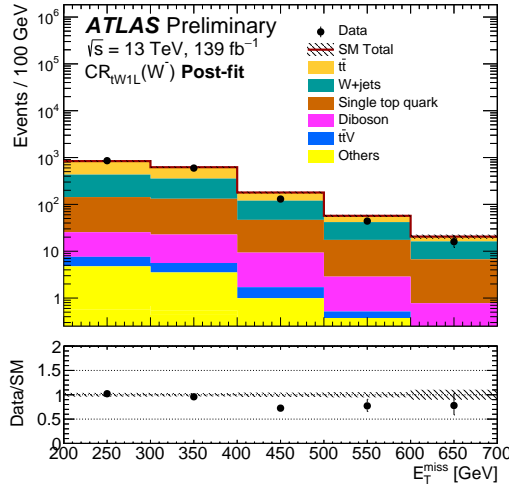
1 ℓ analysis	
$\mu(t\bar{t})$	0.96 ± 0.08
$\mu(W)$	1.01 ± 0.05
1 ℓ + 2 ℓ combination	
$\mu(t\bar{t} \ 1\ell)$	0.96 ± 0.08
$\mu(t\bar{t} \ 2\ell)$	1.00 ± 0.03
$\mu(W)$	1.01 ± 0.05
$\mu(WZ)$	0.75 ± 0.26
$\mu(t\bar{t}Z)$	0.81 ± 0.16

Table 7.10: Background normalisation factors the $tW + E_T^{\text{miss}}$ analysis



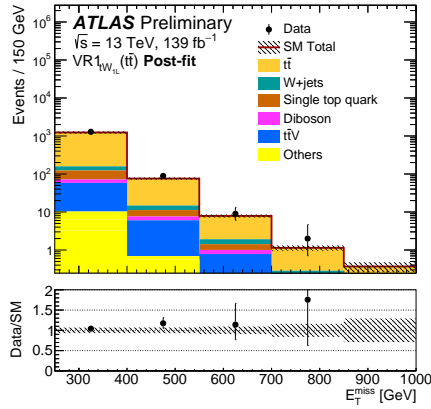
(a) E_T^{miss} distribution in CR($t\bar{t}$)

(b) E_T^{miss} distribution in CR(W^+)

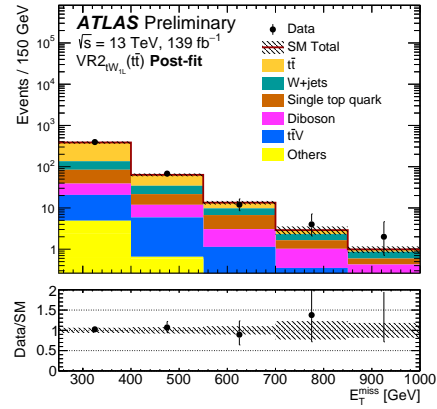


(c) E_T^{miss} distribution in CR(W^-)

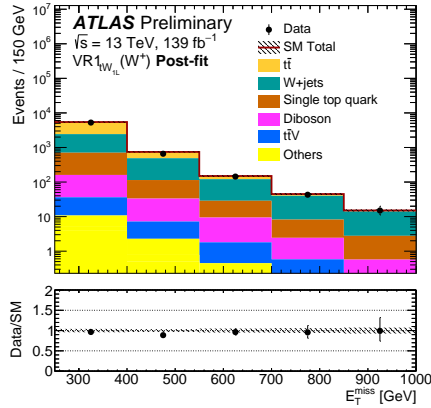
Figure 7.5: Post-fit distributions of the E_T^{miss} variable in all CRs. Excellent data/MC agreement is observed. The uncertainty band on the ratio contains the MC statistical, experimental and modelling uncertainties.



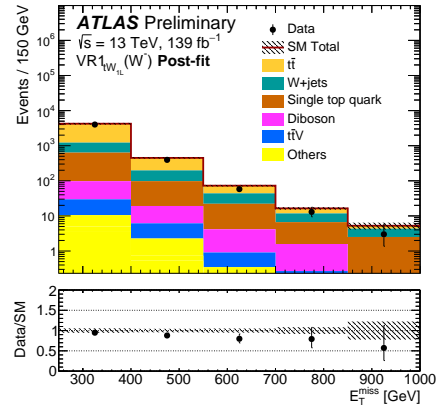
(a) E_T^{miss} distribution in VR1($t\bar{t}$)



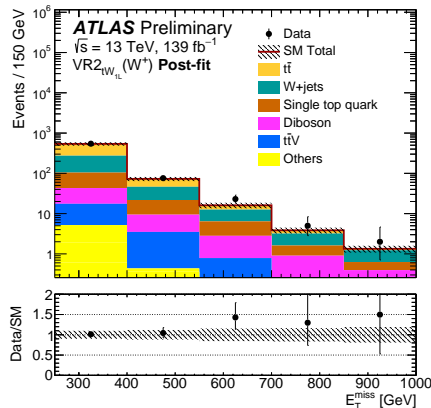
(b) E_T^{miss} distribution in VR2($t\bar{t}$)



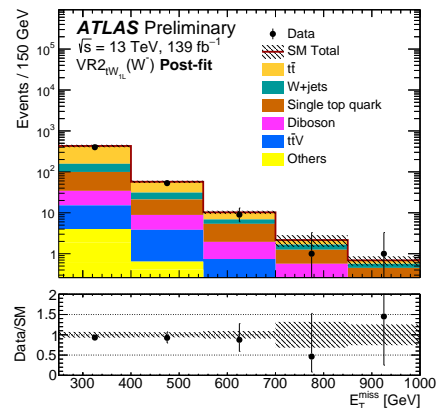
(c) E_T^{miss} distribution in VR1(W^+)



(d) E_T^{miss} distribution in VR1(W^-)



(e) E_T^{miss} distribution in VR2(W^+)



(f) E_T^{miss} distribution in VR2(W^-)

Figure 7.6: Plots showing the E_T^{miss} distribution in all VRs. Good agreement between data and MC in all regions is observed. The uncertainty band on the ratio includes MC statistical, experimental and modelling uncertainties.

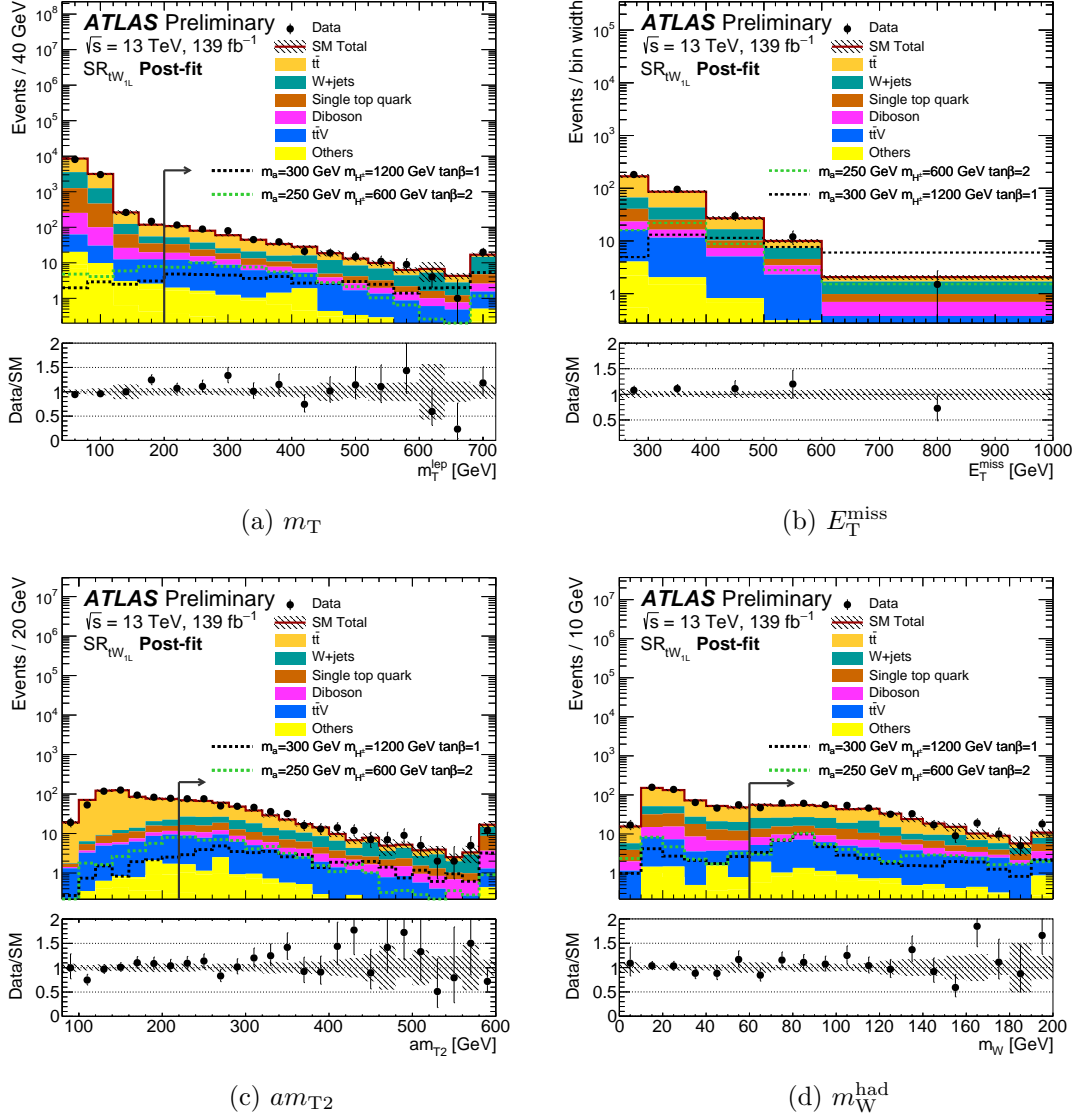


Figure 7.7: Plots showing the post-fit N-1 distributions of the key kinematic variables. In these plots, all selections are applied except those on the variable being plotted. All uncertainties are included in the error band on the ratio. No significant excess is observed in the SR bins.

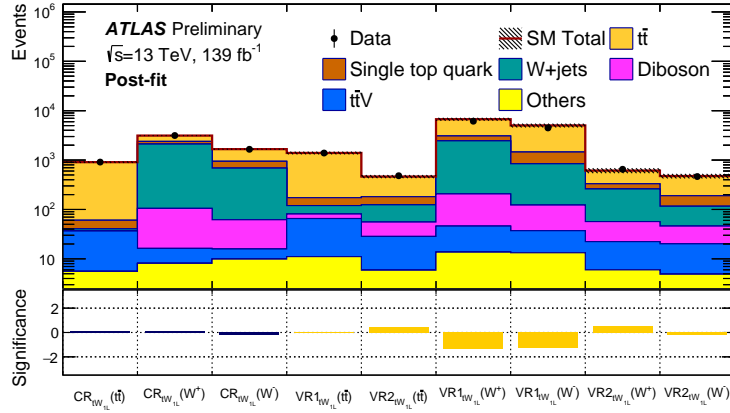
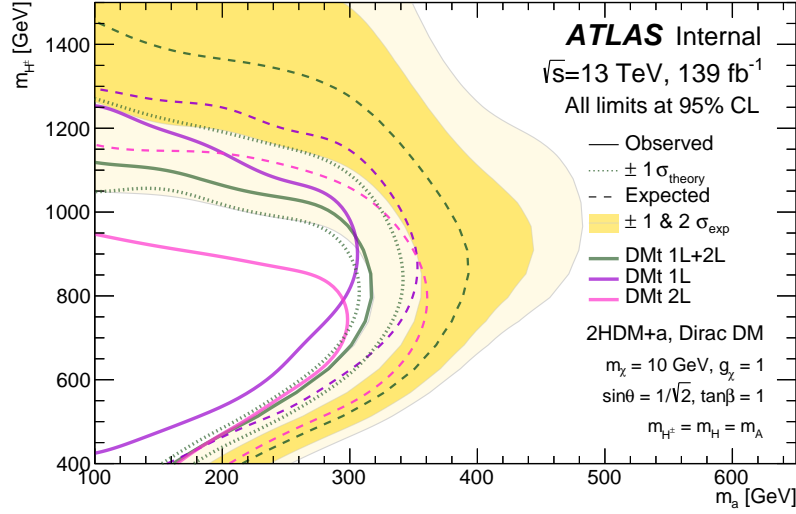


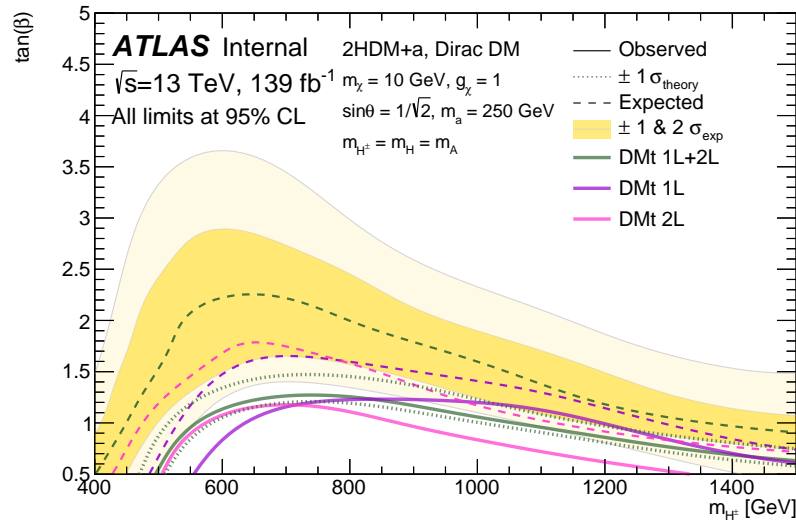
Figure 7.8: Summary plot showing the data/MC agreement in all control and validation regions for the single lepton channel of the search targeting the 2HDM+ a $tW + E_T^{\text{miss}}$ signature. The uncertainty used to calculate the significance of the data/MC difference includes the statistical component on the MC and the data, as well as the total systematic uncertainty on the background estimate.

2141 Model-dependent limits

2142 In the absence of a significant excess, limits are set on the 2HDM+ a model at 95% con-
 2143 fidence limits using the previously described prescription. Model-dependent limits are set
 2144 on the DM t and the DM $t + t\bar{t}$ signatures, in both the $m_a - m_{H^\pm}$ and $m_{H^\pm} - \tan\beta$ planes.
 2145 For the DM t signature, H^\pm masses are excluded up to 1250 GeV for $m_a = 100$ GeV, while
 2146 for the DM $t + t\bar{t}$ signature masses above 1400 GeV are excluded. The observed limit of
 2147 the statistical combination of the 1ℓ and 2ℓ channels is not as sensitive as the dedicated 1ℓ
 2148 channel due to the 2σ excess in the 2ℓ SR.

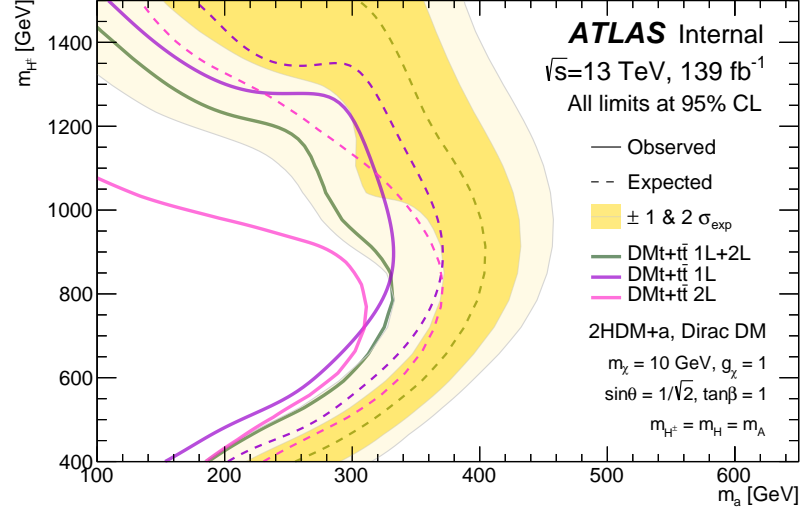


(a)

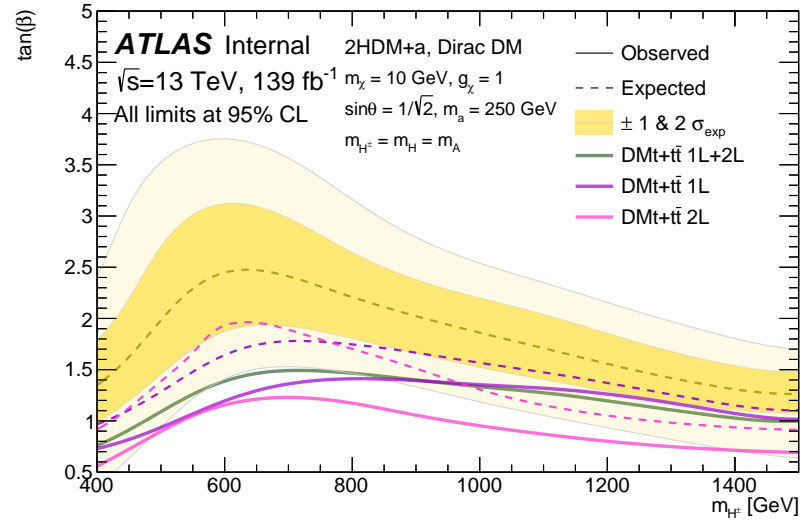


(b)

Figure 7.9: Plots showing the sensitivity to the 2HDM+ a signal with the $tW + E_T^{\text{miss}}$ signature. Limits are shown in both the m_a - m_{H^\pm} plane (a) and the m_{H^\pm} - $\tan(\beta)$ plane (b). Limits are shown for the analyses targeting the single lepton and di-lepton final states, along with the statistical combination of both channels.



(a)



(b)

Figure 7.10: Plots showing the sensitivity to the 2HDM+a signal for both tW and $t\bar{t}$ signatures. Limits are shown in both the m_a - m_{H^\pm} plane (a) and the m_{H^\pm} - $\tan(\beta)$ plane (b). Limits are shown for the analyses targeting the single lepton and di-lepton final states, along with the statistical combination of both channels.

2149 **Model-independent limits**

2150 In addition to model-dependent limits being set on the 2HDM+ a signal model, with both
 2151 tW and $tW + t\bar{t}$ signatures, 95% CL limits are set on any generic BSM processes using the
 2152 model-independent fit strategy described in Section 5.5. The limits are presented as limits
 2153 on the *visible* cross-section, $\sigma_{\text{vis}} = \epsilon \cdot A \cdot \sigma_{\text{BSM}}$, where ϵ is the signal selection efficiency,
 2154 A is the detector acceptance, and σ_{vis} is the production cross-section for a generic BSM
 2155 process. To set limits on a generic BSM process, the SR definition from Table 7.3 are
 2156 modified, such that the individual SR bins have no upper $E_{\text{T}}^{\text{miss}}$ limit and rather only a
 2157 lower $E_{\text{T}}^{\text{miss}}$ threshold. The yields in these modified, ‘inclusive’ SR bins are shown in Table
 2158 7.11. The results of the model-independent fit are shown in Table 7.12, as 95% CL limits
 2159 on the expected and observed number of signal events.

Inclusive signal regions					
$E_{\text{T}}^{\text{miss}}$ threshold [GeV]	> 250	> 300	> 400	> 500	> 600
Observed events	469	287	96	36	12
Fitted bkg events	431.47 ± 27.12	261.90 ± 20.10	90.65 ± 10.07	35.94 ± 5.22	15.54 ± 2.77
Fitted Top1L events	212.61 ± 25.01	111.14 ± 17.69	27.51 ± 7.36	7.44 ± 2.94	2.31 ± 1.48
Fitted SingleTop events	43.28 ± 14.49	26.66 ± 11.76	9.35 ± 6.53	3.92 ± 3.85	$1.68^{+2.02}_{-1.68}$
Fitted Wjets events	91.05 ± 7.64	63.29 ± 5.47	26.24 ± 2.82	11.99 ± 1.67	5.87 ± 1.08
Fitted Zjets events	3.76 ± 1.03	1.72 ± 0.69	0.62 ± 0.12	0.30 ± 0.05	0.15 ± 0.02
Fitted Diboson1L events	26.26 ± 5.49	19.06 ± 3.92	9.42 ± 1.97	4.83 ± 1.01	2.59 ± 0.65
Fitted ttV1L events	47.01 ± 2.76	34.75 ± 2.39	15.27 ± 1.17	6.57 ± 0.48	2.53 ± 0.33
Fitted ttH events	1.42 ± 0.09	0.87 ± 0.07	0.26 ± 0.02	0.09 ± 0.02	0.03 ± 0.00
Fitted tWZ events	6.07 ± 0.37	4.40 ± 0.31	1.99 ± 0.13	0.81 ± 0.08	0.39 ± 0.04
MC exp. SM events	439.58 ± 32.24	267.09 ± 22.29	93.09 ± 11.12	37.36 ± 5.64	16.76 ± 3.13
MC exp. Top1L events	217.33 ± 24.57	114.20 ± 16.85	28.59 ± 7.33	8.20 ± 2.91	2.92 ± 1.51
MC exp. SingleTop events	47.20 ± 15.05	29.34 ± 12.03	10.70 ± 6.75	4.69 ± 4.00	2.35 ± 2.17
MC exp. Wjets events	89.83 ± 6.17	62.24 ± 4.79	26.02 ± 2.29	11.81 ± 1.49	5.75 ± 1.00
MC exp. Zjets events	3.80 ± 1.04	1.72 ± 0.68	0.63 ± 0.12	0.30 ± 0.05	0.15 ± 0.02
MC exp. Diboson1L events	26.52 ± 5.55	19.23 ± 3.96	9.50 ± 1.99	4.86 ± 1.01	2.62 ± 0.66
MC exp. ttV1L events	47.36 ± 2.90	35.05 ± 2.50	15.38 ± 1.20	6.61 ± 0.49	2.55 ± 0.34
MC exp. ttH events	1.44 ± 0.09	0.88 ± 0.07	0.27 ± 0.02	0.09 ± 0.02	0.03 ± 0.00
MC exp. tWZ events	6.11 ± 0.38	4.44 ± 0.32	2.00 ± 0.13	0.82 ± 0.09	0.39 ± 0.04

Table 7.11: Table showing the expected and observed yields in the modified signal regions for the determination of the model-independent limits.

Region	$\langle \epsilon \sigma \rangle_{\text{obs}}^{95} [\text{fb}]$	S_{obs}^{95}	S_{exp}^{95}
SR1L ($E_{\text{T}}^{\text{miss}} > 250 \text{ GeV}$)	0.72	100.6	$66.7^{+32.7}_{-16.4}$
SR1L ($E_{\text{T}}^{\text{miss}} > 300 \text{ GeV}$)	0.51	70.8	$54.1^{+16.0}_{-15.9}$
SR1L ($E_{\text{T}}^{\text{miss}} > 400 \text{ GeV}$)	0.24	32.9	$29.4^{+10.1}_{-6.4}$
SR1L ($E_{\text{T}}^{\text{miss}} > 500 \text{ GeV}$)	0.14	18.9	$18.7^{+7.6}_{-4.9}$
SR1L ($E_{\text{T}}^{\text{miss}} > 600 \text{ GeV}$)	0.08	10.6	$12.0^{+2.7}_{-3.6}$

Table 7.12: Table showing the model-independent limits derived for the five modified inclusive SRs. Visible cross-sections of BSM physics upto 0.72fb are excluded at 95% confidence limits, translating to an upper limit of around 100 events with a dataset of 139fb^{-1} .

2160

Part III

2161

High-Luminosity LHC studies

2162 Chapter 8

2163 Sensitivity to $\tilde{\chi}_1^\pm \tilde{\chi}_2^0$ pair-production 2164 at the HL-LHC

2165 This chapter explores the potential sensitivity of a search for chargino-neutralino pair-
2166 production using the ATLAS detector during the HL-LHC phase of operation. The HL-
2167 LHC is expected to begin operation in the latter half of the 2020's, bringing instantaneous
2168 luminosities around an order of magnitude higher than those currently at the LHC ($7.5 \times$
2169 10^{34}), along with an increase in centre-of-mass energy to $\sqrt{s} = 14$ TeV. It is expected that
2170 by the end of the HL-LHC phase, ATLAS will have taken 3000fb^{-1} of data, an expected
2171 ten-fold increase over the combination of Runs 2 and 3.

2172 Along with the increased luminosity and collision energy delivered by the LHC, the
2173 ATLAS detector will be undergoing major upgrades in Long Shutdown 3 (LS3), providing
2174 an overhaul of many of the detector's subsystems. Of particular note is the new Inner
2175 Tracker (ITk), which will replace the current innermost tracking layers of the current
2176 ATLAS detector, vastly improving on the vertex resolution which will enable accurate track
2177 reconstruction in collisions with an average number of interactions per bunch-crossing, $\langle\mu\rangle$,
2178 of 200. Figure 8.1 shows a simulated $t\bar{t}$ event display from the ATLAS ITk in the expected
2179 pileup conditions at the HL-LHC.

2180 With the increased centre-of-mass energy and the expected 3000fb^{-1} dataset, the
2181 physics analysis potential of the HL-LHC is unprecedented. Much of the HL-LHC physics
2182 program will be devoted to precision measurements of properties related to the Higgs boson
2183 and its relationship with the symmetry breaking mechanism of the electroweak sector
2184 of the SM. First sensitivity to the Higgs self-coupling is expected to be possible in the
2185 $HH \rightarrow b\bar{b}\gamma\gamma$ channel through both a conventional cut-and-count analysis [62] and a mul-
2186 tivariate analysis [63]. This measurement will be used in combination with measurements
2187 in other final states, such as $b\bar{b}\tau\tau$ and $b\bar{b}b\bar{b}$ [64], further increasing sensitivity. It is also
2188 expected that measurements of the largest Higgs boson couplings to SM particles will be
2189 done with percent-level precision. Along with increased precision in measurements and

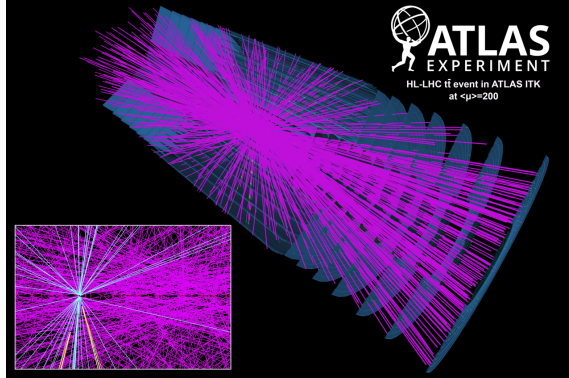


Figure 8.1: An event display of a simulated $t\bar{t}$ event in the ATLAS ITk at the HL-LHC, where there are an expected 200 interactions per bunch-crossing.

2190 sensitivity to SM properties, the HL-LHC will also bring increased sensitivity to TeV-scale
 2191 new physics. This chapter describes one such prospects analysis, forming part of a plethora
 2192 of sensitivity studies [65].

2193 The analysis described in this chapter targets the same signal model as in Chapter
 2194 ??, with a final state of a single electron/muon, two b -jets and E_T^{miss} . The sensitivity is
 2195 assessed in the context of current expected HL-LHC conditions. Due to the huge dataset
 2196 expected to be collected at the HL-LHC, the sensitivity is expected to reach far beyond
 2197 the Run-2 sensitivity, and as such, mass upto 1500 GeV are considered for the $\tilde{\chi}_1^\pm/\tilde{\chi}_2^0$.

2198 8.1 MC simulation

2199 Signal samples for this study are generated at leading-order in QCD, with upto two ad-
 2200 ditional partons, using MADGRAPH5_aMC@NLO [66] for the matrix element (ME), while
 2201 PYTHIA 8 [67] is used for the parton showering (PS), hadronisation and underlying event
 2202 (UE). The A14 tune is used for PYTHIA 8 [68] while the NNPDF23LO PDF set [69] is used
 2203 for generation. Partons are matched between the ME and PS using the CKKW-L [70] pre-
 2204 scription, with the scale used for matching set to one quarter of the mass of the $\tilde{\chi}_1^\pm/\tilde{\chi}_2^0$. The
 2205 cross-sections are evaluated at next-to-leading order in α_s and next-to-leading logarithmic
 2206 precision for the resummation of soft gluon emissions. The nominal cross section is de-
 2207 termined by evaluating the cross section predictions with different PDF sets, factorisation
 2208 and renormalisation scales [71]. Similarly to the analyses previously described, numerous
 2209 generator configurations were used to generate the MC background samples. These are
 2210 summarised in Table 8.1.

2211 All samples are generated at truth-level. A parameterised simulation of the detector
 2212 response is applied to all truth-level MC samples. This will be described in more detail in
 2213 the following section.

Process	Generator + fragmentation/hadronisation	Tune	PDF set	Cross-section order
W/Z +jets	SHERPA 2.2.1 [?]	Default	NNPDF30NNLO [?]	NNLO
$t\bar{t}$	POWHEG-Box v2 + PYTHIA 8.186	A14	NNPDF23LO [?]	NNLO+NNLL
Single top	POWHEG-Box v1 or v2 + PYTHIA 6.428 [?]	PERUGIA2012 [?]	CT10 [?]	NNLO+NNLL
Diboson (fully leptonic)	SHERPA 2.2.1	Default	NNPDF30NNLO	NLO
(semi leptonic)	POWHEG-Box v1 + PYTHIA 8.186	AZNLO [?]	CTEQ6L1	NLO
Higgs	POWHEG-Box v2 + PYTHIA 8.186	AZNLO	CTEQ6L1	NNLO+NNLL

Table 8.1: Summary table showing the ME and PS configurations used to generate the SM MC samples for this study.

2214 8.2 Detector simulation

2215 In order to make meaningful predictions of sensitivity, a simulation of the ATLAS detector
 2216 at the HL-LHC was developed through a set of parameterised smearing functions. These
 2217 functions, known as the UpgradePerformanceFunctions, simulate the detector response by
 2218 smearing the kinematic and angular properties of the physics objects, as well as providing
 2219 additional collision vertices to simulate the pileup conditions at the HL-LHC. The treat-
 2220 ment of each object relevant to this chapter will be discussed separately. Some shorthand
 2221 will now be introduced for the following sections. $R(m, n)$ represents a random number
 2222 drawn from a uniform distribution in the range m to n . $G(\mu, \sigma)$ represents a number drawn
 2223 from a Gaussian distribution with a mean, μ , and a standard deviation, σ .

2224 Leptons

2225 The steps taken in the reconstruction of charged leptons is highly dependent on the gen-
 2226 eration of lepton being considered, but there are some common steps. Lepton ID working
 2227 points are assigned for all three generations of charged leptons, and the detector response
 2228 to the E_T for electrons and taus and p_T for muons is simulated. The charge-flip probability
 2229 (the probability that the reconstructed lepton has the opposite charge to its true value),
 2230 $P(\ell_{truth}^\pm \rightarrow \ell_{reco}^\mp)$, is explicitly parameterised for electrons and is also possible for muons.
 2231 Finally, the misreconstruction of an electron as a photon is parameterised.

2232
 2233 A parameterisation of the lepton ID efficiencies is used in order to choose which lepton
 2234 ID working points the lepton has passed. For each lepton generation there are three ID
 2235 efficiency parameterisations, one corresponding to each working point. These parameteri-
 2236 sations can be seen in Figure A.1. For a given lepton, the three ID efficiencies corresponding
 2237 to the ID working points are retrieved, and all which satisfy $R(0, 1) < \epsilon_{ID}^i$, with $i = 1, 2, 3$,
 2238 are passed.

2239

2240 The p_T resolution for leptons is simulated differently for muons than for electrons and
 2241 taus. For the former, the key quantity is the charge (in units of e) to transverse momen-
 2242 tum ratio, $\frac{q}{p_T}$, while for electrons and taus it is the energy, E . For both quantities, the
 2243 ‘reconstructed’ value is as follows:

$$E_{reco} = E_{truth} + G(0, \Delta E)$$

$$\left(\frac{q}{p_T}\right)_{reco} = \left(\frac{q}{p_T}\right)_{truth} + G\left(0, \Delta\left(\frac{q}{p_T}\right)\right) \quad (8.2.1)$$

2244 Here, ΔE and $\Delta\frac{q}{p_T}$ denote the resolutions on the respective quantity. The reconstructed
 2245 muon transverse momentum is then given by $p_T^{reco} = \left|\left(\frac{q}{p_T}\right)_{reco}^{-1}\right|$, while for electrons and
 2246 taus it is given by $p_T^{reco} = p_T^{truth} \times \frac{E_{reco}}{E_{truth}}$.

2247

2248 The charge-flip probability for electrons is parameterised in η and differs slightly for the
 2249 three ID working points, as can be seen in Figure A.1. The charge-flip probability is deter-
 2250 mined by the tightest working point which is passed by the electron. A charge-flip occurs
 2251 if the following condition is satisfied; $R(0, 1) < P(e_{truth}^\pm \rightarrow e_{reco}^\mp)$. For muons, particularly
 2252 high- p_T or η muons, can undergo a charge flip when the $\frac{q}{p_T}$ is smeared.

2253

2254 Finally, electrons being misreconstructed as a photons is simulated through a parame-
 2255 terisation in η . For electrons with a $p_T > 20$ GeV, the probability of an electron being
 2256 reconstructed as a photon is 2% for electrons with $|\eta| < 1.37$ and is 5% for electrons with
 2257 $|\eta| > 1.52$. An electron is misreconstructed as a photon if $R(0, 1) < P(e \rightarrow \gamma)$.

2258 Jets and flavour tagging

2259 To simulate jet reconstruction, the first step of the detector simulation process is to smear
 2260 the jet energy and p_T . The jet p_T is smeared by a multiplicative factor, $G(1, \Delta E)$, where
 2261 ΔE represents the relative jet energy resolution determined from the parameterisation
 2262 shown in Figure A.3a. The jet energy is smeared by multiplying the true jet energy by
 2263 $\frac{p_T^{smeared}}{p_T^{truth}}$.

2264

2265 Jet flavour-tagging, in particular the tagging of jets originating from b -quarks, is of great
 2266 importance to the study described in this chapter. The b -tagging working point used in
 2267 this study has a b -tagging efficiency $\epsilon_b = 70\%$, which has much-improved light-jet rejection
 2268 compared to the $\epsilon_b = 85\%$ working point. The flavour-tag efficiency, ϵ_{ftag}^b , is parameterised
 2269 in jet p_T and η , and can be seen in Figure A.3b. Jets which have originated from a b -quark
 2270 at truth-level are b -tagged if $R(0, 1) < \epsilon_{ftag}^b$. The misreconstruction of jets as electrons,
 2271 taus and photons is simulated by parameterising the so-called ‘fake rate’. This is rate at

2272 which an object is misreconstructed as another object.

2273 E_T^{miss}

2274 Smearing the E_T^{miss} requires two steps. At truth-level, the missing transverse energy,
2275 $E_{T, \text{truth}}^{\text{miss}}$, is the sum of the transverse energies of all neutral particles in the event; in this
2276 study, only neutrinos and neutralinos contribute.

2277 To account for mismeasurement due to pileup, $E_{T, \text{truth}}^{\text{miss}}$ is smeared by adding an addi-
2278 tional term, $E_{T, \text{pileup}}^{\text{miss}}$, drawn randomly from the distribution shown in Figure A.4a. The
2279 E_T^{miss} resolution, ΔE_T , is then determined from the parameterisation shown in Figure
2280 A.4b, using the sum of the neutral particle and pileup E_T^{miss} components as an input. The
2281 final E_T^{miss} is then give as:

$$E_T = E_{T, \text{truth}}^{\text{miss}} + G(0, \Delta E_T) \quad (8.2.2)$$

2282 Kinematic distribution comparison

2283 The effects of the detector simulation described in this section can be see in Figure 8.2.
2284 The ‘truth-level’ $t\bar{t}$ distribution includes no detector effects, the ‘truth-level with smearing’
2285 $t\bar{t}$ distributions include the detector simulation described in this section, while the ‘reco-
2286 level’ sample is reconstructed using the full ATLAS detector simulation.

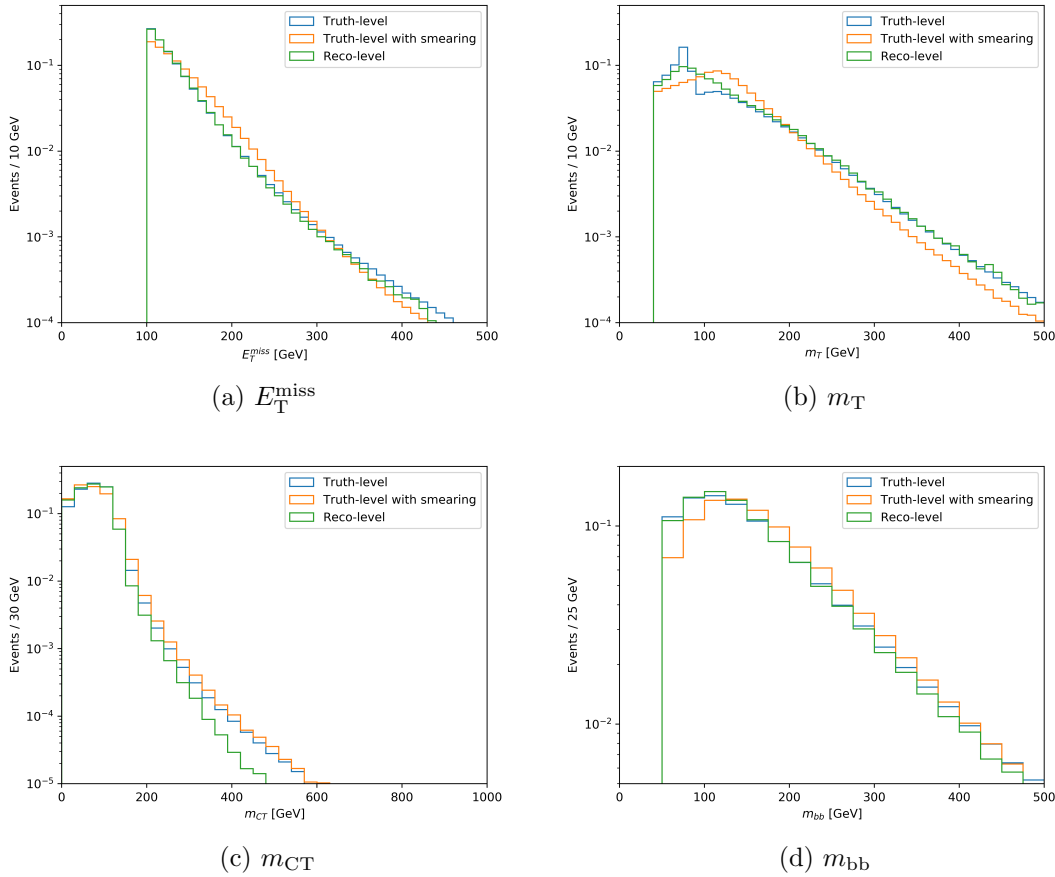


Figure 8.2: The E_T^{miss} , m_T , m_{CT} and m_{bb} distributions at truth-level, truth-level with the detector smearing described in this section, and a fully reconstructed samples. All distributions are normalised to unity to compare only the shape of the distributions and not normalisations.

2287 8.3 Event selection

2288 The object definitions used to reconstruct the leptons and jets are summarised in Table
 2289 8.2 and Table 8.3, respectively.

	Electrons	Muons
p_T	25 GeV	25 GeV
$ \eta $	< 2.47	< 2.7
ID	Tight	Medium

Table 8.2: A summary of the object definitions for leptons in the HL-LHC projection.

2290 Similarly to the 36.1fb^{-1} analysis described in Chapter 6, a number of preliminary
 2291 selections are applied to select events with the single lepton, two b -jet topology, as shown
 2292 in Table 8.4.

	jets	b -jets
p_T	25 GeV	25 GeV
$ \eta $	< 2.5	< 2.5
Jet radius (R)	0.4	0.4
b -tagging WP	-	70%

Table 8.3: A summary of the object definitions for jets in the HL-LHC projection.

Preselection	
Leptons ($p_T \geq 25$ GeV)	1e or 1μ
Jets ($p_T \geq 25$ GeV)	2 or 3
b -jets ($p_T \geq 25$ GeV)	2
m_T	≥ 40 GeV
m_{bb}	≥ 50 GeV
E_T^{miss}	≥ 200 GeV

Table 8.4: A summary of the preliminary selections used for for the HL-LHC projection.

2293 The loose cuts on m_T and m_{bb} are employed to combat MC mismodelling seen in the
 2294 analysis described in Chapter ??, while the cut on E_T^{miss} is used to both reduce the SM
 2295 background and target events containing two $\tilde{\chi}_1^0$ in the final state.

2296

2297 Events passing the preliminary selections listed in Table 8.4 are used as inputs to Boosted
 2298 Decision Tree (BDT) classifiers. The BDTs are implemented in Toolkit for Multivariate
 2299 Data Analysis [41]. In this study, binary classification is performed such that the output
 2300 of the BDT is a single value $\in [-1, 1]$. The key discriminatory variables which are given to
 2301 the BDT classifiers as inputs are the E_T^{miss} , m_T , m_{CT} , m_{bb} and $\Delta R(b_1, b_2)$. Along with
 2302 these, the transverse momentum of the lepton and the two b -jets are useful for background
 2303 rejection. The distributions of E_T^{miss} , m_T and $\Delta R(b_1, b_2)$ for the signal are highly depen-
 2304 dent upon the mass and the mass difference of the $\tilde{\chi}_1^\pm/\tilde{\chi}_2^0$ and $\tilde{\chi}_1^0$, and as such having one
 2305 classifier which performs equally well across the entire phase space is extremely difficult
 2306 to achieve. To aid in this, three BDT classifiers are trained, targeting ‘low’, ‘intermediate’
 2307 and ‘high’ mass-splittings, $\Delta M = m(\tilde{\chi}_1^\pm/\tilde{\chi}_2^0) - m(\tilde{\chi}_1^0)$. SR-Low targets $\Delta M < 300$ GeV,
 2308 SR-Med targets $\Delta M \in [300, 600]$ GeV and SR-High targets $\Delta M > 600$ GeV. The signal
 2309 grid, highlighted with the three targeted regions, is shown in Figure 8.3.

2310 Due to the limited number of MC events in each individual signal sample, all signal
 2311 samples in each mass-splitting regime (‘low’, ‘intermediate’ or ‘high’ ΔM) are summed
 2312 together with an equal weight of 1. The sum of signals for each mass-splitting region
 2313 provide a high-statistics signal sample on which to train the BDTs, with kinematic dis-
 2314 tributions representing a ‘pseudo-average’ of the individual signal samples. A benchmark

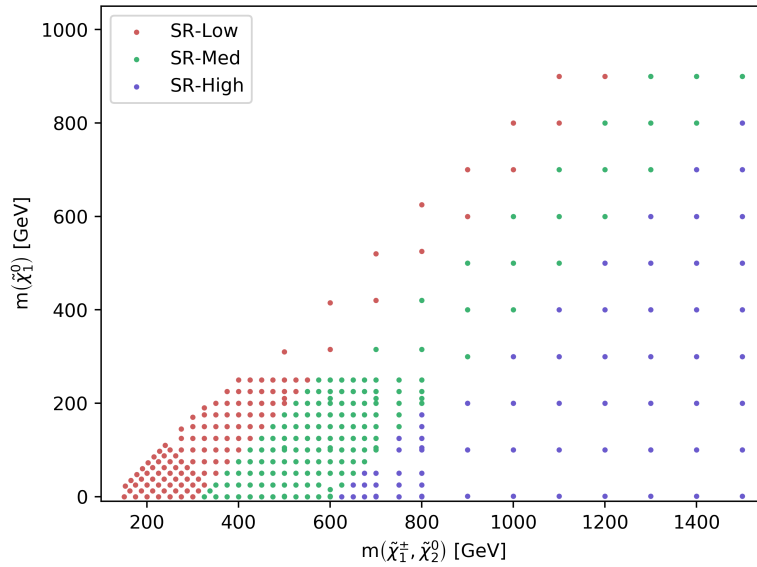
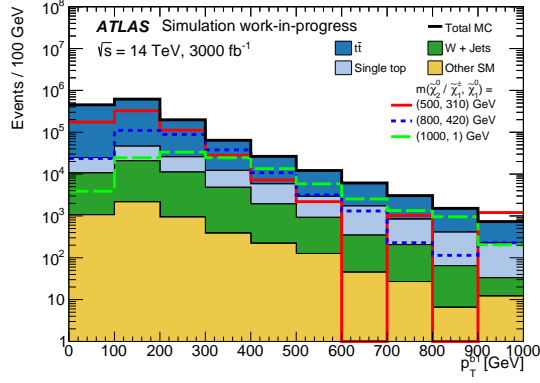
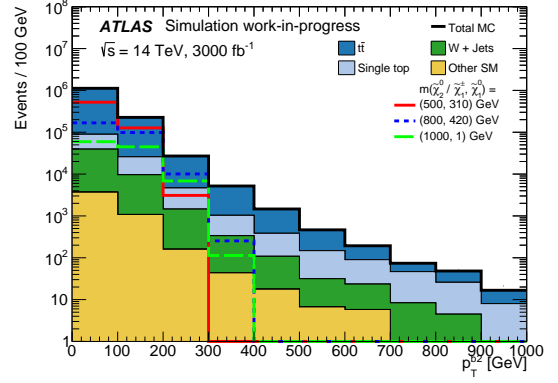
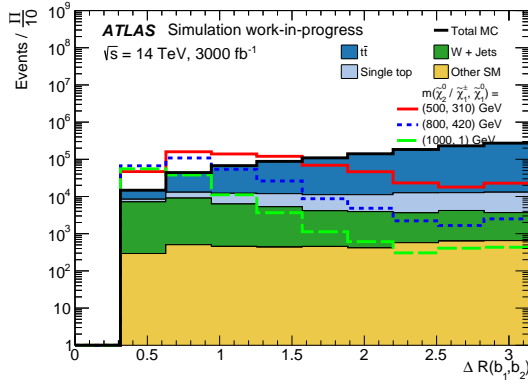
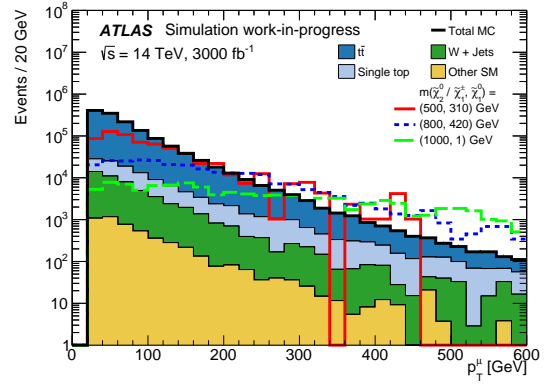
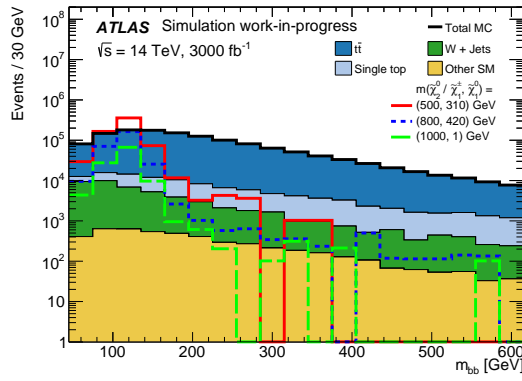
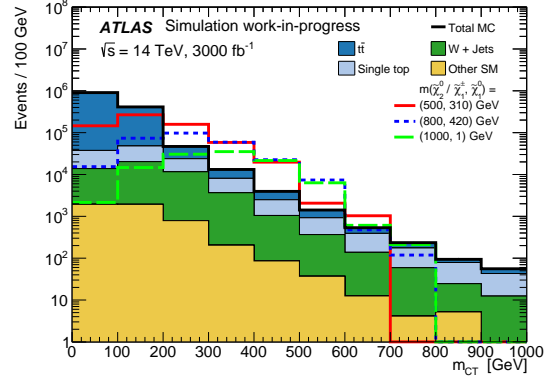


Figure 8.3: Plot showing the separation of the mass plane into the three defined categories.

2315 signal is chosen from each mass-splitting region for the purposes of comparing the kine-
 2316 matic distributions of signal and background, and for later deriving an optimal cut on the
 2317 BDT output. The kinematic distributions forming inputs to the BDTs are shown, with
 2318 benchmark signals overlaid, in Figure 8.4.

(a) p_T^{b1} (b) p_T^{b2} (c) $\Delta R(b_1, b_2)$ (d) p_T^{l1} (e) m_{bb} (f) m_{CT}

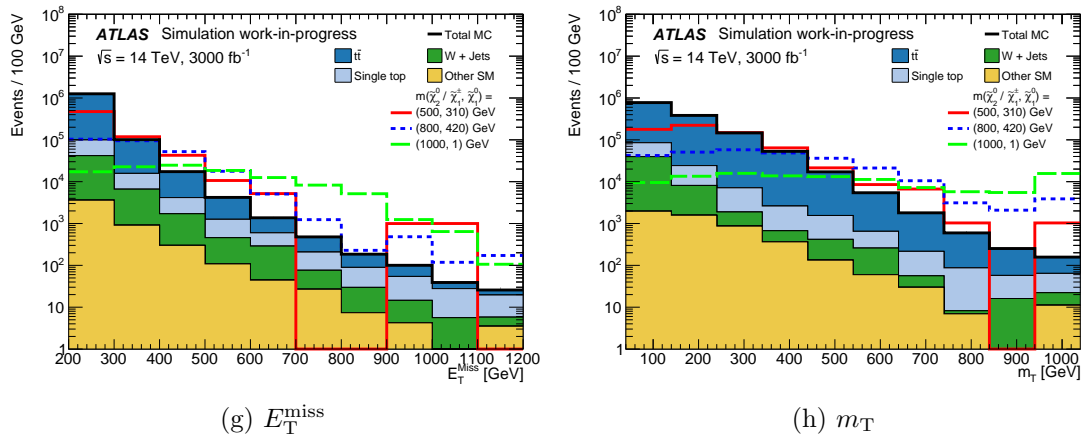


Figure 8.4: Kinematic and angular distributions for the BDT input variables at the preselection-level.

2319 The estimate for signal and background yields in the SRs is obtained by placing a cut
 2320 on the output of the BDTs. The optimal cut value is derived by scanning over the BDT
 2321 output with an increasing lower bound, and calculating the binomial significance, Z_n , for
 2322 that region's benchmark model and the SM background. The optimal cuts are shown in
 2323 Table 8.5.

SR	Signal benchmark $m(\tilde{\chi}_1^\pm / \tilde{\chi}_2^0, \tilde{\chi}_1^0)$ [GeV]	BDT range
SR-M1	(500, 310)	> 0.25
SR-M2	(800, 420)	> 0.35
SR-M3	(1000, 1)	> 0.30

Table 8.5: Benchmark signal models and the corresponding optimised BDT output cut, derived by maximising the binomial significance, Z_n of the benchmark signal over the SM background.

2324 The BDT output distributions for the SM backgrounds and the benchmark signal point
 2325 for each region is shown in Figure 8.5. The arrows in these plots show the cut placed on
 2326 the BDT output.

2327 8.4 Systematic uncertainties

2328 A joint strategy between the ATLAS and CMS collaborations was adopted for estimat-
 2329 ing systematic uncertaines for HL-LHC projection studies. For analyses with an existing
 2330 Run-2 analysis, a prescription for extrapolating the current systematic uncertainties to
 2331 3000 fb^{-1} , where theoretical modelling uncertainties are expected to be half their current
 2332 value. The extrapolation method for experimental uncertainties depend upon the system-

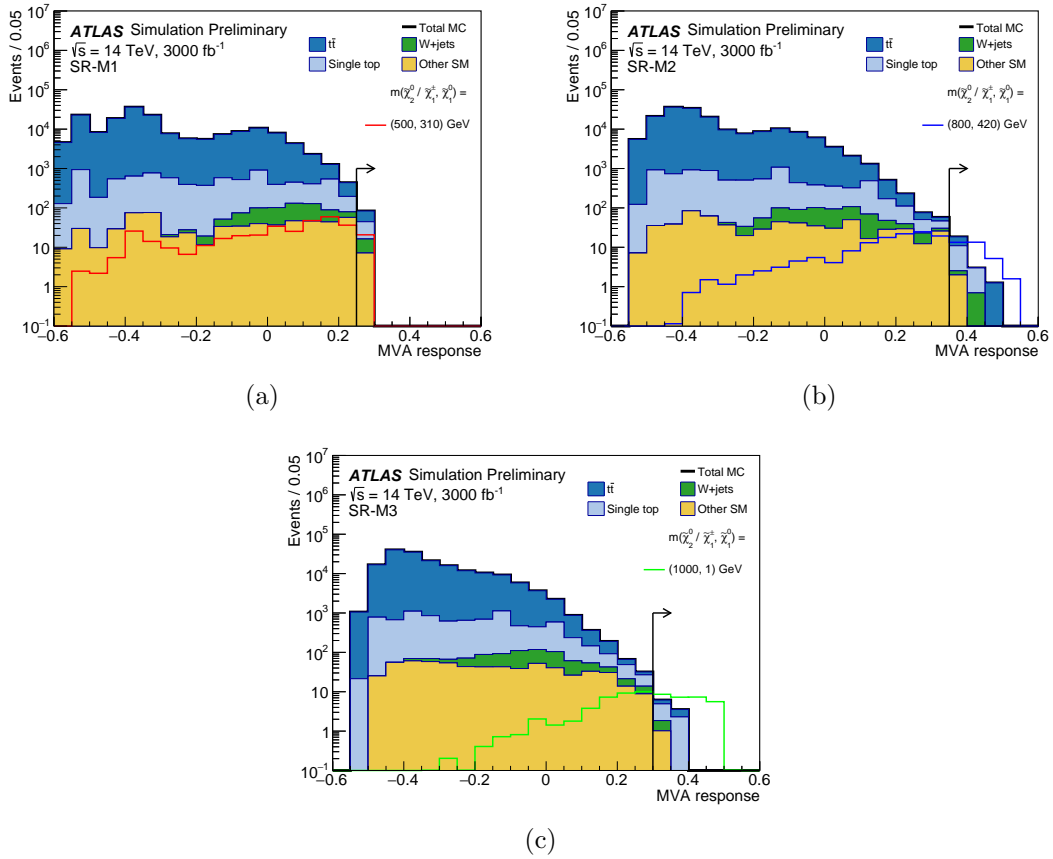


Figure 8.5: BDT outputs for HL-LHC projection. The arrow on each plot shows the cut placed on the BDT output, defining the SR.

2333 atic under consideration and are provided as multiplicative factors which are applied to
 2334 the Run-2 systematic uncertainties.

2335

2336 In this study, the systematics from the Run-2 analysis described in Chapter ?? are ex-
 2337 trapolated from SR1Lbb-High, which is the signal region most kinematically similar to
 2338 the regions presented in this analysis. The Run-4 extrapolated uncertainties are shown in
 2339 Table 8.6.

SR1Lbb-High	
JET_JER_SINGLE_NP	10.30%
Wt-Interference	8.10%
ttbar-PS	6.40%
ttbar-Generator	5.50%
ttbar-Rad	5.00%
Wt-PS	4.50%
Wt-Rad	3.30%
JET_GroupedNP_2	2.90%
JET_GroupedNP_1	2.60%
MET_SoftTrk_Scale	2.00%
Wt-Generator	1.80%
EG_RESOLUTION_ALL	1.70%
JET_GroupedNP_3	1.10%
FT_EFF_B_systematics	0.98%
FT_EFF_C_systematics	0.97%
FT_EFF_Light_systematics	0.70%
MET_SoftTrk_ResoPara	0.45%
MET_SoftTrk_ResoPerp	0.42%
FT_EFF_extrapolation_from_charm	0.41%
EG_SCALE_ALL	0.36%
FT_EFF_extrapolation	0.18%
Pileup	0.17%
MUONS_ID	0.12%
JET_EtaIntercalibration_NonClosure	0.00%
EF_EFF	0.00%
MUONS_MS	0.00%
MUON_EFF_SYS	0.00%
Quadratic sum	18.13%

Table 8.6: A table showing the extrapolated systematic uncertainties based upon the Run-2 analysis.

2340 8.5 Results

2341 The yields after the BDT cuts shown in Table 8.5 are shown below in Table 8.7. Entries
 2342 denoted by ‘-’ indicate there were no events of that particular process in the corresponding
 2343 region. Figure 8.6 shows the 95% CL exclusion limit for this channel, as well as the 5σ

Processes	SR-M1	SR-M2	SR-M3
$t\bar{t}$	38.9 ± 8.4	8.7 ± 3.3	2.5 ± 1.8
single top	28.3 ± 4.8	10.7 ± 3.2	5.4 ± 2.5
W+jets	22.2 ± 5.4	3.0 ± 2.0	2.0 ± 1.8
$t\bar{t}V$	5.1 ± 2.4	2.0 ± 1.4	1.0 ± 1.0
Diboson	2.0 ± 2.0	-	-
total background	96.5 ± 11.8	24.4 ± 5.2	10.9 ± 3.4
$m(\tilde{\chi}_1^\pm/\tilde{\chi}_2^0, \tilde{\chi}_1^0) = (500, 300)$ GeV	20.7 ± 4.8	4.6 ± 2.3	1.0 ± 1.0
$m(\tilde{\chi}_1^\pm/\tilde{\chi}_2^0, \tilde{\chi}_1^0) = (800, 420)$ GeV	44.3 ± 2.3	33.6 ± 2.0	21.2 ± 1.6
$m(\tilde{\chi}_1^\pm/\tilde{\chi}_2^0, \tilde{\chi}_1^0) = (1000, 1)$ GeV	32.2 ± 1.8	31.9 ± 1.8	28.9 ± 1.7

Table 8.7: Expected signal and background yields. The errors are statistical uncertainties. Entries marked – indicate a negligible background contribution.

2344 discovery potential. The three signal regions are combined by taking the best expected
 2345 sensitivity for each signal point. The systematics band, represented by the yellow area
 2346 around the 95% CL exclusion line includes the extrapolated experimental and modelling
 2347 systematics on the SM backgrounds, as well as the statistical uncertainty on all MC sam-
 ples.

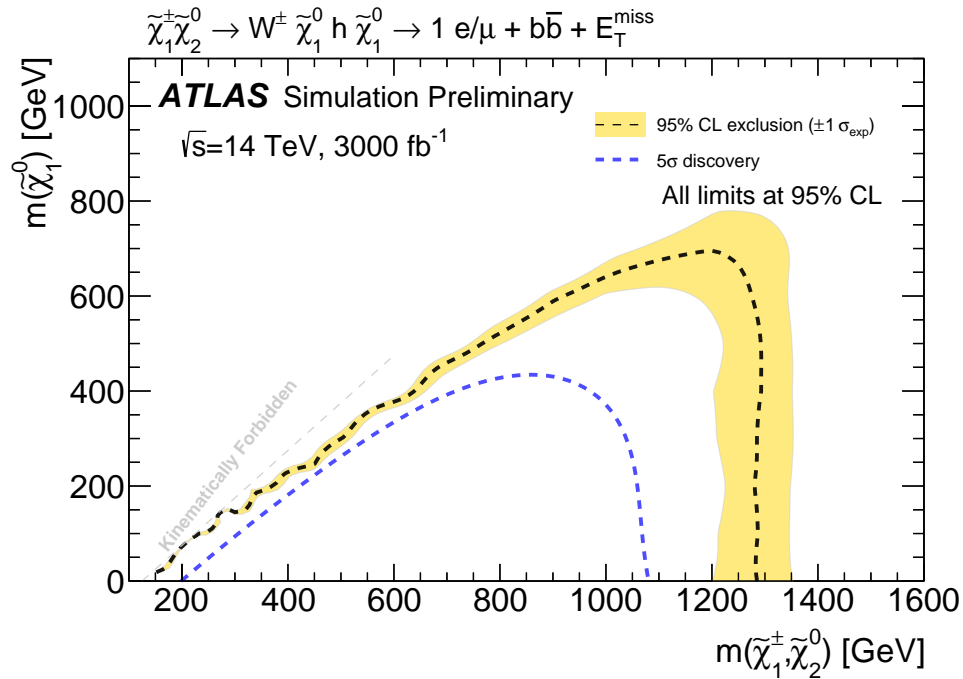


Figure 8.6: 95% CL exclusion limit and 5σ discovery limit for the analysis presented in this chapter.

2348

2349

2350 As shown in Figure 8.6, it is expected that this channel can be excluded upto 1280 GeV,
2351 while there is discovery potential upto 1070 GeV. This far exceeds the exclusion limits at
2352 the end of Run-2, with results shown in Chapter 6 for both 36.1fb^{-1} and 139fb^{-1} . During
2353 this analysis, studies were performed using a both a conventional cut-based analysis and
2354 also using a deep neural network to perform binary classification of signal and background.
2355 These studies are included in Appendix A.

2356 **Appendix A**

2357 **Sensitivity to $\tilde{\chi}_1^\pm \tilde{\chi}_2^0$ pair-production**
2358 **at the HL-LHC**

2359 The first part of this appendix is dedicated to documenting the detector simulation pa-
2360 rameterisations detailed in Chapter 8.

2361 **A.1 Detector simulation parameterisations**

2362 **Electrons**

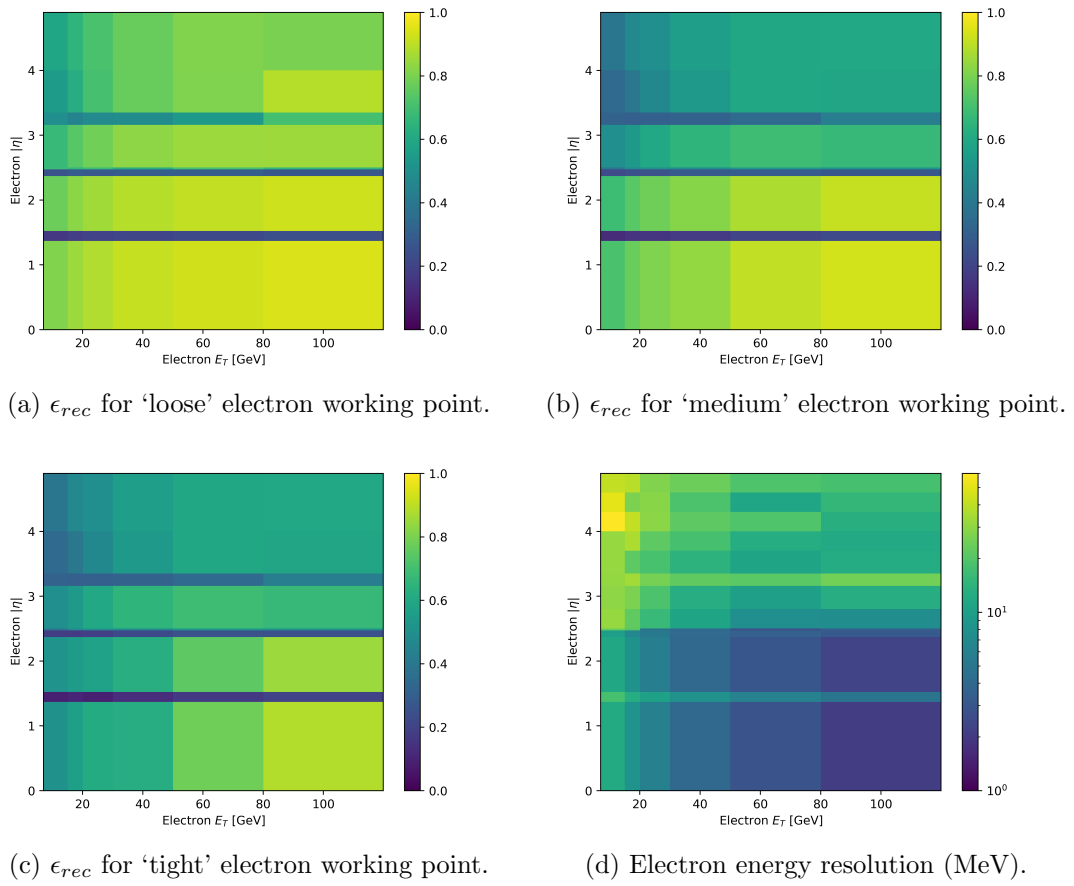
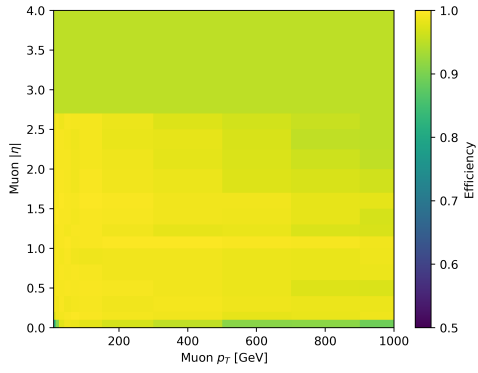
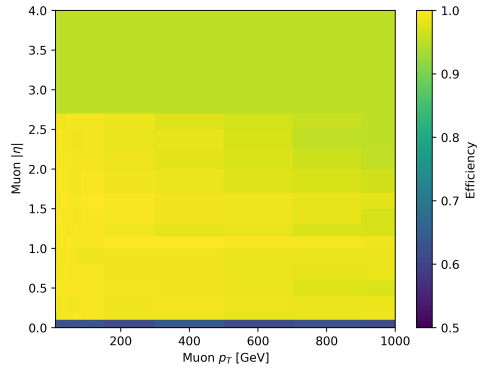


Figure A.1: Electron ID efficiencies, energy resolution and charge-flip probability for the prospects study presented in Chapter 8. The

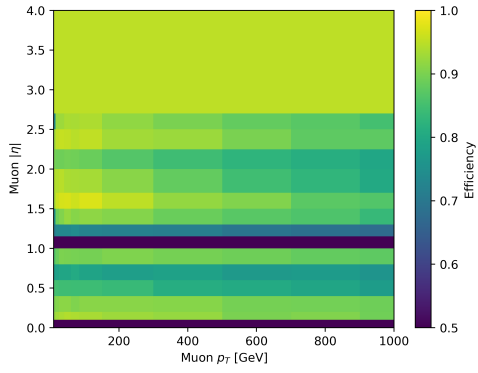
2363 **Muons**



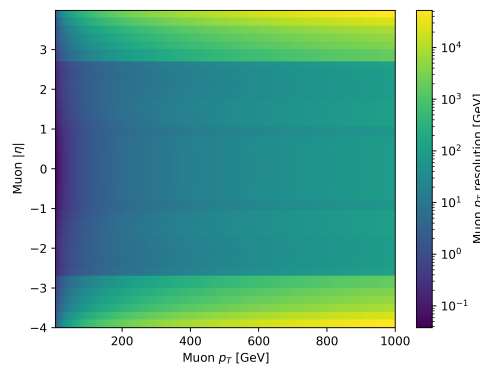
(a) ϵ_{rec} for 'loose' muon working point.



(b) ϵ_{rec} for 'tight' muon working point.



(c) ϵ_{rec} for 'high- p_T ' muon working point.



(d) Muon p_T resolution (MeV).

Figure A.2: Muon ID efficiencies and p_T resolution for the prospects study presented in Chapter 8. The

2364 **Taus**

2365 **Jets**

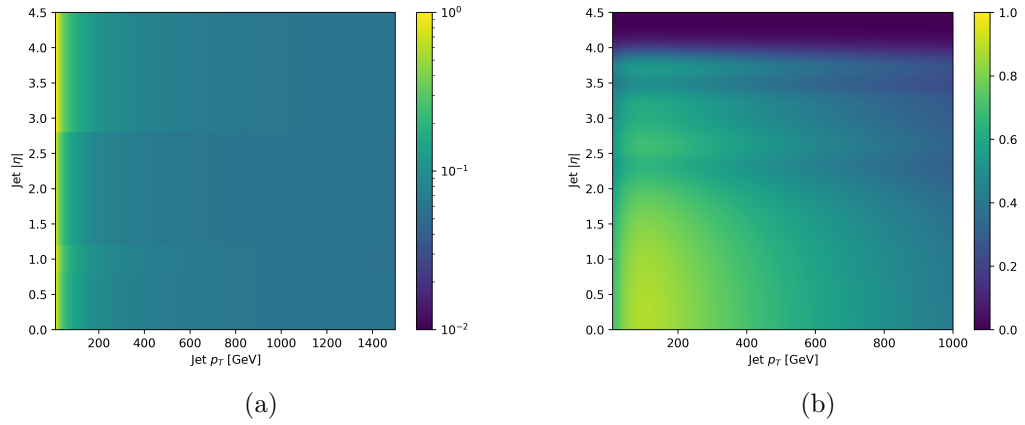


Figure A.3: Parameterised relative jet energy resolution, shown in Figure A.3a, and parameterised b -tagging efficiency, shown in Figure A.3b, used in the HL-LHC detector simulation.

2366 E_T^{miss}

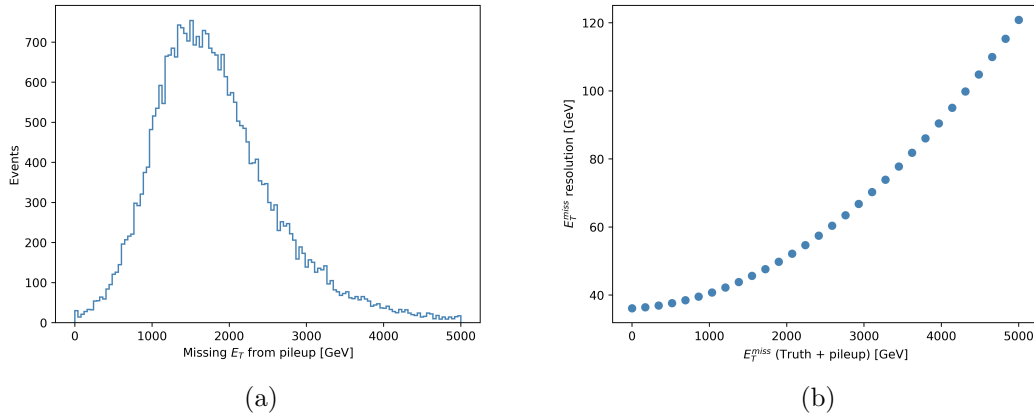


Figure A.4: Parameterised E_T^{miss} distribution from pileup, shown in Figure A.4a, and parameterised E_T^{miss} resolution, shown in Figure A.4b, used in the HL-LHC detector simulation.

2367 A.2 Cut & count studies

2368 A reoptimisation of the signal regions defined in Table 6.3 was performed to compare the
 2369 potential sensitivity of the conventional analysis to the multivariate analysis described in
 2370 Chapter 8. During the reoptimisation, the selections on the m_{bb} and m_{CT} variables are
 2371 unchanged from Table 6.3. A scan over the lower bound of the m_T and E_T^{miss} variables
 2372 was performed in steps of 10 GeV, with no upper bound. The lack of an upper bound on
 2373 these variables means the regions are able to overlap, and therefore lose their orthogonal-
 2374 ity. However, as the final fit result takes the best expected sensitivity for each point, the
 2375 orthogonality of signal regions is not required. The cuts maximising the binomial signif-
 2376 icance, Z_n , for the benchmark signal points shown in Table 8.5 are chosen for the three
 signal regions. These cuts are summarised in Table A.1. The sensitivity to each signal

	SRLM	SRMM	SRHM
m_{bb}	$\in [105, 135]$		
m_{CT}	> 160		
E_T^{miss}	> 320	> 380	> 420
m_T	> 180	> 280	> 280

Table A.1: Reoptimised signal region selections for conventional analysis in order to compare sensitivity with the multivariate analysis described in Chapter 8. All cuts are in units of GeV.

2377
 2378 point is assessed by calculating the binomial significance, Z_n , for each signal point in all
 2379 three signal regions, and the combination of the regions takes the best expected significance
 2380 for each point. The expected sensitivities can be seen in Figure A.5.

2381 A.3 Deep learning studies

2382 In addition to the the reoptimisation of the signal regions, described in the previous section,
 2383 a study of the expected sensitivity using a DNN as a binary classifier was undertaken. A
 2384 diagram of the DNN used in this study is shown in Figure A.6, and the model itself is
 2385 implemented using Keras and Tensorflow. The inputs to the classifier are the same as
 2386 described in Chapter 8 for the BDT analysis, and the same procedure for separating the
 2387 signal samples into three sets targeting different mass-splitting regimes is also the same.
 2388 The DNN is trained on a GPU for a maximum of 10000 epochs, or until the accuracy of the
 2389 classifier, evaluated using test data, has not improved in 2 epochs. To avoid overtraining,
 2390 a dropout of 20% is used, such that upto 20% of the inputs to each layer can be ignored, at
 2391 random, in each training epoch. Similarly to the BDT analysis described in Chapter 8, 3
 2392 classifiers are trained, one per mass-splitting region. The signal-background discrimination
 2393 can be seen in Figure A.7.

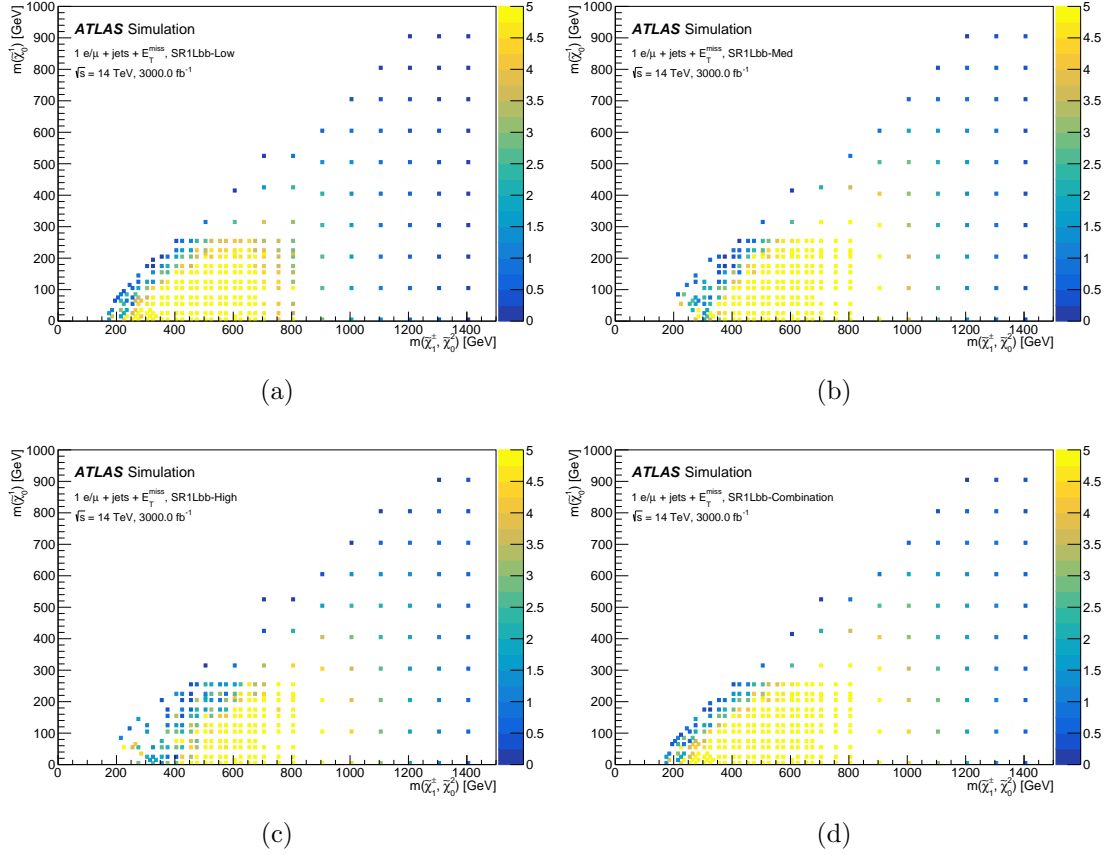
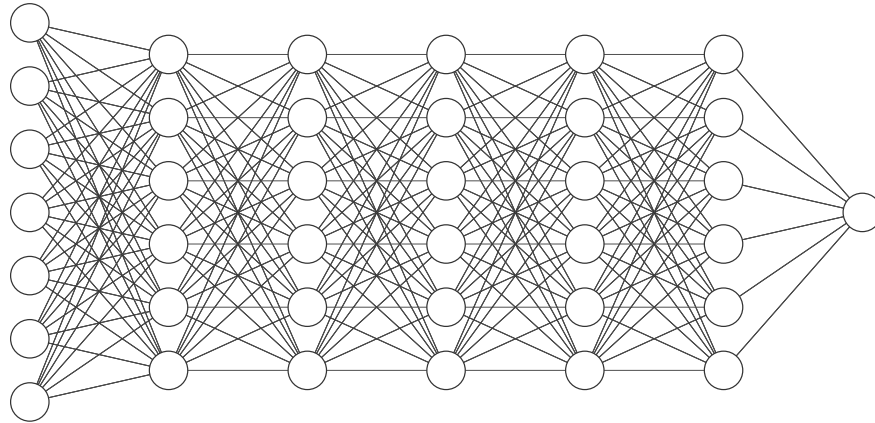


Figure A.5: Plots showing the binomial significance, Z_n , of each signal point in the reoptimised SRLM (A.5a), SRMM (A.5b), SRHM (A.5c), and the best expected combination (A.5d). All plots are produced assuming a total 15% background uncertainty.



Input Layer $\in \mathbb{R}^7$ Hidden Layer $\in \mathbb{R}^6$ Hidden Layer $\in \mathbb{R}^6$ Hidden Layer $\in \mathbb{R}^6$ Hidden Layer $\in \mathbb{R}^6$ Hidden Layer $\in \mathbb{R}^6$ Output Layer $\in \mathbb{R}^1$

Figure A.6: A diagram showing the structure of the fully-connected Deep Neural Network tested as a binary classifier in the HL-LHC sensitivity study.

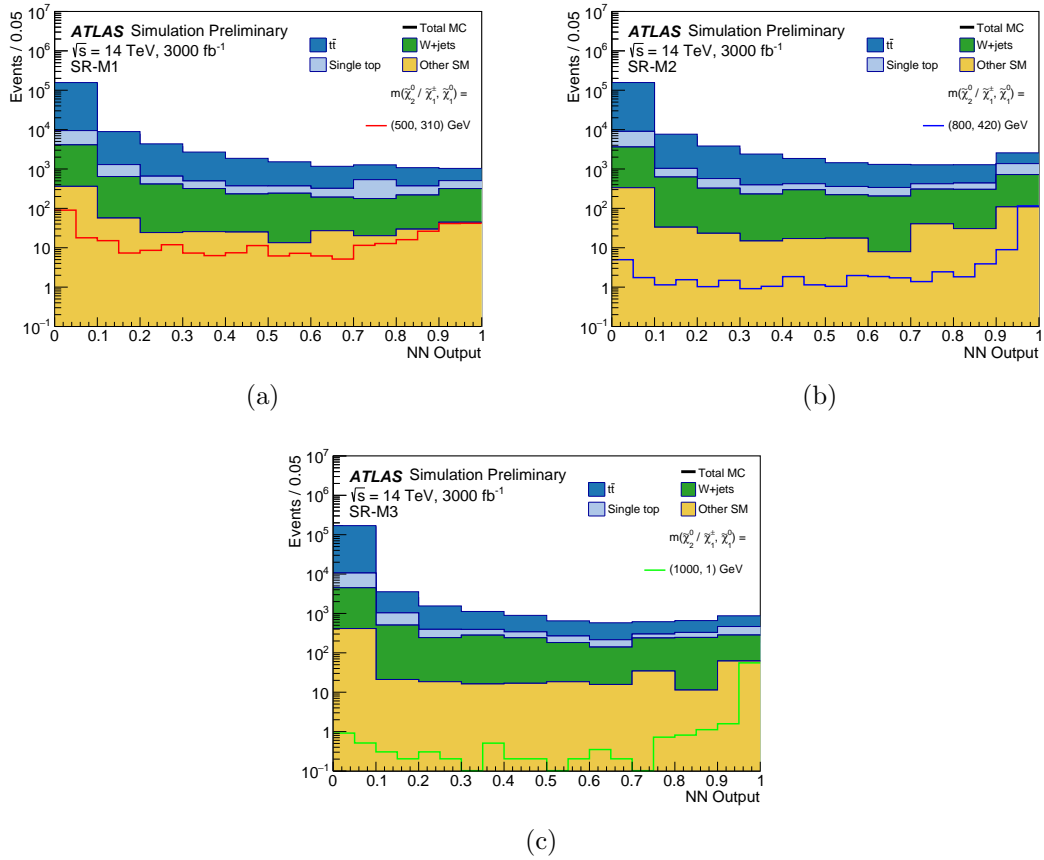


Figure A.7: Outputs for each of the DNN classifiers trained on the signal ensemble of each region and the dominant $t\bar{t}$ background.

2394 The shape and range of the output of the DNN classifiers is due to the use of the
2395 sigmoid/softmax activation on the output layer of the classifier, while TMVA performs a
2396 transformation of the form $y(x) = -\frac{1}{15} \left(\frac{1}{x} - 1\right)$ on the output of the classifier [41]. The
2397 DNN classifiers were not used in the final analysis as the sensitivity to the signal using a
2398 cut on the output of the DNN classifiers is much lower than for the BDT classifiers. While
2399 these studies were not performed due to time and resource constraints, it is expected that
2400 with larger MC statistics for the signal samples, fine-tuning of the DNN hyperparameters,
2401 and performing multi-class classification instead of binary classification, the DNN could
2402 achieve superior classification performance over the BDT classifiers.

2403 **A.4 Extending W +jets sample statistics**

2404 After applying all selections listed in Table 8.4 and the cuts on the BDT output listed
2405 in Table 8.5, the MC statistics in the W +jets sample was extremely low, such that the
2406 MC statistical uncertainty was $\sim 100\%$. For the final statistical analysis, a procedure was
2407 developed for extending the W +jets sample statistics in order to predict realistic yields and
2408 uncertainties. Using the detector simulation method described in Chapter 8, individual
2409 events in the nominal W +jets samples were smeared $N = 10$ times, to produce an extended
2410 sample with $\leq N$ times the input sample statistics. Due to the significant computing time
2411 of running this procedure, only B -filtered slices of the W +jets MC with $W \rightarrow e\nu/\mu\nu$ were
2412 used as the input for this procedure. A plot comparing the shape of the E_T^{miss} distribution
2413 for the nominal B -filtered samples with electrons, muons and taus and extended samples
2414 for B -filtered samples with electrons and muons is shown in Figure A.8.

2415 The normalisation of the extended sample is corrected for the multiple smearing method
2416 by weighting each event by a factor $\frac{1}{N}$, and corrected for the missing $W \rightarrow \ell\nu$ slices by
2417 multiplying the expected yield of the extended sample by $N_{MC}^{nominal}/N_{MC}^{extended}$ evaluated at
2418 preselection level. The correction factor for the missing MC slices was found to be 1.21.

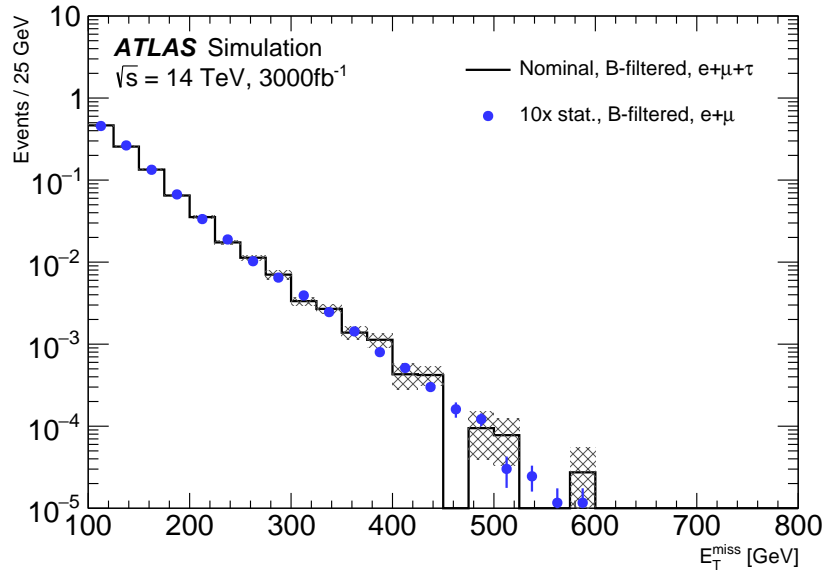


Figure A.8: A comparison of the E_T^{miss} distributions at preselection level for the nominal W +jets sample and the sample with extended MC statistics from the multiple event smearing method described in this section.

2419 Appendix B

2420 Testbeam studies of FE-I4 and 2421 RD53A performance at HL-LHC

2422 The Run-2 period of data taking concluded in 2018, with ATLAS having recorded a dataset
2423 totalling 139 fb^{-1} , making way for the start of Long Shutdown 2 (LS2). With LS2 comes
2424 the start of preparations for the next phase of the scientific programme of the LHC and
2425 ATLAS, the High-Luminosity phase. The High-Luminosity LHC (HL-LHC) will begin run-
2426 ning in the mid-2020s, bringing instantaneous luminosities around 5 times higher than in
2427 Run-2, reaching $7.5 \times 10^{34} \text{ cm}^{-2}\text{s}^{-1}$ at $\sqrt{s} = 14 \text{ TeV}$. The total integrated luminosity to be
2428 recorded by ATLAS during this period is expected to total 3000-4000 fb^{-1} . Both the LHC
2429 and ATLAS will undergo numerous upgrades to prepare for the HL-LHC operations phase.

2430

2431 The first set of upgrades to the ATLAS detector, known as the Phase I upgrades, will take
2432 place in Long Shutdown 2 (LS2), between 2019-2021. The New Small Wheel (NSW) [72]
2433 will replace the current muon end-cap system, providing precision tracking and triggering
2434 capabilities. In addition, upgrades will be made to the electronics of the LAr calorimeter
2435 system, providing higher-granularity information to the L1 trigger [73].

2436

2437 Following the completion of Run-3 of LHC operations, both ATLAS and LHC will go
2438 into Long Shutdown 3 (LS3). During the High-Luminosity LHC (HL-LHC) phase, the
2439 instantaneous luminosity is estimated to result in an average of 200 inelastic pp collisions
2440 in each bunch-crossing, with bunch-crossings occurring every 25 ns. This instantaneous
2441 luminosity far exceeds the design of the ATLAS detector described in Chapter 2. The
2442 increase in luminosity will render the current ID of the ATLAS detector inoperable, and
2443 hence a new tracker will be installed, known as the ATLAS Inner Tracker (ITk). The ITk
2444 will be constructed using only silicon pixel and strip modules, as these technologies are
2445 suited for high-occupancy, high-radiation environments. This Appendix documents studies
2446 performed on the performance of pixel modules for the upcoming ATLAS Inner Tracker

2447 (ITk) upgrade.

2448 **B.1 ATLAS ITk upgrade**

2449 **B.2 Experimental setup**

2450 **B.3**

2451

Bibliography

- 2452 [1] G. Aad, T. Abajyan, B. Abbott, J. Abdallah, S. Abdel Khalek, A.A. Abdelalim,
2453 O. Abdinov, R. Aben, B. Abi, M. Abolins, and et al. Observation of a new particle
2454 in the search for the standard model higgs boson with the atlas detector at the lhc.
2455 *Physics Letters B*, 716(1):1–29, Sep 2012.
- 2456 [2] S. Chatrchyan, V. Khachatryan, A.M. Sirunyan, A. Tumasyan, W. Adam, E. Aguilo,
2457 T. Bergauer, M. Dragicevic, J. Erö, C. Fabjan, and et al. Observation of a new
2458 boson at a mass of 125 gev with the cms experiment at the lhc. *Physics Letters B*,
2459 716(1):30–61, Sep 2012.
- 2460 [3] Y. Fukuda, T. Hayakawa, E. Ichihara, K. Inoue, K. Ishihara, H. Ishino, Y. Itow,
2461 T. Kajita, J. Kameda, S. Kasuga, and et al. Evidence for oscillation of atmospheric
2462 neutrinos. *Physical Review Letters*, 81(8):1562–1567, Aug 1998.
- 2463 [4] X. Qian and P. Vogel. Neutrino mass hierarchy. *Progress in Particle and Nuclear*
2464 *Physics*, 83:1–30, Jul 2015.
- 2465 [5] LHCb Collaboration. Observation of the resonant character of the $z(4430)^-$ state.
2466 *Phys. Rev. Lett.*, 112:222002, Jun 2014.
- 2467 [6] LHCb collaboration. Observation of structure in the j/ψ -pair mass spectrum, 2020.
- 2468 [7] LHCb Collaboration. Observation of $j/\psi p$ resonances consistent with pentaquark
2469 states in $\Lambda_b^0 \rightarrow j/\psi K^- p$ decays. *Phys. Rev. Lett.*, 115:072001, Aug 2015.
- 2470 [8] M. Tanabashi et al. Review of Particle Physics. *Phys. Rev.*, D98(3):030001, 2018.
- 2471 [9] William Martin McClain. *Axioms of group theory*, pages 55–58. Springer New York,
2472 New York, NY, 2008.
- 2473 [10] G. Arnison, A. Astbury, B. Aubert, C. Bacci, G. Bauer, A. Bézaguët, R. Böck,
2474 T.J.V. Bowcock, M. Calvetti, T. Carroll, P. Catz, P. Cennini, S. Centro, F. Cera-
2475 dini, S. Cittolin, D. Cline, C. Cochet, J. Colas, M. Corden, D. Dallman, M. De-
2476 Beer, M. Della Negra, M. Demoulin, D. Denegri, A. Di Ciaccio, D. DiBitonto, L. Do-
2477 brzynski, J.D. Dowell, M. Edwards, K. Eggert, E. Eisenhandler, N. Ellis, P. Erhard,

- 2478 H. Faissner, G. Fontaine, R. Frey, R. Frühwirth, J. Garvey, S. Geer, C. Ghesquière,
2479 P. Ghez, K.L. Giboni, W.R. Gibson, Y. Giraud-Héraud, A. Givernaud, A. Go-
2480 nidec, G. Grayer, P. Gutierrez, T. Hansl-Kozanecka, W.J. Haynes, L.O. Hertzberger,
2481 C. Hodges, D. Hoffmann, H. Hoffmann, D.J. Holthuizen, R.J. Homer, A. Honma,
2482 W. Jank, G. Jorat, P.I.P. Kalmus, V. Karimäki, R. Keeler, I. Kenyon, A. Kernan,
2483 R. Kinnunen, H. Kowalski, W. Kozanecki, D. Kryn, F. Lacava, J.-P. Laugier, J.-
2484 P. Lees, H. Lehmann, K. Leuchs, A. Lévêque, E. Linglin, E. Locci, M. Loret, J.-J.
2485 Malosse, T. Markiewicz, G. Maurin, T. McMahon, J.-P. Mendiburu, M.-N. Minard,
2486 M. Moricca, H. Muirhead, F. Muller, A.K. Nandi, L. Naumann, A. Norton, A. Orkin-
2487 Lecourtois, L. Paoluzi, G. Petrucci, G.Piano Mortari, M. Pimiä, A. Placci, E. Rader-
2488 macher, J. Ransdell, H. Reithler, J.-P. Revol, J. Rich, M. Rijssenbeek, C. Roberts,
2489 J. Rohlf, P. Rossi, C. Rubbia, B. Sadoulet, G. Sajot, G. Salvi, J. Salvini, J. Sass,
2490 A. Saudraix, A. Savoy-Navarro, D. Schinzel, W. Scott, T.P. Shah, M. Spiro, J. Strauss,
2491 K. Sumorok, F. Szoncsó, D. Smith, C. Tao, G. Thompson, J. Timmer, E. Tscheslog,
2492 J. Tuominiemi, S. Van der Meer, J.-P. Vialle, J. Vrana, V. Vuillemin, H.D. Wahl,
2493 P. Watkins, J. Wilson, Y.G. Xie, M. Yvert, and E. Zurfluh. Experimental observation
2494 of isolated large transverse energy electrons with associated missing energy at $s=540$
2495 gev . *Physics Letters B*, 122(1):103 – 116, 1983.
- 2496 [11] M. Banner, R. Battiston, Ph. Bloch, F. Bonaudi, K. Borer, M. Borghini, J.-C. Chol-
2497 let, A.G. Clark, C. Conta, P. Darriulat, L. Di Lella, J. Dines-Hansen, P.-A. Dorsaz,
2498 L. Fayard, M. Fraternali, D. Froidevaux, J.-M. Gaillard, O. Gildemeister, V.G. Goggi,
2499 H. Grote, B. Hahn, H. Hänni, J.R. Hansen, P. Hansen, T. Himel, V. Hungerbühler,
2500 P. Jenni, O. Kofoed-Hansen, E. Lançon, M. Livan, S. Loucatos, B. Madsen, P. Mani,
2501 B. Mansoulie, G.C. Mantovani, L. Mapelli, B. Merkel, M. Mermikides, R. Møllerud,
2502 B. Nilsson, C. Onions, G. Parrou, F. Pastore, H. Plothow-Besch, M. Poverel, J.-P.
2503 Repellin, A. Rothenberg, A. Roussarie, G. Sauvage, J. Schacher, J.L. Siegrist, H.M.
2504 Steiner, G. Stimpfl, F. Stocker, J. Teiger, V. Vercesi, A. Weidberg, H. Zacccone, and
2505 W. Zeller. Observation of single isolated electrons of high transverse momentum in
2506 events with missing transverse energy at the cern pp collider. *Physics Letters B*,
2507 122(5):476 – 485, 1983.
- 2508 [12] G. Arnison et al. Experimental Observation of Lepton Pairs of Invariant Mass Around
2509 $95\text{-GeV}/c^{**2}$ at the CERN SPS Collider. *Phys. Lett. B*, 126:398–410, 1983.
- 2510 [13] P. Bagnaia et al. Evidence for $Z^0 \rightarrow e^+e^-$ at the CERN $\bar{p}p$ Collider. *Phys. Lett.*,
2511 129B:130–140, 1983.
- 2512 [14] V. Agrawal, S. M. Barr, John F. Donoghue, and D. Seckel. Viable range of the mass
2513 scale of the standard model. *Physical Review D*, 57(9):5480–5492, May 1998.

- 2514 [15] A. D. Sakharov. Violation of CP Invariance, C Asymmetry, and Baryon Asymmetry
2515 of the Universe. *Soviet Journal of Experimental and Theoretical Physics Letters*, 5:24,
2516 January 1967.
- 2517 [16] Esma Mobs. The CERN accelerator complex. Complexe des accélérateurs du CERN.
2518 Jul 2016. General Photo.
- 2519 [17] Werner Herr and B Muratori. Concept of luminosity. 2006.
- 2520 [18] A. Airapetian and V. et. al. Grabsky. *ATLAS detector and physics performance:
2521 Technical Design Report, 1*. Technical Design Report ATLAS. CERN, Geneva, 1999.
- 2522 [19] G. Aad et al. The ATLAS Experiment at the CERN Large Hadron Collider. *JINST*,
2523 3:S08003, 2008.
- 2524 [20] M Capeans, G Darbo, K Einsweiler, M Elsing, T Flick, M Garcia-Sciveres, C Gemme,
2525 H Pernegger, O Rohne, and R Vuillermet. ATLAS Insertable B-Layer Technical Design
2526 Report. Technical Report CERN-LHCC-2010-013. ATLAS-TDR-19, Sep 2010.
- 2527 [21] Avoni, G and Bruschi, M et. al. The new LUCID-2 detector for luminosity measure-
2528 ment and monitoring in ATLAS. *JINST*, 13(07):P07017. 33 p, 2018.
- 2529 [22] Richard D. Ball, Valerio Bertone, Stefano Carrazza, Christopher S. Deans, Luigi
2530 Del Debbio, Stefano Forte, Alberto Guffanti, Nathan P. Hartland, José I. Latorre,
2531 and et al. Parton distributions for the lhc run ii. *Journal of High Energy Physics*,
2532 2015(4), Apr 2015.
- 2533 [23] B. Andersson, G. Gustafson, and B. Nilsson-Almqvist. A model for low-pt hadronic re-
2534 actions with generalizations to hadron-nucleus and nucleus-nucleus collisions. *Nuclear
2535 Physics B*, 281(1):289 – 309, 1987.
- 2536 [24] J.-C. Winter, F. Krauss, and G. Soff. A modified cluster-hadronisation model. *The
2537 European Physical Journal C*, 36(3):381–395, Aug 2004.
- 2538 [25] Stefano Frixione, Eric Laenen, Patrick Motylinski, Chris White, and Bryan R Webber.
2539 Single-top hadroproduction in association with awboson. *Journal of High Energy
2540 Physics*, 2008(07):029–029, Jul 2008.
- 2541 [26] Joao Pequeno and Paul Schaffner. How ATLAS detects particles: diagram of particle
2542 paths in the detector. Jan 2013.
- 2543 [27] M. Aaboud, G. Aad, B. Abbott, D. C. Abbott, O. Abidinov, B. Abeloos, D. K. Ab-
2544 hayasinghe, S. H. Abidi, O. S. AbouZeid, and et al. Electron reconstruction and
2545 identification in the ATLAS experiment using the 2015 and 2016 LHC proton–proton
2546 collision data at $\sqrt{s} = 13$ TeV. *The European Physical Journal C*, 79(8), Aug 2019.

2547 [28] M. Aaboud, G. Aad, B. Abbott, O. Abdinov, B. Abeloos, D. K. Abhayasinghe, S. H.
 2548 Abidi, O. S. AbouZeid, N. L. Abraham, and et al. Measurement of the photon identi-
 2549 fication efficiencies with the ATLAS detector using LHC Run 2 data collected in 2015
 2550 and 2016. *The European Physical Journal C*, 79(3), Mar 2019.

[29] G. Aad, B. Abbott, J. Abdallah, O. Abdinov, B. Abeloos, R. Aben, M. Abolins, O. S.
 AbouZeid, N. L. Abraham, and et al. Muon reconstruction performance of the atlas
 detector in proton–proton collision data at

$$\sqrt{s}$$

2551 $s = 13$ tev. *The European Physical Journal C*, 76(5), May 2016.

2552 [30] G. Aad, B. Abbott, J. Abdallah, O. Abdinov, R. Aben, M. Abolins, O. S. AbouZeid,
 2553 H. Abramowicz, H. Abreu, and et al. Topological cell clustering in the atlas calorime-
 2554 ters and its performance in lhc run 1. *The European Physical Journal C*, 77(7), Jul
 2555 2017.

2556 [31] Michele Livan and Richard Wigmans. Misconceptions about calorimetry. *Instruments*,
 2557 1(1):3, May 2017.

2558 [32] ATLAS Collaboration. Performance of pile-up mitigation techniques for jets in pp
 2559 collisions at $\sqrt{s} = 8$ TeV using the ATLAS detector. *Eur. Phys. J. C*, 76(11):581,
 2560 2016.

2561 [33] Georges Aad et al. ATLAS b-jet identification performance and efficiency measure-
 2562 ment with $t\bar{t}$ events in pp collisions at $\sqrt{s} = 13$ TeV. *Eur. Phys. J. C*, 79(11):970,
 2563 2019.

[34] M. Aaboud, G. Aad, B. Abbott, O. Abdinov, B. Abeloos, S. H. Abidi, O. S. AbouZeid,
 N. L. Abraham, H. Abramowicz, and et al. Search for top-squark pair production in
 final states with one lepton, jets, and missing transverse momentum using 36 fb

–1

of

$$\sqrt{s} = 13$$

2564 tev pp collision data with the atlas detector. *Journal of High Energy Physics*, 2018(6),
 2565 Jun 2018.

2566 [35] Daniel R Tovey. On measuring the masses of pair-produced semi-invisibly decaying
 2567 particles at hadron colliders. *Journal of High Energy Physics*, 2008(04):034–034, Apr
 2568 2008.

- 2569 [36] Giacomo Polesello and Daniel R. Tovey. Supersymmetric particle mass measurement
2570 with the boost-corrected contranverse mass. *Journal of High Energy Physics*, 2010(3),
2571 Mar 2010.
- 2572 [37] C.G Lester and D.J Summers. Measuring masses of semi-invisibly decaying particle
2573 pairs produced at hadron colliders. *Physics Letters B*, 463(1):99–103, Sep 1999.
- 2574 [38] Partha Konar, Kyoungchul Kong, Konstantin T. Matchev, and Myeonghun Park.
2575 Dark matter particle spectroscopy at the lhc: generalizing m t2 to asymmetric event
2576 topologies. *Journal of High Energy Physics*, 2010(4), Apr 2010.
- 2577 [39] Christopher G. Lester and Benjamin Nachman. Bisection-based asymmetric m t2
2578 computation: a higher precision calculator than existing symmetric methods. *Journal*
2579 *of High Energy Physics*, 2015(3), Mar 2015.
- 2580 [40] William Buttinger and Michel Lefebvre. Formulae for Estimating Significance. Tech-
2581 nical Report ATL-COM-GEN-2018-026, CERN, Geneva, Oct 2018.
- 2582 [41] A. Hoecker, P. Speckmayer, J. Stelzer, J. Therhaag, E. von Toerne, H. Voss,
2583 M. Backes, T. Carli, O. Cohen, A. Christov, D. Dannheim, K. Danielowski, S. Henrot-
2584 Versille, M. Jachowski, K. Kraszewski, A. Krasznahorkay Jr., M. Kruk, Y. Mahalalel,
2585 R. Ospanov, X. Prudent, A. Robert, D. Schouten, F. Tegenfeldt, A. Voigt, K. Voss,
2586 M. Wolter, and A. Zemla. Tmva - toolkit for multivariate data analysis, 2007.
- 2587 [42] Harris Drucker and Corinna Cortes. Boosting decision trees. In *NIPS*, 1995.
- 2588 [43] Yoav Freund and Robert E Schapire. A decision-theoretic generalization of on-line
2589 learning and an application to boosting. *J. Comput. Syst. Sci.*, 55(1):119–139, August
2590 1997.
- 2591 [44] Tianqi Chen and Carlos Guestrin. Xgboost. *Proceedings of the 22nd ACM SIGKDD*
2592 *International Conference on Knowledge Discovery and Data Mining*, Aug 2016.
- 2593 [45] S van der Meer. Calibration of the effective beam height in the ISR. Technical Report
2594 CERN-ISR-PO-68-31. ISR-PO-68-31, CERN, Geneva, 1968.
- [46] M. Aaboud, G. Aad, B. Abbott, J. Abdallah, O. Abdinov, B. Abeloos, R. Aben, O. S.
AbouZeid, N. L. Abraham, and et al. Luminosity determination in pp collisions at
$$\sqrt{s}$$

s = 8 tev using the atlas detector at the lhc. *The European Physical Journal C*, 76(12),
Nov 2016.

- 2597 [47] The ATLAS Collaboration. Determination of jet calibration and energy res-
2598 olution in proton-proton collisions at $\sqrt{s} = 8$ TeV using the ATLAS detec-
2599 tor. Technical Report arXiv:1910.04482, CERN, Geneva, Oct 2019. 110
2600 pages in total, author list starting page 94, 58 figures, 7 tables, submit-
2601 ted to Eur. Phys. J. C. All figures including auxiliary figures are available at
2602 <https://atlas.web.cern.ch/Atlas/GROUPS/PHYSICS/PAPERS/PERF-2014-02/>.
- 2603 [48] A method for the construction of strongly reduced representations of ATLAS exper-
2604 imental uncertainties and the application thereof to the jet energy scale. Technical
2605 Report ATL-PHYS-PUB-2015-014, CERN, Geneva, Jul 2015.
- 2606 [49] G. Aad, T. Abajyan, B. Abbott, J. Abdallah, S. Abdel Khalek, A. A. Abdelalim,
2607 O. Abdinov, R. Aben, B. Abi, and et al. Jet energy resolution in proton-proton
2608 collisions at $\sqrt{s} = 7$ TeV recorded in 2010 with the atlas detector. *The European*
2609 *Physical Journal C*, 73(3), Mar 2013.
- [50] M. Aaboud, G. Aad, B. Abbott, O. Abdinov, B. Abeloos, S. H. Abidi, O. S. AbouZeid,
N. L. Abraham, H. Abramowicz, and et al. Performance of missing transverse mo-
mentum reconstruction with the atlas detector using proton-proton collisions at
- $\sqrt{s} = 13$ TeV
- 2610 . *The European Physical Journal C*, 78(11), Nov 2018.
- 2611 [51] M. Baak, G. J. Besjes, D. Côté, A. Koutsman, J. Lorenz, and D. Short. Histfitter
2612 software framework for statistical data analysis. *The European Physical Journal C*,
2613 75(4), Apr 2015.
- 2614 [52] A L Read. Presentation of search results: theCLstechnique. *Journal of Physics G:*
2615 *Nuclear and Particle Physics*, 28(10):2693–2704, sep 2002.
- 2616 [53] Search for dark matter associated production with a single top quark in $\sqrt{s} = 13$ TeV
2617 (pp) collisions with the ATLAS detector. Technical Report ATLAS-CONF-2020-034,
2618 CERN, Geneva, Aug 2020.
- 2619 [54] Jalal Abdallah, Adi Ashkenazi, Antonio Boveia, Giorgio Busoni, Andrea De Simone,
2620 Caterina Doglioni, Aielet Efrati, Erez Etzion, Johanna Gramling, Thomas Jacques,
2621 Tongyan Lin, Enrico Morgante, Michele Papucci, Bjoern Penning, Antonio Walter
2622 Riotto, Thomas Rizzo, David Salek, Steven Schramm, Oren Slone, Yotam Soreq,
2623 Alessandro Vichi, Tomer Volansky, Itay Yavin, Ning Zhou, and Kathryn Zurek. Sim-
2624 plified models for dark matter and missing energy searches at the lhc, 2014.
- 2625 [55] Jalal Abdallah, Henrique Araujo, Alexandre Arbey, Adi Ashkenazi, Alexander
2626 Belyaev, Joshua Berger, Celine Boehm, Antonio Boveia, Amelia Brennan, Jim Brooke,

- 2627 and et al. Simplified models for dark matter searches at the lhc. *Physics of the Dark*
2628 *Universe*, 9-10:8–23, Sep 2015.
- 2629 [56] Daniel Abercrombie, Nural Akchurin, Ece Akilli, Juan Alcaraz Maestre, Brandon
2630 Allen, Barbara Alvarez Gonzalez, Jeremy Andrea, Alexandre Arbey, Georges Azuelos,
2631 Patrizia Azzi, and et al. Dark matter benchmark models for early lhc run-2 searches:
2632 Report of the atlas/cms dark matter forum. *Physics of the Dark Universe*, 27:100371,
2633 Jan 2020.
- 2634 [57] Priscilla Pani and Giacomo Polesello. Dark matter production in association with a
2635 single top-quark at the lhc in a two-higgs-doublet model with a pseudoscalar mediator.
2636 *Physics of the Dark Universe*, 21:8–15, Sep 2018.
- 2637 [58] Felix Kahlhoefer, Kai Schmidt-Hoberg, Thomas Schwetz, and Stefan Vogl. Implica-
2638 tions of unitarity and gauge invariance for simplified dark matter models. *Journal of*
2639 *High Energy Physics*, 2016(2), Feb 2016.
- 2640 [59] url: <http://feynrules.irmp.ucl.ac.be/wiki/DMsimp>.
- 2641 [60] Tomohiro Abe, Yoav Afik, Andreas Albert, Christopher R. Anelli, Liron Barak, Mar-
2642 tin Bauer, J. Katharina Behr, Nicole F. Bell, Antonio Boveia, Oleg Brandt, Giorgio
2643 Busoni, Linda M. Carpenter, Yu-Heng Chen, Caterina Doglioni, Alison Elliot, Mo-
2644 toko Fujiwara, Marie-Helene Genest, Raffaele Gerosa, Stefania Gori, Johanna Gram-
2645 ling, Alexander Grohsjean, Giuliano Gustavino, Kristian Hahn, Ulrich Haisch, Lars
2646 Henkelmann, Junji Hisano, Anders Huitfeldt, Valerio Ippolito, Felix Kahlhoefer, Greg
2647 Landsberg, Steven Lowette, Benedikt Maier, Fabio Maltoni, Margarete Muehlleitner,
2648 Jose M. No, Priscilla Pani, Giacomo Polesello, Darren D. Price, Tania Robens, Giu-
2649 lia Rovelli, Yoram Rozen, Isaac W. Sanderson, Rui Santos, Stanislava Sevova, David
2650 Sperka, Kevin Sung, Tim M. P. Tait, Koji Terashi, Francesca C. Ungaro, Eleni Vry-
2651 onidou, Shin-Shan Yu, Sau Lan Wu, and Chen Zhou. Lhc dark matter working group:
2652 Next-generation spin-0 dark matter models, 2018.
- [61] M. Aaboud, G. Aad, B. Abbott, D. C. Abbott, O. Abdinov, D. K. Abhayasinghe, S. H.
Abidi, O. S. AbouZeid, N. L. Abraham, and et al. Constraints on mediator-based dark
matter and scalar dark energy models using
- $$\sqrt{s}$$
- 2653 = 13 tev pp collision data collected by the atlas detector. *Journal of High Energy*
2654 *Physics*, 2019(5), May 2019.
- 2655 [62] Study of the double Higgs production channel $H(\rightarrow b\bar{b})H(\rightarrow \gamma\gamma)$ with the ATLAS
2656 experiment at the HL-LHC. Technical Report ATL-PHYS-PUB-2017-001, CERN,
2657 Geneva, Jan 2017.

- 2658 [63] Jung Chang, Kingman Cheung, Jae Sik Lee, and Jubin Park. Probing the trilinear
2659 Higgs boson self-coupling at the high-luminosity LHC via multivariate analysis. *Phys.*
2660 *Rev. D*, 101(1):016004, 2020.
- 2661 [64] M. Cepeda et al. *Report from Working Group 2: Higgs Physics at the HL-LHC and*
2662 *HE-LHC*, volume 7, pages 221–584. 12 2019.
- 2663 [65] Xabier Cid Vidal et al. *Report from Working Group 3: Beyond the Standard Model*
2664 *physics at the HL-LHC and HE-LHC*, volume 7, pages 585–865. 12 2019.
- 2665 [66] J. Alwall, R. Frederix, S. Frixione, V. Hirschi, F. Maltoni, O. Mattelaer, H.-S. Shao,
2666 T. Stelzer, P. Torrielli, and M. Zaro. The automated computation of tree-level and
2667 next-to-leading order differential cross sections, and their matching to parton shower
2668 simulations. *Journal of High Energy Physics*, 2014(7), Jul 2014.
- 2669 [67] Torbjörn Sjöstrand, Stefan Ask, Jesper R. Christiansen, Richard Corke, Nishita De-
2670 sai, Philip Ilten, Stephen Mrenna, Stefan Prestel, Christine O. Rasmussen, and Pe-
2671 ter Z. Skands. An introduction to pythia 8.2. *Computer Physics Communications*,
2672 191:159–177, Jun 2015.
- 2673 [68] ATLAS Run 1 Pythia8 tunes. Technical Report ATL-PHYS-PUB-2014-021, CERN,
2674 Geneva, Nov 2014.
- 2675 [69] Stefano Carrazza, Stefano Forte, and Juan Rojo. Parton distributions and event
2676 generators, 2013.
- 2677 [70] Leif Lönnblad and Stefan Prestel. Merging multi-leg nlo matrix elements with parton
2678 showers. *Journal of High Energy Physics*, 2013(3), Mar 2013.
- 2679 [71] Christoph Borschensky, Michael Krämer, Anna Kulesza, Michelangelo Mangano, San-
2680 jay Padhi, Tilman Plehn, and Xavier Portell. Squark and gluino production cross sec-
2681 tions in pp collisions at $\sqrt{s} = 13, 14, 33$ and 100 tev. *The European Physical Journal*
2682 *C*, 74(12), Dec 2014.
- 2683 [72] T Kawamoto, S Vlachos, L Pontecorvo, J Dubbert, G Mikenberg, P Iengo, C Dal-
2684 lapiccola, C Amelung, L Levinson, R Richter, and D Lellouch. New Small Wheel
2685 Technical Design Report. Technical Report CERN-LHCC-2013-006. ATLAS-TDR-
2686 020, Jun 2013. ATLAS New Small Wheel Technical Design Report.
- 2687 [73] The ATLAS Collaboration. Technical Design Report for the Phase-I Upgrade of the
2688 ATLAS TDAQ System. Technical Report CERN-LHCC-2013-018. ATLAS-TDR-023,
2689 Sep 2013. Final version presented to December 2013 LHCC.